Mathematical Multiphysical Modeling of Integrated Thermoelectric Devices

by

Joshua A. Cameron

B.S., University of Pittsburgh, 2018

Submitted to the Graduate Faculty of

the Swanson School of Engineering in partial fulfillment

of the requirements for the degree of

Master of Science

University of Pittsburgh

2021

UNIVERSITY OF PITTSBURGH

SWANSON SCHOOL OF ENGINEERING

This dissertation was presented

by

Joshua A. Cameron

It was defended on

October 1, 2020

and approved by

Matthew M. Barry, Ph.D., Assistant Professor, Department of Mechanical Engineering and Materials Science

Shervin Sammak, Ph.D., Assistant Professor, Department of Mechanical Engineering and Materials Science

Hessam Babaee, Ph.D., Assistant Professor, Department of Mechanical Engineering and Materials Science

Sung Kwon Cho, Ph.D., Professor, Department of Mechanical Engineering and Materials Science

Laura Schaefer, Ph.D., Burton J. and Ann M. McMurtry Chair and Professor, and Department Chair, Mechanical Engineering Department Rice University

Dissertation Director: Matthew M. Barry, Ph.D., Assistant Professor, Department of Mechanical Engineering and Materials Science

Mathematical Multiphysical Modeling of Integrated Thermoelectric Devices

Joshua A. Cameron, M.S

University of Pittsburgh, 2021

Thermoelectric devices have garnered attention for potential economic and environmental impacts when applied as waste heat recovery (WHR) systems. Scalability, steady-state and long- term operation, as well as compactness, are attractive features of TEDs. These characteristics are not enough to overcome the relatively low thermal conversion efficiency and electrical power output in comparison to conventional power generation systems. Consequentially, research has focused on determining optimal TED configurations that yield maximum performance for a given set of operating conditions. More often than not, these models are over-simplifications of physical systems that ignore critical physical phenomena and/or temperature dependency of material properties, namely in the modeling of the exhaust fluid flow and the developed temperature gradient across the device. In addition, such models are limited to one-off designs, providing little to no guidance on how to design a TED powered WHR system. To address the issue of modeling deficiencies, a robust, fully-coupled, thermal-fluid-electric mathematical model is introduced. This model simultaneously quantifies the thermal-fluid behavior of the exhaust gas, and the thermal-electric behavior of the heat exchanger and thermoelectric domains. The fluid behavior of the exhaust gas is modeled using empirical correlations. The thermal-fluid behavior of the exhaust gas is coupled to the thermal behavior of the heat exchanger via a control volume formulation of the Conservation of Energy equation. The thermal behavior of the heat exchanger and thermoelectric domain is modeled using a thermal resistance network coupled to the thermoelectric heat equation. The generated electric current develops implicitly with the temperature solution. The aforementioned system of equations includes temperature dependent material properties and is solved via an implicit iterative solution algorithm. This model is applied to a novel pin-fin integrated TED. Device performance based on operating conditions, device geometry and thermoelectric material geometry is determined. Using thermal-fluid data collected from Cummins ISL-powered transit buses as the inputs to the fluid domain, an exhaustive

parametric study was conducted over all possible inputs and device configurations of a TED applied to WHR of the aforementioned engines.

Table of Contents

1.0 Introduction . . . 1
1.1 Thermal Pollution . . . 1
1.2 Waste Heat Recovery . . . 2
1.3 Thermoelectric Theory . . . 7
1.4 Modeling Approaches . . . 11
1.5 Motivation . . . 14
1.6 Objectives . . . 17
2.0 Mathematical Analysis Of The Integrated Thermoelectric Device . . . 18
2.1 Multi-Physical Modeling . . . 19
2.1.1 Control Volume Approach for Modeling the Fluid Domain . . . 19
2.1.2 Thermal resistance network modeling of the solid domain . . . 26
2.1.3 Electrical domain solutions . . . 36
2.2 Solution Methodology . . . 39
2.3 Device Performance Solutions . . . 47
3.0 Results And Discussion . . . 49
3.1 Validation . . . 51
3.2 Linear Correlations . . . 62
3.2.1 Effect of Inlet Conditions . . . 64
3.2.1.1 Electrical Power Output . . . 64
3.2.1.2 Thermal Conversion Efficiency . . . 66
3.2.1.3 Performance Index . . . 69
3.2.2 Effect of Pin-Fin Heat Exchanger Geometry . . . 72
3.2.2.1 Electrical Power Output . . . 72
3.2.2.2 Thermal Conversion Efficiency . . . 75
3.2.2.3 Performance Index . . . 77
3.2.3 Effect of Thermoelectric Material Length . . . 82

3.2.3.1 Thermal Conversion Efficiency 82
3.2.4 Effect of Cold-Side Thermal Impedance 84
3.2.5 Variable Selection 84
3.3 Maximum Configuration For Optimization 85
3.4 Uni-Variate Nonlinear Regression 87
3.4.1 Equation Set $\mathbb{Z}_1$ 87
3.4.1.1 Electrical Power Output 88
3.4.1.2 Thermal Conversion Efficiency 92
3.4.1.3 Performance Index 96
3.4.2 Equation Set $\mathbb{Z}_2$ 100
3.4.2.1 Electrical Power Output 100
3.4.2.2 Thermal Conversion Efficiency 104
3.4.2.3 Performance Index 108
3.4.3 Equation Set $\mathbb{Z}_3$ 112
3.4.3.1 Electrical Power Output 112
3.4.3.2 Thermal Conversion Efficiency 116
3.4.3.3 Performance Index 120
3.5 Multivariate Nonlinear Regression 124
3.5.1 Equation Set $\mathbb{Z}_1$ 125
3.5.1.1 Electrical Power Output 125
3.5.1.2 Thermal Conversion Efficiency 128
3.5.1.3 Performance Index 131
3.5.2 Equation Set $\mathbb{Z}_2$ 135
3.5.2.1 Electrical Power Output 135
3.5.2.2 Thermal Conversion Efficiency 138
3.5.2.3 Performance Index 141
3.5.3 Equation Set $\mathbb{Z}_3$ 145
3.5.3.1 Electrical Power Output 145
3.5.3.2 Thermal Conversion Efficiency 148
3.5.3.3 Performance Index 152

3.6 Conclusions . . . 155
4.0 Conclusion And Future Work . . . 157
4.1 Conclusions . . . 157
4.2 Future Work . . . 158
Appendix. Nomenclature . . . 161
Bibliography . . . 165

List of Tables

2.1 Coefficients for polynomial expressions used for temperature dependent thermal properties of exhaust gas treated as air 43

2.2 Coefficients for polynomial expressions used for temperature dependent inertial properties of exhaust gas treated as air 44

2.3 Polynomial expressions for temperature dependent properties of interconnector and pins treated as aluminum and ceramic substrates treated as Alumina Oxide 45

2.4 Polynomial expressions for temperature dependent properties of N- and P-Type Materials of Ag-Na semiconductor pairs 46

3.1 Independent parameters and their numeric values 50

3.2 Statistical values of boxplots for electrical power output, with units of [W], grouped by inlet Reynolds number 64

3.3 Statistical values of boxplots for electrical power output, with units of [W], grouped by inlet fluid temperature 66

3.4 Statistical values of boxplots for thermal conversion efficiency, reported as percent, grouped by inlet Reynolds number 68

3.5 Statistical values of boxplots for thermal conversion efficiency, reported as percent, grouped by inlet fluid temperature 68

3.6 Statistical values of boxplots for performance index, a dimensionless quantity, grouped by inlet Reynolds number 69

3.7 Statistical values of boxplots for performance index, a dimensionless quantity, grouped by inlet fluid temperature 71

3.8 Statistical values of boxplots for electrical power output, with units of [W], grouped by maximum pins per row 74

3.9 Statistical values of boxplots for electrical power output, with units of [W] grouped by row of pins 74

3.10 Statistical values of boxplots for thermal conversion efficiency, reported as percent, grouped by pin diameter 75
3.11 Statistical values of boxplots for thermal conversion efficiency, reported as percent, grouped by pin height 77
3.12 Statistical values of boxplots for performance index, a dimensionless quantity, grouped by maximum pins per row 78
3.13 Statistical values of boxplots for performance index, a dimensionless quantity, grouped by row of pins 78
3.14 Statistical values of boxplots for performance index, a dimensionless quantity, grouped by pin diameter 81
3.15 Statistical values of boxplots for performance index, a dimensionless quantity, grouped by pin height 81
3.16 Statistical values of boxplots for thermal conversion efficiency, reported as percent, grouped by thermoelectric material length 83
3.17 Configurations of maximum performance solutions 85
3.18 Uni-variate non-linear regression results for electrical power output versus independent variables in domain $\mathbb{A}_1$ 91
3.19 Selected uni-variate non-linear fits for electrical power output in domain $\mathbb{A}_1$. 91
3.20 Uni-variate non-linear regression results for thermal conversion efficiency versus independent variables in domain $\mathbb{A}_1$ 95
3.21 Selected uni-variate non-linear fits summarized for thermal conversion efficiency in domain $\mathbb{A}_1$ 95
3.22 Uni-variate non-linear regression results for performance index versus independent variables in domain $\mathbb{A}_1$ 99
3.23 Selected uni-variate non-linear fits summarized for performance index in domain $\mathbb{A}_1$ 99
3.24 Uni-variate non-linear regression results for thermal conversion efficiency versus independent variables in domain $\mathbb{A}_2$ 103
3.25 Best uni-variate non-linear fits summarized for electrical power output in domain $\mathbb{A}_2$ 103

3.26 Uni-variate non-linear regression results for thermal conversion efficiency versus independent variables in domain $\mathbb{A}_2$ . . . 107
3.27 Best uni-variate non-linear fits summarized for thermal conversion efficiency in domain $\mathbb{A}_2$ . . . 107
3.28 Uni-variate non-linear regression results for performance index versus independent variables in domain $\mathbb{A}_2$ . . . 111
3.29 Best uni-variate non-linear fits summarized for performance index in domain $\mathbb{A}_2$ 111
3.30 Uni-variate non-linear regression results for electrical power output versus independent variables in domain $\mathbb{A}_3$ . . . 115
3.31 Best non-linear fits summarized for electrical power output in domain $\mathbb{A}_3$ . . 115
3.32 Uni-variate non-linear regression results for thermal conversion efficiency versus independent variables in domain $\mathbb{A}_3$ . . . 119
3.33 Best uni-variate non-linear fits summarized for thermal conversion efficiency in domain $\mathbb{A}_3$ . . . 119
3.34 Uni-variate non-linear regression results for thermal conversion efficiency versus independent variables in domain $\mathbb{A}_3$ . . . 123
3.35 Best uni-variate non-linear fits summarized for performance index in domain $\mathbb{A}_3$ 123
3.36 Regression analysis results for model fits of equations in set $\mathbb{Z}_1$ . . . 134
3.37 Regression analysis results for model fits of equations in set $\mathbb{Z}_2$ . . . 144
3.38 Regression analysis results for model fits of equations in set $\mathbb{Z}_3$ . . . 154

List of Figures

1.1 Illustration of a a) conventional and b) integrated thermoelectric device modules. The variables $T_{\infty,h}$, $T_{\infty,c}$, Q_h, Q_c, HEX, N and P refer to the heat source temperature, heat sink temperature, heat input, heat output, heat exchanger, n-type TEM and p-type TEM, respectively. 10

2.1 Tube arrangements in a staggered configuration 19

2.2 Top view illustration of controlled volumes 20

2.3 Side view illustration of controlled volumes 20

2.4 Schematic of an iTED module and its associated thermal resistance network. 29

2.5 TEM pair connected by the same interconnector 31

2.6 Controlled Surface of Hot-Side Junctions of TEM Pair 31

2.7 Controlled volume of TEM pair 33

2.8 Isometric view of ITED without dielectric channel housing, reproduced with permission [53] 37

2.9 Flow chart of the solution methodology 42

3.1 Comparison of analytic to numeric results for average hot-side junction temperatures, T_{avg}, for various Re and T_{in} values 53

3.2 Comparison of analytic to numeric results for total internal electrical resistance, $R_{el,tot}$, for various Re and T_{in} values 54

3.3 Comparison of analytic to numeric results for Seebeck voltage, V_{oc}, for various Re and T_{in} values 55

3.4 Comparison of analytic to numeric results for current, I, for various Re and T_{in} values 56

3.5 Comparison of analytic to numeric results for power output, $\dot{P}_o$, for various Re and T_{in} values 57

3.6 Comparison of analytic to numeric results for pumping power, $\dot{W}$, for various Re and T_{in} values 58

3.7 Comparison of analytic to numeric results for heat extracted, $\dot{Q}_{ext}$, for various Re and T_{in} values . . . 59
3.8 Comparison of analytic to numeric results for device thermal conversion efficiency, η_{th}, for various Re and T_{in} values . . . 60
3.9 Comparison of analytic to numeric results for performance index, ζ, for various Re and T_{in} values . . . 60
3.10 Correlation matrix of independent and dependent variables . . . 63
3.11 Boxplots of power output grouped by a) inlet Reynolds number and b) inlet fluid temperature. . . . 65
3.12 Boxplots of thermal conversion efficiency grouped by a) inlet Reynolds number and b) inlet fluid temperature. . . . 67
3.13 Boxplots of performance index grouped by a) inlet Reynolds number and b) inlet fluid temperature. . . . 70
3.14 Boxplots of electrical power output grouped by a) maximum pins per row count and b) the number of pin rows. . . . 73
3.15 Boxplots of thermal conversion efficiency grouped by a) pin diameter and b) pin height. . . . 76
3.16 Boxplots of performance index grouped by a) maximum pins per row count and b) the number of pin rows. . . . 79
3.17 Boxplots of performance index grouped by a) pin diameter and b) pin height. 80
3.18 Boxplot of thermal conversion efficiency grouped by thermoelectric material length . . . 83
3.19 Electrical power output versus inlet fluid temperature . . . 89
3.20 Electrical power output versus inlet Reynolds number . . . 89
3.21 Electrical power output versus maximum pins per row . . . 90
3.22 Thermal conversion efficiency versus inlet fluid temperature . . . 93
3.23 Thermal conversion efficiency versus inlet Reynolds number . . . 93
3.24 Thermal conversion efficiency versus maximum pins per row . . . 94
3.25 Performance index versus inlet fluid temperature . . . 97
3.26 Performance index versus inlet Reynolds number . . . 97

3.27 Performance index versus maximum pins per row 98
3.28 Thermal conversion efficiency versus inlet fluid temperature 101
3.29 Thermal conversion efficiency versus thermoelectic material length 101
3.30 Thermal conversion efficiency versus pin diameter 102
3.31 Thermal conversion efficiency versus inlet fluid temperature 105
3.32 Thermal conversion efficiency versus thermoelectric material length 105
3.33 Thermal conversion efficiency versus pin diameter 106
3.34 Performance index versus inlet fluid temperature 109
3.35 Performance index versus thermoelectic material length 109
3.36 Performance index versus pin diameter 110
3.37 Electrical power output versus maximum pins per row 113
3.38 Electrical power output versus pin diameter 114
3.39 Electrical power output versus inlet Reynolds number 114
3.40 Thermal conversion efficiency versus maximum pins per row 117
3.41 Thermal conversion efficiency versus pin diameter 117
3.42 Thermal conversion efficiency versus inlet Reynolds number 118
3.43 Performance index versus maximum pins per row 121
3.44 Performance index versus pin diameter 121
3.45 Performance index versus inlet Reynolds number 122
3.46 Scatter plots of electrical power output in domain $\mathbb{A}_1$ 127
3.47 Electrical power output vs inlet fluid temperature and Reynolds number . . . 128
3.48 Scatter plots of thermal conversion efficiency in domain $\mathbb{A}_1$ 130
3.49 Thermal conversion efficiency vs inlet fluid temperature and Reynolds number 131
3.50 Scatter plots of performance index in domain $\mathbb{A}_1$ 133
3.51 Performance index vs inlet fluid temperature and Reynolds number 134
3.52 Scatter plots of electrical power output in domain $\mathbb{A}_2$ 137
3.53 Electrical power output vs inlet fluid temperature and thermoelectric material length 138
3.54 Scatter plots of thermal conversion efficiency in domain $\mathbb{A}_2$ 140

3.55 Thermal conversion efficiency vs inlet fluid temperature and thermoelectric material length . . . 141
3.56 Scatter plots of performance index in domain $\mathbb{A}_2$ . . . 143
3.57 Performance index vs inlet fluid temperature and thermoelectric material length 144
3.58 Scatter plots of electrical power output in domain $\mathbb{A}_3$ . . . 147
3.59 Electrical power output vs maximum pin per row count and pin diameter . . 148
3.60 Scatter plots of thermal conversion efficiency in domain $\mathbb{A}_3$ . . . 150
3.61 Thermal conversion efficiency vs maximum pin per row count and pin diameter 151
3.62 Scatter plots of performance index in domain $\mathbb{A}_3$ . . . 153
3.63 Performance index vs maximum pin per row count and pin diameter . . . 154
4.1 Heat extraction versus inlet Reynolds number for set $\mathbb{A}_1$ . . . 159
4.2 Heat extraction versus inlet Reynolds number for set $\mathbb{A}_2$ . . . 160
4.3 Heat extraction versus inlet Reynolds number for set $\mathbb{A}_3$ . . . 160

1.0 Introduction

This dissertation discusses the coupling of thermal, electrical and fluid dynamic phenomena through mathematical modeling with the goal of increasing the performance of thermoelectric devices using the exhaust gases of transit buses. In this work, thermoelectric generators will be evaluated based on electrical power output, heat captured and thermal conversion efficiency. Before an in-depth discussion of the modeling approach, it is essential to provide context of thermal pollution, waste heat recovery, the thermoelectric effect, as well as contemporary modeling approaches for thermoelectric generators discussed in literature.

1.1 Thermal Pollution

Greenhouse gas (GHG) emissions play a significant role in the intensification of atmospheric warming. In the United States (U.S), the Environmental Protection Agency (EPA) has taken measures to quantify GHG emissions, their global warming potential, and the means by which they are produced. These GHG emissions include carbon dioxide (CO_2), nitrous oxide (NO_2), methane (CH_4), and various forms of fluorocarbons. In 2017, CO_2 was the most produced GHG from the U.S was recording at 81.6% [1]. Despite the quantity of CO_2, the effects of other GHG's on atmospheric warming are comparable given that they have larger global warming potentials over a 100-year time span [1]. The further increase of GHG emissions into the atmosphere will only intensify the rising of global temperatures given they exacerbate the greenhouse effect.

The greenhouse effect is the retention of thermal energy by GHG emissions trapped in the atmosphere. As a result, net heat flux into Earth's atmosphere is present. The first law of thermodynamics states that a net influx of heat into the Earth's atmosphere will result in global temperatures rising until it achieves thermal equilibrium. The ability of GHG emissions to retain thermal energy in Earth's atmosphere is not the only contributing factor to rising global temperatures. Concurrently, there is the creation of heat with GHG emissions - a form of thermal pollution. The combination of these two physical phenomena will accelerate rising global temperatures.

There are two major sources of heat developed within Earth's atmosphere: geothermal heat and heat created from human activity (i.e the use of fossil fuels) [2]. The rise of global economic activity comes with the rising use of fossil fuels as a primary source of electrical and mechanical power to satisfy energy demands. In the case of the U.S, it was found that in 2017, fossil fuels comprising of coal, natural gas and petroleum made up approximately 80.0% of the primary sources of fuel used to satisfy the energy needs of all sectors in the U.S economy. Of all primary fuels used in that same year, approximately 68.3% of the produced energy was lost in the form of rejected thermal energy [3]. Waste heat recovery (WHR) systems have the potential to reduce thermal pollution by converting its energy into additional electrical energy for other uses. As a result, the effects of the greenhouse effect can be mitigated while simultaneously developing additional usable energy.

1.2 Waste Heat Recovery

A WHR system utilizes thermal energy from waste heat for additional uses with the goal of increasing primary cycle efficiency. Ways by which efficiency can be increased are by using said thermal energy for other heating processes or by generating additional electrical energy. Consequently, the reduction of fuel consumption by cars, power plants, and any other devices that rely on the combustion of fossil fuels can be achieved while simultaneously reducing the rejected energy retained by waste heat. To maximize the outcome of these two phenomena, the design of a WHR system must be such that its efficiency is maximized for a quantity of GHG emission in terms of both volume and thermal energy. The maximum theoretical efficiency of a heat engine (i.e WHR system) that operates between a heat source and a heat sink to generate any amount of work is its Carnot efficiency [4]. The Carnot efficiency of a system is a combination of the temperature of the heat source (T_h) and the temperature of the heat sink (T_c), yielding the non-dimensional expression:

$$\eta = \left(1 - \frac{T_c}{T_h}\right) \tag{1.1}$$

Maximizing this parameter would require the heat source to operate at a temperature close to that of the GHG emissions. It still remains to be determined what group of GHG's are high in both volume and thermal energy. This is imperative to determine what type of WHR system works best to reduce thermal pollution and generate additional energy.

In 2017, the EPA quantified the four aforementioned types of GHG emissions produced in the U.S using an approach outlined by the 2006 Intergovernmental Panel on Climate Change Guidelines for National Greenhouse Gas Inventories [5]. They also determined the quantitative uncertainty of each GHG group and found that total emission uncertainty ranged from -6% to +7%. To compare GHG emissions, the EPA determined an equivalent quantity of CO_2 for the other three groups of GHG emissions based on their global warming potential. As a result, the comparison of emissions from a global warming standpoint can be achieved.

In conjunction with their quantification of GHG emissions, the EPA was able to segregate them into the five major fuel-consuming economic sectors in which they were produced. These sectors are the residential end-use, commercial end-use, industrial, energy generation, and transportation sectors- all of which use some form of fossil fuels comprised of coal, natural gas and petroleum. Additionally, the EPA was able to determine GHG quantities produced by fuel types used (i.e natural gas, coal, biofuels, etc.). Each sector produces an appreciable quantity of GHG emissions; however, there are distinctions among them as it pertains to volume, concentration, as well as thermal and flow characteristics when produced. The characterization of emissions is important to develop a WHR system that will take full advantage of available thermal energy by achieving maximum efficiency.

All emissions were quantified for the year of 2017. In that year, the residential end-use sector accounted for 5.1% of total U.S GHG emissions. In terms of CO_2, this equated to 330.9 MMT of CO_2 from direct emissions. Since 1990, emissions from this sector have continued to decrease. Concurrently, these emissions are primarily by-products from heating and cooking uses [1]; thus, the sources that generate them are sparse and the emissions themselves are produced at relatively low volumes.

The commercial end-use sector accounted for 6.4% of total U.S GHG emissions. This equates to 416.0 MMT of CO_2 from direct emissions. Emissions in this sector have increased since 1990; however, only at the marginal rate of 2.79%. This sector is heavily reliant on electricity generated and its emissions from direct combustion are primarily produced from the use of natural gas and petroleum used for cooking and heating [1]. Similar to the emissions from the residential end-use sector, GHG's in this sector come from sparse sources and are produced at relatively low volumes.

The industrial sector accounted for 22.2% of total U.S GHG emissions. This equates to 1,436.5 MMT of CO_2 from direct emissions. Since 1990, emissions from this sector have declined by 14.8% due to the changes in production to develop more products from less energy-intensive processes and less products from energy-intensive processes. Appreciable contributors of these direct emissions consist of fossil fuel combustion, natural gas systems and petroleum systems. From these industrial processes, CO_2 made up the majority of these emissions recording at 75.9% while CH_4 came second recording at 19.2% [1]. While methane has a much larger global warming potential than CO_2, most of the total CH_4 production is generated from the degradation of organic matter occurring in a myriad of anaerobic settings as well as natural methane released from shale gas and oil extraction [6]. Alone, the temperature and the means of release of CH_4 from this sector would make this form of emission from this sector less viable of a heat source for WHR. However, the quantity of CO_2 produced with it and the potential thermal energy it has due to being produced by direct combustion makes it a viable source for WHR.

The energy generation sector accounted for 27.5% of total U.S GHG emissions. This equates to 1,778.3 MMT of CO_2 from direct emissions. CO_2 made up the vast majority of GHG emissions produced recording at 98.89%. Of the CO_2 produced in this sector, 67.88% of it was produced from the use of coal as a primary fuel [1]. Coal power plants release emissions, at high temperatures, in the mixture of flue gases and are much more heavily concentrated compared to the those produced from the commercial and residential sectors. Singh et al. [7] developed models of a western Canadian pulverized coal boiler producing energy at a rate of 400 MW having flue gases at temperatures as high as 150 °C . Ding et al. [8] developed experimentation for high temperature recovery of CO_2 from flue gases produced by a 10 MW coal-fired power plant. Flue gases here were measured to be 301.85 °C . Given their concentration, quantity and temperature ranges, the emissions produced from the energy generation sector have the potential to be a viable heat source for WHR.

Lastly, there is the transportation sector. This sector was responsible for the largest quantity of GHG emissions recording at 28.9%. This equates to 1,866.2 MMT of CO_2 from direct emissions. The largest source of GHG emission in this sector are by-products of the internal combustion process from the engines of passenger cars, freight trucks and buses just to name a few [1]. Thanks to the growing trend in urban areas to minimize emissions, public transportation has begun to increase in ridership, especially with the use of public transit buses. With increasing ridership of buses, an interest has been fostered to increase their efficiency by reducing fuel consumption. A WHR system for transit buses has the potential to achieve this. The design of such a system would also have the potential to be scaled for other contributors of pollutants such as cars, planes and freight vehicles. In the city of Pittsburgh, we were able to obtain data for the volumetric flow rates and temperatures of exhaust gas for Cummins ISL diesel-powered transit buses operated by the Port Authority of Allegheny County for both city and highway conditions. It was found that the average post-SCR exhaust temperature was approximately 330 °C over 45-minute drive cycles, with values exceeding 400 °C under heavy loads. The average volumetric flow rate was found to be 0.22 [m^3s^{-1}]. Given their concentration, quantity and temperature, the emissions from this sector have the potential to be a viable heat source for WHR.

GHG emissions, their temperature ranges, concentration and their potential to be used for a WHR system have been discussed for a myriad of economic sectors. Overall, emissions from the transportation sector are the most viable heat source for a WHR system to simultaneously generate additional energy and reduce thermal pollution. The commercial and residential end-use sectors produce GHG's at comparatively lower temperatures and volumes. The contribution of emissions in these sectors are less than those of the industrial, energy and transportation sectors. GHG emissions from the industrial sector are appreciable, but less CO_2 is emitted compared to the energy and transportation sector. Concurrently, the other highly potent emission, CH_4, is not produced at high volumes and are produced at relatively lower temperatures than the emissions in the energy and transportation sectors. The energy sector and transportation sector produce emissions at comparable temperatures and at large volumes; however, the bulk of emissions at these temperatures come from flue gases produced with the burning of coal. Coal produced 1207.1 MMT of CO_2 compared to the 1866.2 MMT of CO_2 from the transportation sector, most of which are produced with the burning of petroleum based fuels and natural gas. Therefore, it can be deduced that the transportation sector produces a larger quantity of GHG emissions at higher temperatures.

For high temperature exhaust gases from modes of transportation to be an effective heat source for a WHR system, a device that performs direct energy conversion with minimal loss of energy from the emissions to its heat source is necessary. Concurrently, the device must be of a size such that it can be embedded within the already existent system of an automobile and be built in such a manner that doesn't add to the complexity of it's interior or require additional power to operate. Jouhara et al. [9] performed an investigative study on a large scale of WHR systems operating with low, medium and high temperature range working fluids (i.e exhaust gas). Working fluid temperature ranges have been defined as high temperature ($\geq 400\,^{\circ}\mathrm{C}$), medium temperature ($100\,^{\circ}\mathrm{C} - 400\,^{\circ}\mathrm{C}$) and low temperature. Cummins ISL diesel-powered buses produce exhaust emissions at the medium temperature range. WHR systems that work well for working fluids in this range include waste heat boilers, regenerators, run around coils (RAC's), heat pipe systems and conventional thermoelectric generators [10].

Of the aforementioned WHR systems, conventional thermoelectric generators (TEG's) suit the needs of energy conversion and reduction of thermal pollution of waste heat. While the remaining WHR systems have the potential to generate electricity, they either don't adhere to the structural needs to operate within a transit bus or require additional energy to operate. Waste heat boilers are suitable for medium to high temperature working fluids because they utilize exhaust heat to generate additional steam [11]. However, if the temperature of the exhaust gas is not high enough to turn additional working fluid into steam, an additional burner would be needed to achieve this task [12].

Regenerators have much more compact surfaces on their heat exchangers to increase effectiveness for a given pressure drop. Regenerators, however, work to transfer thermal energy from one working fluid to another through direct contact [13]. The purpose of this WHR system is to reduce thermal energy from the GHG emissions while generating additional electrical power.

RAC's are useful for systems where the heat source is too far from from the exhaust emissions. RAC's, however, require the use of an additional pump to move a secondary working fluid; thus, requiring additional spacing and energy to operate. Concurrently, their effectiveness only increases when coupled with a direct recuperator [14]. As a result, additional spacing would be needed to accommodate this system.

Heat pipes are systems that are composed of a wick structure containing a small quantity of working fluid entirely encapsulated by a sealed container. The energy from a heat source is applied on one end to evaporate the internal fluid. The internal fluid then condenses at the other end, releasing thermal energy while losing minimal heat to the surrounding environment [15]. Unfortunately, heat pipe systems require appropriate design, materials, wick structures and working fluid to be optimal for a specified temperature range. Concurrently, the system only transfers heat from a source to another substance rather than directly convert thermal energy into electrical energy.

While these WHR systems have advantages, their disadvantages make them ill-suited for use on transit buses. Conventional TEG's are ideal for they have no moving parts, do not require external components to function, are compact in size and have immense potential for use in a myriad of applications that produce rejected thermal energy in the form of exhaust gases. The device directly converts the thermal energy extracted from working fluids into electrical energy via the thermoelectric effect. In order to get the best design for a conventional TEG, a thorough description of the thermoelectric effect as well as the historical applications of conventional TEG's must be discussed to understand the transition of thermal energy into electrical energy and the design needed to maximize this effect.

1.3 Thermoelectric Theory

The thermoelectric effect is a phenomenon by which temperature gradients generate electric potentials and vice versa via a thermocouple. It consists of four separate phenomena: the Peltier, the Seebeck, the Thomson and the Bridgman effects. Operating between a temperature source and sink, a conventional TEG is capable of using the imposed temperature gradient to develop an electric potential using a series of n- and p-type semiconductors, otherwise considered as thermoelectric materials. Being embedded within a conventional TEG, thermoelectric materials have a temperature gradient imposed upon them when operating between a heat source and heat sink. As a result, an electric potential potential develops via the Seebeck effect.

The Seebeck effect is a voltage generating effect that occurs when a temperature gradient is imposed across an electrical conductor [16]. For thermoelectric materials housed within a conventional TEG, this generates the electric potential that is used for electrical energy. The Seebeck coefficient, a temperature dependent property, relates this generated electric potential to the temperature gradient used to generate it.

The Peltier effect is a heat generating effect occurring at the junctions of two dissimilar, electrically conducting materials carrying an electrical current. At the junction, one material undergoes thermoelectric cooling while the other thermoelectric heating [17]. The imposed temperature difference across the electrically conducting material will change as a result of this additional heating and cooling. The Peltier coefficient, a temperature dependent property representing a quantity of heat per unit charge, describes the quantity of heat gained or lost at the junction as a function of the carrying electrical current.

The Thomson effect is an additional heat generation effect that occurs in current carrying conductor materials with an imposed temperature gradient. A combination of the Peltier and Seebeck effect, the Thomson effect is a phenomena that occurs within a homogeneous conductor material that has an imposed temperature gradient across it and is carrying an electrical current. The result being that between any two points in the conductor materials interior, their will be a heating or cooling effect [18]. As a result, the temperature difference between any given set of points in the conductor will not be the same.

Lastly, the Bridgman effect occurs when there is a gradient in the current density within an electrically conductive material, causing localized heating [19]. This effect is often ignored in analytical and numerical models because the volumetric source term associated with it is orders of magnitude less than that of the Peltier and Thomson effects, as well as Joule heating. It is the combination of all these effects that have allowed researchers, scientist and engineers to deploy conventional TEG's as a viable form of energy conversion.

Conventional TEG's for WHR have been used extensively in recent history. They were initially restricted to specialized medical, military and space applications where monetary cost was not a significant concern [20]. However, the improvement of thermoelectric material conversion efficiency [21, 22, 23] coupled with a growing interest to decrease fuel consumption has expanded an interest to deploy TEG's into systems where thermal energy in the form of waste heat and solar radiation are essentially free.

Thacher et al. [24] determined factors of importance for TEG optimization by developing a prototype installed in a 1999 GMC Sierra light-duty truck using an interface with the engine coolant as a heat sink and the exhaust gas as a heat source. Stordeur et al. [25] developed prototypes of low-powered TEG's and demonstrated that even small temperature gradients imposed across them could power microelectronics and micro-matched systems. Suter et al. [26] determined power output and thermal conversion efficiency for a conventional TEG utilizing high temperature concentrated solar heat from a high-flux solar simulator to determine its performance in solar-to-electricity energy conversion.

Clearly, there is an interest in the improvement of conventional TEG's in the automotive, electronics and energy industries. One objective is the improvement of these devices so as to increase the electrical power produced for a given quantity of thermal energy by either optimizing heat exchanger geometry, selecting the best arrangement of thermoelectric materials, improving material conversion efficiency or some combination of the three.

While these factors are critical, there is consideration in the design of the device. Figure 1.1a shows the anatomy of an individual thermoelectric module in a conventional TEG. It includes a ceramic substrate acting as a mechanical support for the system as well as an electrical insulator to isolate the current carrying interconnectors from the electrically conductive heat exchangers. The heat exchanger is needed to ensure no chemical reactions between the working fluid and the junctions of the thermoelectric material, as well as augment the heat exchanger surface area. The interconnector is needed to connect the thermoelectric materials electrically in series. Additional heat paths, such as the ceramic substrates, increase the thermal resistance of the system. As a result, less heat can reach the hot-side junction of the thermoelectric material. This reduces the potential for a higher temperature gradient to develop across them. As a result, a smaller quantity of electrical energy would be produced. If the potential for an even greater temperature difference across the junctions of the thermoelectric materials wanted to be obtained, a new design of the conventional TEG would be a starting point for consideration.

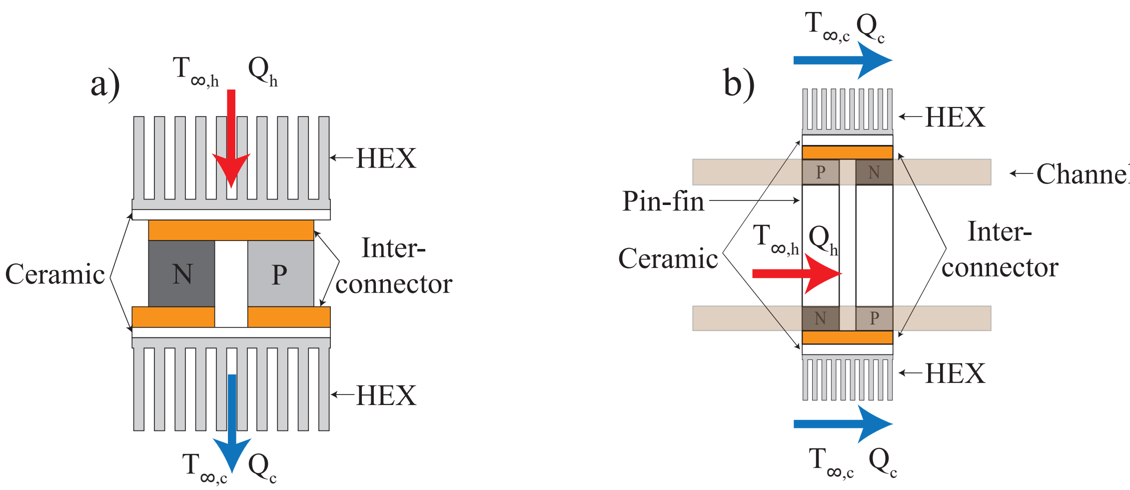

Figure 1.1: Illustration of a a) conventional and b) integrated thermoelectric device modules. The variables $T_{\infty,h}$, $T_{\infty,c}$, Q_h, Q_c, HEX, N and P refer to the heat source temperature, heat sink temperature, heat input, heat output, heat exchanger, n-type TEM and p-type TEM, respectively.

Work has been done on novel designs for TEG's with the goal of reducing the thermal resistance path between the working fluid and the hot-side junction of the TEM. Crane et al. [27, 28] developed numerical models to examine the effects of eliminating heat loss mechanisms for a TEG using a cylindrical gas/liquid heat exchanger design. Qiu et al. [29] developed a prototype of a radial TEG using only heat-conducting fins and a thin layer of a silver-based adhesive as the intermediate materials between the hot-side junction of the TEM and the heat developed by an internalized natural gas burner. A common characteristic of these designs is to structure the TEG so that the working fluid, used as a heat source, is channeled by the TEG rather than flowing across one of its external faces. A design that we consider is the integrated thermeoelectric device (iTED). Figure 1.1b shows the anatomy of an individual thermoelectric module for an iTED. It directly puts the hot-side junction of a thermoelectric material in contact with the heat exchanger while also keeping it electrically insulated via a dielectric housing. As a result, the thermoelectric materials are connected electrically in series, are electrically insulated from external objects and a smaller thermal resistance path exist between their hot-side junctions and the heat source.

The iTED has been proposed in various forms, and studied analytically [30], numerically [31, 32, 33, 34] and experimentally [35, 36]. However, these studies have not been exhaustive, but have considered one-off designs, to either demonstrate design efficacy or to illustrate improvement over a conventional device design.

A common goal of research on TEG's is to increase its efficiency and performance capability by focusing on the improvement of heat exchanger geometry as well as thermoelectric material arrangement and conversion efficiency. If efficiency and performance capability is of interest, the iTED will garner attention for analysis. The modification to the structural design from a conventional TEG does not jeopardize its application or structural integrity. Simultaneously, the reduction of substrates should increase efficiency. As discussed in previous paragraphs, there exists a desire to deploy TEG's into systems where thermal energy in the form of waste heat is essentially free. To determine if the iTED can address this need, a thorough analysis on its performance via mathematical modeling will be performed in this dissertation. Section 1.4 will discuss modeling approaches taken by other researches while section 1.5 discusses the motivation for the novel approach in mathematical modeling taken in Chapter 2.

1.4 Modeling Approaches

The operation of a TEG (i.e iTED) is a multi-faceted physics problem that is non-linear in nature. The methodological paradigm of researchers taking an analytic, numerical or mathematical approach to determining device performance is to solve the hydraulic and thermal characteristics of a working fluid and its effects on the temperature profile of the thermoelectric materials. The fluid domain is where the behavior and change of properties for the working fluid exist while the solid domain is where the behavior and change of properties of thermoelectric materials and substrates exist. The two domains are solved simultaneously using a series of boundary conditions and governing equations while also ensuring energy balance within the system. The temperature dependence of material properties and variation of velocity profiles downstream makes the use of mathematical and numerical modeling approaches the best methods to solve device solutions. This requires the variables of interest in each domain to be discretized and solved in an iterative fashion until solution convergence is achieved; otherwise, the use of temperature independent material properties, bulk empirical correlations or a combination of the two becomes essential.

While the anatomical structure of the iTED differs from that of the conventional TEG, the evaluation of variables of interest in the two aforementioned domains are similar. Meng et al. [37] developed an analytic model to solve for the electrical power generated from a conventional TEG when accounting for internal and external irreversibilities such as convection in between the air gaps of thermoelectric materials and radiation heat transfer between housing ceramic plates. In their solid domain they take into account the Thomson, Peltier and Joule heating effects of the thermoelectric materials but neglect temperature dependency of material properties. In their fluid domain, they used a bulk convection coefficient from empirical correlations and assumed isothermal heat sinks and sources. An energy balance was confirmed and the two domains were coupled using an equivalent heat flux boundary condition at the interface of the thermoelectric material junctions and their corresponding substrates. With this model, Meng et al. [37] were able to compare the electrical power generated and the thermal conversion efficiency of the device when internal irreversibilities were accounted for and when they were not.

Demir et al. [38] developed a numerical model to determine maximum electrical power generation for two configurations of TEG arrangements using a shell and tube heat exchanger for various inlet flow conditions of the working fluid. In order to model the turbulent flow of the working fluid, they used a $\kappa - \epsilon$ turbulence model using the COSMOL multiphysics software. To couple their fluid and solid domain, they imposed a uniform temperature boundary condition at all solid-fluid interfaces. Once temperature profiles were determined for the thermoelectric materials, they used the equation for maximum heat-to-electricity conversion efficiency of TEM's [4, 16] to determine the maximum electrical power generation for a set of model configurations.

Yu et al. [39] developed a numerical model to determine the performance of a conventional TEG using a parallel-plate heat exchanger. Within their solid's domain they take into account the Peltier and Joule heating effect while assuming temperature independent properties, negligible heat loss at the interface of the heat exchangers and the heat source. They also considered negligible convective heat transfer in the air gaps between thermoelectric materials. For their fluid domain, the differential equation used to describe the heat input into the thermoelectric material's hot-side junction was discretized in the direction by which the working fluid flows. The differential equation was then solved numerically using a first-order forward-difference finite-difference scheme. An energy balance was confirmed and the two domains were coupled when the difference between solutions from the aformentioned differential equation and the specific heat transfer equation was well below a specified tolerance level. Once temperature profiles were determined for the thermoelectric materials, the generated electrical power was determined by taking the difference of heat input and output of the thermoelectric modules.

He et al. [40] developed a mathematical model to determine the electrical power generated for a conventional TEG using exhaust emission conditions measured from an inline six-cylinder gasoline engine in a BMW 530i. Within their solid domain they take into account the Peltier and Joule heating effect while assuming temperature independent properties while also considering negligible radiation and internal convective heat transfer effects. For their fluid domain, they discretized their working fluids into several control volumes acting as the heat source and heat sink that varies in temperature downstream. A bulk convection coefficient for convective heat transfer is used for the entire domain. An energy balance was confirmed and the domains were coupled by applying a heat flux boundary condition at the hot-side junction of the thermoelectric materials. Since the electrical current is to be equal in all thermoelectric materials, the solutions reached convergence when the estimated relative error for electrical current was below an accepted tolerance. Once temperature profiles reached convergence, the generated electrical power was determined by taking the difference of heat input and output of the thermoelectric modules.

Kumar et al. [41, 42] developed a mathematical model to determine the electrical power generated and the affiliated pressure drop of a conventional and integrated TEG. Within their solid domain they take into account the Peltier and Joule heating effect, internal radiation heat transfer between the ceramic plates as well as temperature dependency of material properties. For their fluid domain, they discretize their working fluid into several control volumes acting as the heat source that varies in temperature downstream. A bulk convection coefficient is used for the entire domain. The domains were coupled by applying a heat flux boundary condition at the hot-side junction of the thermoelectric materials. An energy balance was confirmed by ensuring the difference between the change in enthalpy of the working fluid and the sum of the rejected heat and energy generated by the TEG was minimal. Once temperature solutions reached convergence, the generated electrical power was determined by taking the difference of heat input and heat output from the thermoelectric modules.

Several approaches for the modeling of TEG's have been discussed. It is evident from literature that in order to determine device performance, several assumptions have to be made to reduce the complexity of the physics, thus, making it solvable. While these assumptions may be argued as fair, a more robust approach can be taken to consider temperature dependency of material properties, all thermoelectric phenomena and the variation of flow characteristics for the working fluid.

1.5 Motivation

Reviewing literature on the modeling approaches of conventional and integrated TEG's, it is evident deficiencies exist. The use of temperature independent properties eliminate the non-linearity of the steady-state energy equation of thermoelectric materials. The volumetric source terms of Thomson and Joule heating are difficult to quantify as a function of length along the leg of a thermoelectric material. As a result, they are either eliminated or evenly distributed to both junctions of the thermoelectric materials. Convection coefficients developed from empirical data based on inlet flow conditions are used rather than localized convection coefficients. As a result, the variation of flow characteristics and properties downstream can be accounted for in the working fluid. Isothermal heat sources are used rather than mediums that change in temperature downstream. These assumptions make the solving of device performance solutions simple. Unfortunately, they don't consider critical physical phenomena that can result in an overestimation or underestimation of performance solutions.

From literature, modeling approaches that consider temperature dependency of materials use direct averages of hot- and cold-side junction temperatures of the TEM's for volumetric heat source terms. These include the Joule and Thomson effect. In this dissertation, we use integral averaged properties based on junction temperatures to express temperature dependent properties. We also take into account the variation of junction temperatures for each row given that the working fluid loses energy downstream.

The Thomson effect is often ignored because the distribution of heat is dependent upon the temperature along the length of the thermoelectric materials. Given that additional source terms are present in them, it is difficult to defined the temperature profile along the materials length; thus, making it difficult to quantify the Thomson heat as a function of length. The absence of this heat phenomena is consequential as discovered by Zhang [43]. Zhang performed an analytic study comparing the electrical power generated by a single thermoelectric module using an n- and p-type Bi_2Te_3 thermoelectric material pairing. They considered when the Thomson coefficient was zero- that is, the effect is ignored- and when it was represented by a third order polynomial. They examined the results for various imposed temperature differences and varying coefficients for the second order term of the material's polynomial fit. While the properties for one of these materials was subjected to this change, the properties of the other remained constant. Results varied for imposed temperature gradients. For a varying Thomson coefficient of the n-type semiconductor at low temperature gradients, Zhang found the consideration of the Thomson heat effect resulted in power generation to be, at most, 25.3% lower than the power generation from the same configuration when Thomson heating wasn't considered. At large temperature gradients, power generation was found to be, at most, 62.5% higher than the power generation from the same configuration when Thomson heating wasn't considered. For a varying Thomson coefficient of the p-type semiconductor, the power generated was always lower than the same configuration when Thomson heating was ignored. A power generation that varies between 25.3% below and 62.5% above the power generation evaluated when the Thomson heating is ignored makes it clear that the consideration of the Thomson effect is essential. In this dissertation, we consider Thomson heating effects in the same manner the Joule heating effect is consider. This is done by using integral averages for applicable material properties and equally distributing the generated heat at both junctions of the thermoelectric materials.

Empirical convection coefficients have their advantages for they are based on experimental data. From literature, it is often practiced to use a bulk convection coefficient for integrated TEG's across it's channel length. As a result, a lack of consideration for the variations in Reynolds number due to head loss and changes in kinematic viscosity exist. Temperature variation, pressure drops and the introduction of obstructing geometry play an integral role in influencing the convective heat transfer coefficient at the solid-fluid interface of a heat exchanger. In this dissertation we address this issue for a pin-fin heat exchanger used in an integrated TEG by localizing convection coefficients in controlled volumes that capture variation of temperature and the bifurcation effect for staggered pin-fin arrangements.

Isothermal heat sources and sinks are useful in so far that they eliminate the consideration for energy balances between the solid and fluid domains. It becomes a much simpler convective heat transfer problem by forcing a uniform heat flux boundary condition at the solid-fluid interface assuming the effective area of the heat exchanger and convective coefficients, as shown in literature, remain constant. In this dissertation we consider the variation in temperature of the exhaust used as the heat source. This will result in a change of the thermoelectric material's temperature dependent properties downstream; thus, eliminating factors that would otherwise overestimate or underestimate solutions describing device performance.

Several forms of modeling deficiencies have been discussed. The motivation of this dissertation is to address these deficiencies by building upon and revising contemporary approaches for the modeling of TEG's. This is done by implementing the approaches discussed in the aforementioned paragraphs of this section. Our goal is to increase the fidelity of the solutions for device performance of the iTED while also determining the magnitude of influence independent variables have on the iTED's performance. This is done using working fluids representative of the exhaust from transit buses.

1.6 Objectives

Given the areas of potential improvement pertaining to the modeling of TEG's discussed in 1.5, this work focuses on implementing modifications to the mathematical modeling with the goal of improving the fidelity of the solutions for device performance and determining the magnitude of influence independent variables have on them. The objectives of this work are:

1. To implement the aformentioned improvements for an updated mathematical model that determines device performance. This will require us to a.) integrate temperature dependency of properties for solid materials and working fluid(s) b.) discretize the fluid domain where the working fluid exist c.) account for all thermoelectric phenomena using updated temperature dependent properties and d.) use energy balances to ensure minimal global energy losses within the system.
2. To determine device performance solutions using Silver Sodium ($AgNa$) n- and p-type semiconductor pairs for the thermoelectric materials.
3. To determine the influence of the following independent variables on device performance: Inlet exhaust temperature, inlet exhaust Reynolds number, pins per row, number of rows of pins, pin diameter, pin height, thermoelectric material length, cold-side heat exchanger effective area, cold-side convection coefficient and heat sink temperature.

2.0 Mathematical Analysis Of The Integrated Thermoelectric Device

The mathematical model of the integrated thermoelectric device (iTED) consists of a solid and fluid domain. A control volume approach is used to define the space by which the energy balance and flow characteristics of the exhaust are evaluated. Here, governing equations and empirical correlations postulated by Žukauskas [44] are used to determine the heat extracted and flow characteristics of the exhaust. Pressure drops within the iTED channel due to heat exchanger geometry, head loss and ribbed walls are quantified using empirical correlations and experimental data from Chandra et al. [45], Colebrook et al. [44], Haaland [46] and Žukauskas [47].

The solid domain is modeled using a one-dimensional analytic thermal resistance network to determine all nodal temperatures. Nodal temperatures in the solid domain are influenced by their imposed boundary conditions. Once the flow characteristics and energy balance of the exhaust gas have been determined, the heat sink and source act as boundary conditions for the solid domain. This coupling of the two domains forces the temperatures of the solid domain to be solved in terms of the temperatures of both the heat source and sink in the fluid domain. As a result, nodal temperatures in the solid domain will be the result of the physical phenomena in both solid and fluid domains.

Temperature solutions in both domains are solved in a manner such that temperature dependency of material and fluid properties is considered. This requires analytic expressions to be solved in an iterative fashion until convergence is achieved. In Section 2.2, a thorough description is discussed on how the iterative approach is taken. Governing equations from Ohm [48] and Jacobi [49] are then used to determine electrical solutions of the iTED using the converged temperature solutions as inputs. Finally, the electrical solutions are used to determine metrics of device performance.

2.1 Multi-Physical Modeling

2.1.1 Control Volume Approach for Modeling the Fluid Domain

The flow characteristics and energy balance of the working fluid are influenced by the mechanical setup of the pin-fin heat exchanger and the forced convective heat transfer phenomena. To fully account for critical variations of exhaust temperature and velocity, a sub-domain from which analysis will be performed must defined. Therefore, a control volume (C∀) approach is taken to evaluate the energy state and flow characteristics of the exhaust.

Figure 2.1 shows a top view of an iTED using a staggered pin-fin configuration for a heat exchanger and corbels aligned on the walls having equivalent spacing and diameters as the pins. Figures 2.2 and 2.3 show a top and side view of the controlled volumes, respectively, labeled as C∀. The C∀'s are defined to encompass an individual pin and its local surroundings, having a height equal to the height of the pin (H_{pin}) and a length and width equal to the longitudinal pitch (S_L) and transverse pitch (S_T) respectively. By setting up the C∀'s in this manner, convective heat transfer parameters and localized dimensionless numbers, such as the Reynolds, Prandtl and Nusselt numbers, can be determined.

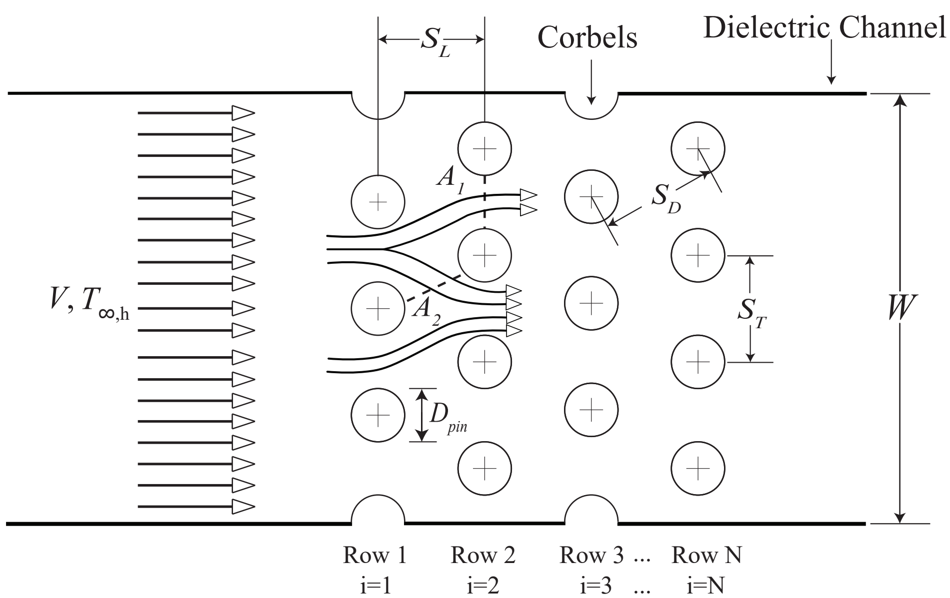

Figure 2.1: Tube arrangements in a staggered configuration

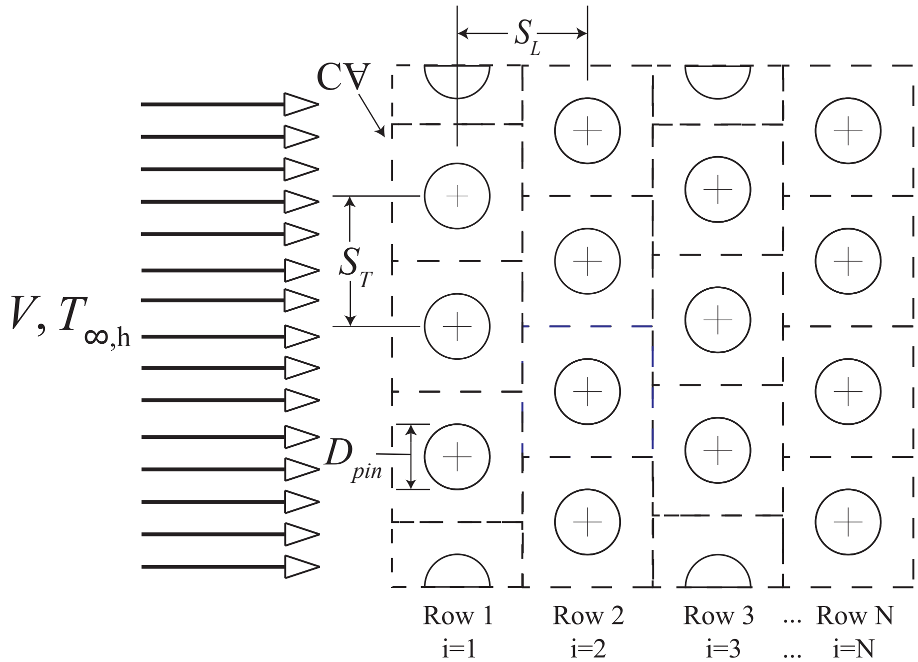

Figure 2.2: Top view illustration of controlled volumes

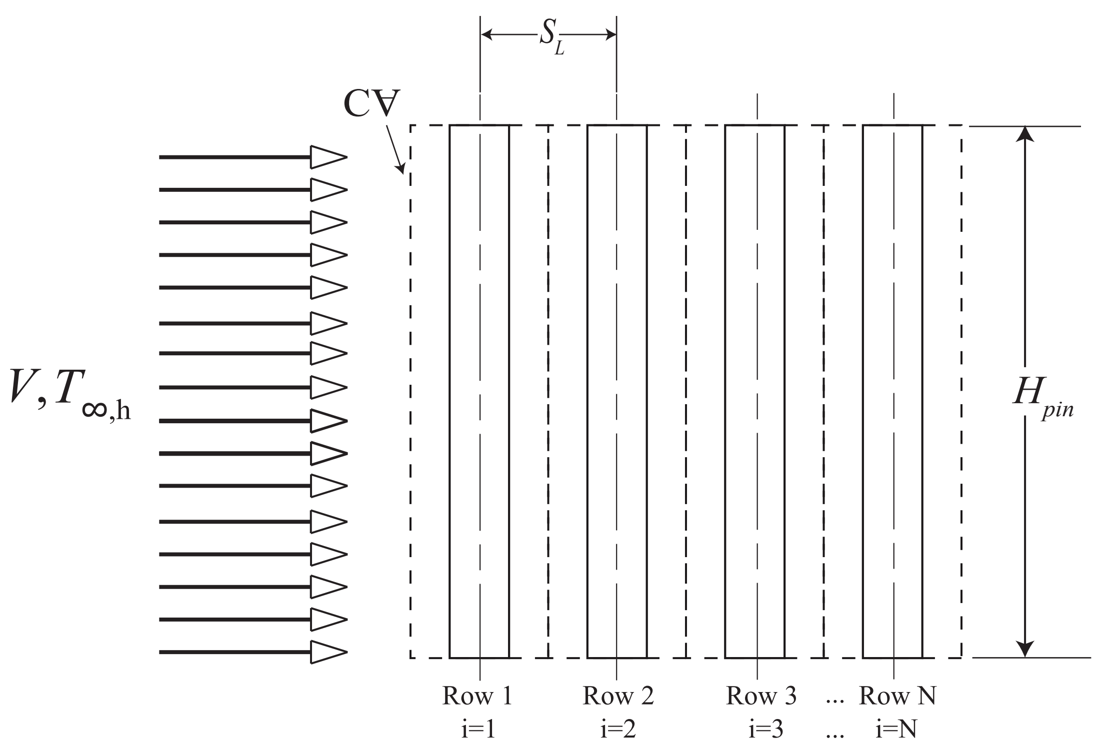

Figure 2.3: Side view illustration of controlled volumes

The iTED is idealized to be positioned after a nozzle or diffuser that channels exhaust from the post-SCR exhaust system so to capitalize on the high thermal energy state of the exhaust without adding to the complexity of the exhaust piping system. Therefore, the conditions of the exhaust at the iTED inlet will be reflective of this.

The dominant heat transfer effect is convective heat transfer at the fluid-pin interface. By using a C∀ approach, a localized convective heat transfer coefficient can be determined from the expression:

$$h = \frac{\overline{Nu}_D \lambda_{air}}{D_{pin}} \tag{2.1}$$

where $\overline{Nu}_D$ is the average Nusselt number at the interface of the working fluid and the pin, λ_{air} is its thermal conductivity and D_{pin} is the diameter of the pin. Žukauskas proposed a correlation for an average Nusselt number for aligned and staggered bank of tubes given as:

$$\overline{Nu}_D = C_1 C_2 Re_{D,max}^m Pr^{0.36} \left(\frac{Pr_{air}}{Pr_s} \right)^{1/4} \tag{2.2}$$

where C_1, C_2, and m are constants dependent on the geometric arrangement of pin-fins and maximum Reynolds number [44], $Re_{D,max}$ is the maximum Reynolds number, Pr is the Prandtl number and Pr_s is the Prandtl number of the working fluid with the latter being at the surface of the pin. The expression for the maximum Reynolds number is defined as:

$$Re_{D,max} = \frac{V_{max} D_{pin}}{\nu_{air}} \tag{2.3}$$

where V_{max} is its maximum velocity and ν_{air} is the kinematic viscosity of the working fluid.

The maximum velocity is evaluated from a conservation of mass analysis of an incompressible fluid in a controlled volume. It is defined as:

$$V_{max} = \begin{cases} \dfrac{S_T}{2(S_D - D_{pin})} V \;\middle|\; \left[S_L^2 + \left(\dfrac{S_T}{2} \right)^2 \right]^{1/2} < \dfrac{S_T + D_{pin}}{2} & \text{(2.4a)} \\[2ex] \dfrac{S_T}{(S_T - D_{pin})} V \;\middle|\; \left[S_L^2 + \left(\dfrac{S_T}{2} \right)^2 \right]^{1/2} \geq \dfrac{S_T + D_{pin}}{2} & \text{(2.4b)} \end{cases}$$

where the diagonal pitch (S_D) is given by the expression:

$$S_D = \left[S_L^2 + \left(\frac{S_T}{2}\right)^2\right]^{1/2} \tag{2.5}$$

The first condition given by expression 2.4a is the case by which the maximum velocity of the working fluid occurs at the transverse plane (A_1). The second condition given by the expression 2.4b is the case by which the maximum velocity occurs at the longitudinal plane (A_2). Both cases consider the maximum velocity to be completely orthogonal to the planes. Once the incoming velocity from the previous row has been determined, it is considered as the inlet velocity for C∀'s in the next row. As a result, Eqs. 2.1- 2.5 are used to determine the average localized convection coefficient in the C∀.

Pressure drop (ΔP_{pins}) occurs within the channel due to losses from the pin-fin heat exchanger, head loss and corbels aligned on the wall. The method of superposition is taken to quantify the total pressure drop due to losses. Žukauskas proposed an empirical correlation for pressure drop, due to the bank of pins, expressed as:

$$\Delta P_{pins} = NX\left(\frac{\rho_{air} V_{max}^2}{2}\right) f_p \tag{2.6}$$

where N is the number of rows of pins, X is a correction factor, ρ_{air} is the density of the air and f_p is the friction factor affiliated with the pins. The friction factor and correction factor are constants dependent on the maximum Reynolds number near the inlet, pin arrangement and pin geometry. Equation 2.6 determines the total pressure drop due to the bank of pins based on inlet conditions. Rather than using an expression for the entire pressure drop, the N term is dropped from Eq. 2.6 to evaluate pressure drop on a per row basis. This way, the reduction of the exhaust's maximum velocity is taken into account. Therefore, the expression for pressure drop across individual rows is defined as:

$$\Delta P_{pins} = X\left(\frac{\rho_{air} V_{max}^2}{2}\right) f_p. \tag{2.7}$$

Internal friction from the inlet until the outlet of the iTED channel is another considerable cause of pressure drop. The pressure drop due to the major frictional head loss for any segment of the channel is defined as:

$$\Delta P_{fric} = f\frac{LV^2}{2D_h g} \tag{2.8}$$

where f is the friction factor affiliated with the channel surface, L is the length of the segment of the channel, V is the velocity of the working fluid and D_h is the hydraulic diameter of the channel. Friction factors can be determined from Moody plots. Haaland, however, has developed a modified expression of Colebrook's friction factor expression by using Reynolds numbers (Re) and surface roughness (ϵ) as input parameters for his analytic expression to determine friction factors. Haaland's proposed friction factor, as a function of Reynolds number and surface roughness, can be expressed as:

$$f = \left(-1.8\log_{10}\left[\left(\frac{\epsilon/D_h}{3.7}\right)^{1.11} + \frac{6.9}{\mathrm{Re}}\right]\right)^{-2} \tag{2.9}$$

The dielectric channel is treated as plastic and is considered to have a uniform surface roughness with a numeric value of 0.45 [mm] [50]. For a rectangular cross-section, the hydraulic diameter is defined as:

$$D_h = \frac{2HW}{H+W} \tag{2.10}$$

where H is the inner height of the channel and W is its inner width. The inner height of the channel is equivalent to the height of the pin. Its width is a function of pin diameter and the maximum member of pins per row. It is defined as:

$$W = 2D_{pin}M_{max}. \tag{2.11}$$

The iTED is segmented into three sections. The first section is defined from the channel inlet until the beginning of the pins. The first section is given a length of two hydraulic diameters. The velocity of the exhaust is determined using the channel inlet Reynolds number (Re_i). Given these conditions and Eq. 2.8, the affiliated head loss ($H_{\ell,1}$) is defined as:

$$H_{\ell,1} = f\frac{\mathrm{Re}_{in}^2\nu_{air}^2}{D_h^2 g}. \tag{2.12}$$

The second section is defined from the beginning of the pins until they end. For the second section, the velocity in Eq.2.8 is considered the maximum velocity found using Eqs. 2.4a - 2.5. Its length is defined as the longitudinal pitch (i.e the length of the C$\forall$ pitch). Given these conditions and Eq. 2.8, the affiliated head loss ($H_{\ell,2}$), on a per row basis, is defined as:

$$H^i_{\ell,2} = f\frac{S_L(\mathrm{Re}^i)^2\nu^2_{air}}{D^3_h g} \tag{2.13}$$

where the superscript denotes the row being evaluated.

The last section is defined from the end of the pins until the outlet of the iTED. The last section is given a length of four hydraulic diameters. The velocity of the working fluid is approximated as the final velocity leaving the pin-fin heat exchanger. Given these conditions and Eq. 2.8, the affiliated head loss ($H_{\ell,3}$) is defined as:

$$H_{\ell,3} = f\frac{2\mathrm{Re}^2_o\nu^2_{air}}{D^2_h g}. \tag{2.14}$$

The last form of pressure drop is due to corbels (ΔP_c) aligned on the side walls of the iTED channel. Treated as semi-circular ribs with uniform spacing, corbels contribute further mixing of a working fluid with the by-product being additional pressure drop. Experimental data has been developed by Chandra relating the ratio of friction factors for ribbed and non-ribbed channel walls given a working fluids Reynolds number and rib profile. The affiliated pressure drop is defined as:

$$\Delta P_c = f_c\frac{LV^2}{2D_h g} \tag{2.15}$$

where f_c is the friction factor due to ribbed walls and L is the length of the C$\forall$ when evaluating pressure drop on a per row basis. This contribution of pressure drop is evaluated every other row given that corbels in the iTED are aligned in such a manner as shown in figure 2.1.

The turbulent nature of the working fluid makes it difficult to couple the pressure field with the velocity field of the exhaust in the form of an analytic expression. Therefore, variation of the velocity is determined by ensuring continuity for one-dimensional steady flow in the C∀'s. The continuity equation for the exhaust is defined as:

$$\nabla \cdot (\rho_{air} \overline{V}) = 0. \tag{2.16}$$

The exhaust is being emitted at velocities low enough such that its Mach number is below 0.3; therefore, it can be treated as incompressible [51]. This leads to the exhaust's density being solely a function of temperature. As a result, a one-dimensional version of Eq. 2.16 can expressed as:

$$\rho_{air}(T^{i}_{air}) V^{i} = \rho_{air}(T^{i+1}_{air}) V^{i+1}. \tag{2.17}$$

The superscripts indicate the row of the C∀. Since the C∀'s in the same row experience the same input conditions and have the same physical obstructions within, the physical phenomena within each C∀ of the same row can be idealized as equivalent. As a result, analysis only needs to be performed in one C∀ with the results replicated to the remaining C∀'s of the same row.

A conservation of energy approach is taken to determine free stream temperature of the exhaust gas. The convective heat transfer effect is assumed to take place solely at the interface of the pin-fin heat exchanger and the working fluid. The energy extracted from the exhaust gas by an individual pin is given by the equation:

$$\dot{Q}_{pin} = \dot{m} C_p \Delta T \tag{2.18}$$

where $\dot{m}$ is the mass flow rate, C_p is the temperature dependent specific heat capacity and ΔT is the temperature difference of the working fluid prior to and after its complete exposure to the pin. The specific heat capacity is a function of the inlet and outlet temperatures of the exhaust. Since the outlet temperature of the working fluid in one C∀ is the inlet temperature in the next C∀, Eq. 2.18 can be expressed as:

$$\dot{Q}_{pin} = \dot{m} \tilde{C}_p (T^{i+1}_{air} - T^{i}_{air}) \tag{2.19}$$

where the tilde overbar indicates the use of integral averaging for temperature dependent properties, T^{i+1}_{air} is the free stream temperature of the C∀ in the next row and T^{i}_{air} is the free stream temperature of the C∀ in the current row. The integral average is an operator used to take into account temperature dependency of two temperatures and will be discussed further in section 2.2. The two aforementioned temperature are the values by which the integral average will be evaluated with.

Equation 2.18 defines the rate by which thermal energy is extracted from the working fluid by an individual pin. Given a number of pins per row (M), the quantity of heat extracted by the pins on a per row basis can be expressed as:

$$\dot{Q}_{ext,row} = M(\dot{Q}_{pin}). \tag{2.20}$$

The variation of free stream temperature is critical given that it acts as a heat source for the individual pins used as a heat exchanger. Once the temperature and flow characteristics of the heat source are determined, the evaluation of nodal temperatures in the solid's domain can be accomplished.

2.1.2 Thermal resistance network modeling of the solid domain

An analytic one-dimensional thermal resistance network is used to model nodal temperatures from the heat source to the heat sink. Figure 2.4 is a schematic for an individual module of the iTED and its associated thermal resistances. The working fluid is shown to be moving downstream from left to right. It can be seen that the n- and p-type TEM's are in direct contact with the interconnector, of which connects them electrically in series. This module is also mechanically supported by a ceramic substrate. Grease layers are applied between the substrate and interconnector as well as a conventional heat exchanger with the purpose of minimizing thermal contact resistances while adding minimal thermal impedance. The conventional heat exchanger is in contact with an isothermal medium that acts as a heat sink.

As heat travels from the heat source to the heat sink, it is impeded by thermal resistances affiliated with the aforementioned materials. In sequential order, the causes of thermal resistances are as follows: convective heat-transfer resistance at the pin-fin heat exchanger-fluid interface, conductive resistance in the pin-fin heat exchanger, TEM's, interconnector, hot grease layer, ceramic substrate, and cold grease layer, and convective heat-transfer resistance at the conventional heat exchanger-fluid interface. The numeric values of these resistances will vary due to temperature dependency of material and fluid properties.

The thermal resistance network is segmented into three sections: the hot-side branch, TEM pair and cold-side branch. The methods by which the nodal temperatures in these sections are solved are different. The hot- and cold-side branches are solved using thermal resistance modeling while the TEM pair is solved using a conservation of energy approach to ensure energy balance.

The hot-side branch is the portion of the thermal resistance network composed of thermal resistances and nodal temperatures from the heat source to the hot-side junction of the n- and p-type TEM's. The total heat transfer into the hot-side branch ($\dot{Q}_h$) is a function of the temperature at each node of the thermal resistance network and the respective thermal resistances between said nodes. This total heat is defined as:

$$\begin{aligned} \dot{Q}_h = \dot{Q}_{N,h} = \dot{Q}_{P,h} = \frac{T_{\infty,h} - T_{pin}}{R_{hex,h}} = \frac{T_{pin} - T_{N,h}}{R_{th,pin}} = \\ \frac{T_{pin} - T_{P,h}}{R_{th,pin}} = \frac{T_{\infty,h} - T_{N,h}}{R_{hex,h} + R_{th,pin}} = \frac{T_{\infty,h} - T_{P,h}}{R_{hex,h} + R_{th,pin}} \end{aligned} \tag{2.21}$$

where $T_{\infty,h}$, T_{pin}, $T_{N,h}$ and $T_{P,h}$ are the temperatures of the heat source, the surface of the pin-fin heat exchanger and the hot-side junction of the n- and p- type TEM's respectively.

The expression used to determine the convective thermal resistance at the pin-fin heat exchanger-fluid interface is given as:

$$R_{hex,h} = \frac{1}{hA_{hex,h}}. \tag{2.22}$$

Based on the thermal resistance network exhibited in figure 2.4, the effective area for which convective heat transfer occurs over is half the circumferential area of the pin. This area is defined as:

$$A_{hex,h} = \frac{\pi D_{pin} H_{pin}}{2}. \tag{2.23}$$

where D_{pin} is the diameter of the pin. The conductive thermal resistance of the pin-fin heat exchanger is defined as:

$$R_{th,pin} = \frac{H_{pin}}{2(\lambda_{pin} A_{c,pin})} \tag{2.24}$$

where λ_{pin} is the isotropic, temperature dependent thermal conductivity and $A_{c,pin}$ is the cross-sectional area of the pin. Equations 2.21 - 2.24 are used to determine the heat entering the hot-side junctions of the TEM pellets.

Continuing on the path by which heat flows, thermal impedance is introduced from the TEM pair. Given that volumetric source terms exist in individual TEM pellets, a conservation of energy approach must be taken around the volume of TEM pair, rather than a thermal resistance network, to solve both of their hot- and cold-side junction temperatures. This is accomplished by solving its steady-state energy equation and applying thermal boundary conditions.

The three-dimensional steady-state general energy equation that considers Joule, Peltier and Thomson effects for an individual TEM pellet is defined as:

$$0 = \nabla \cdot (\lambda \nabla T) + \rho_{el} \mathbf{J}^2 - T\mathbf{J} \cdot \left[(\nabla \alpha)_T + \left(\frac{\delta \alpha}{\delta T} \right) \nabla T \right] \tag{2.25}$$

where λ and ρ_{el} is the TEM's thermal conductivity and electrical resistivity respectively, $\mathbf{J}$ is the current density it carries and α is it's Seebeck coefficient. Figure 2.5 is a close-up view of the TEM pair connected at the same interconnector from figure 2.4. Heat generation terms as well as heat entering and leaving the TEM pellets are labeled. A temperature boundary condition is applied at the hot- and cold-side junctions of the TEM pellets. For said junctions, a temperature boundary condition asserts that the hot-side junctions of n- and p-type pellets in the same row are equivalent. The same case applies for the cold-side junctions as well. Given these conditions, the following expressions:

$$T_{N,h} = T_{P,h} = T_h \tag{2.26}$$

$$T_{N,c} = T_{P,c} = T_c \tag{2.27}$$

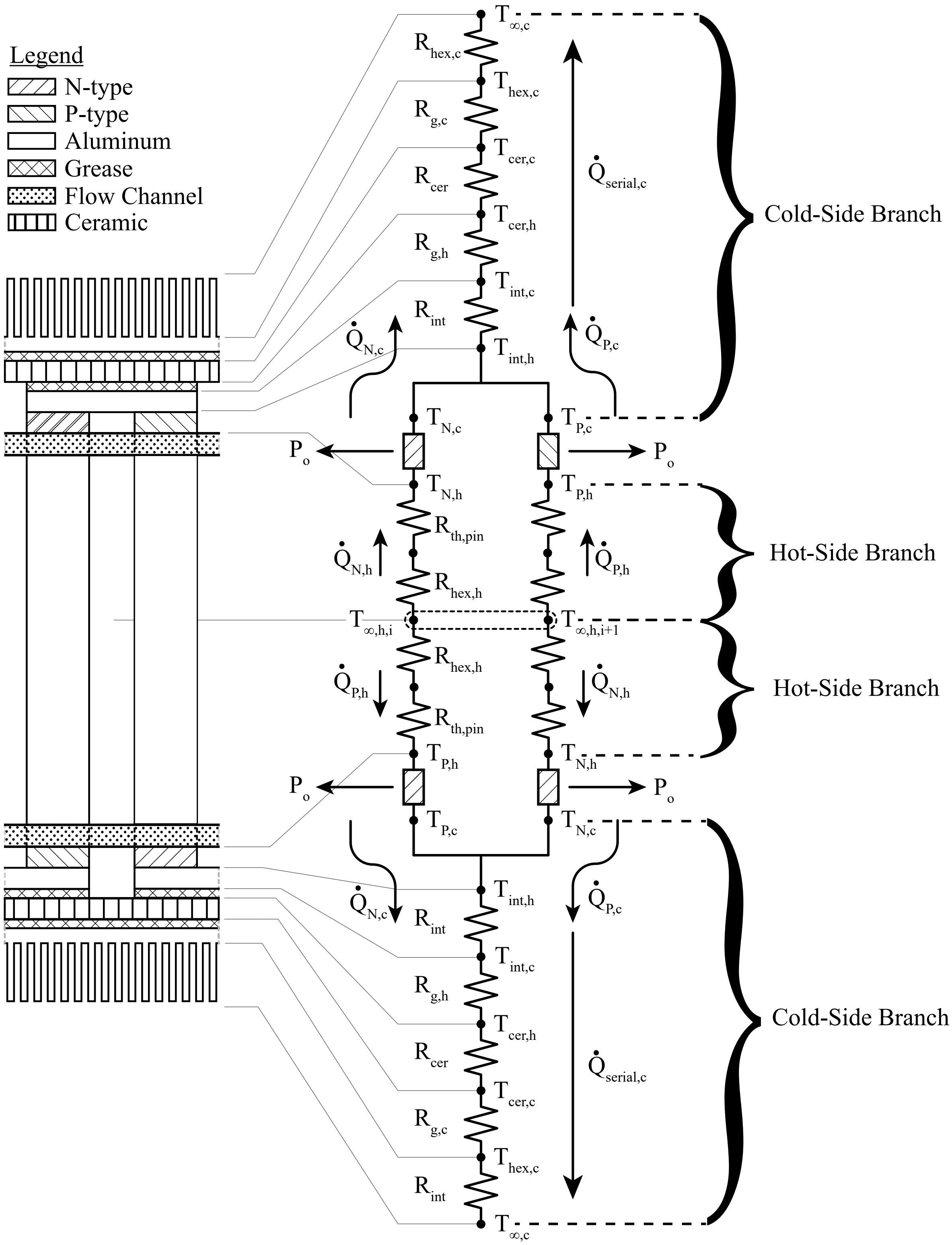

Figure 2.4: Schematic of an iTED module and its associated thermal resistance network.

$$\Delta T_N = \Delta T_P = \Delta T \tag{2.28}$$

are applied when evaluating junction temperatures at the same row. Given that the thermal impedance between equivalent heat sources and sinks with their respective junctions are the same in a given row, the boundary condition is fair to apply.

Considering a one-dimensional steady-state energy equation accounting for the Joule, Peltier and Thomson effects, the energy balance at the hot-side junction for both n- and p-type pellets can be expressed as:

$$\dot{Q}_{N,h} = K_N \Delta T_N - \frac{1}{2} I^2 R_{el,N} + I|\alpha_N(T_{N,h})|T_{N,h} - \frac{1}{2} I|\tau_N|\Delta T_N \tag{2.29}$$

$$\dot{Q}_{P,h} = K_P \Delta T_P - \frac{1}{2} I^2 R_{el,P} + I|\alpha_P(T_{P,h})|T_{P,h} - \frac{1}{2} I|\tau_P|\Delta T_P. \tag{2.30}$$

K is the thermal conductance of the TEM pellet defined by the expression:

$$K_{N,P} = \frac{\lambda_{N,P} A_{c,(N,P)}}{t_{N,P}} \tag{2.31}$$

where $\lambda_{N,P}$ is the isotropic, temperature dependent thermal conductivity, $A_{c,(N,P)}$ is the cross-sectional area and $t_{N,P}$ is the thickness of the TEM pellet. ΔT is the temperature difference of the hot-side junction temperature and the cold-side junction temperature of a TEM pellet. I is the steady-state electrical current carried by the TEM pellets. R_{el} is the TEM pellet electrical resistance defined by the expression:

$$R_{el,(N,P)} = \frac{\rho_{el,(N,P)} t_{N,P}}{A_{c,(N,P)}}. \tag{2.32}$$

The Thomson coefficient (τ) is defined as:

$$\tau_{(N,P)} = \frac{\partial \alpha_{(N,P)}}{\partial T} T. \tag{2.33}$$

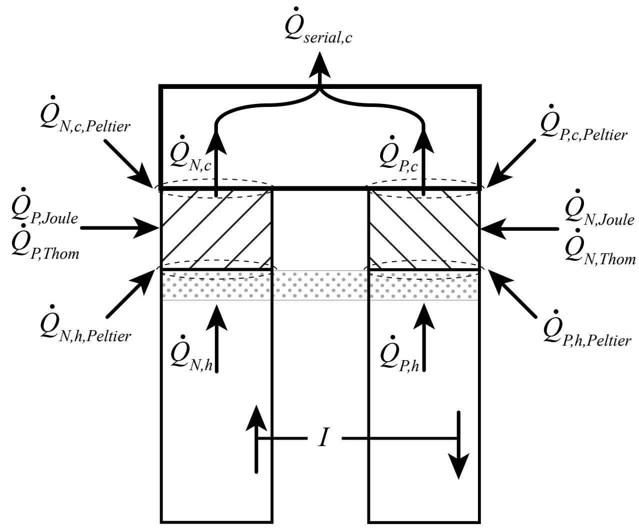

Figure 2.5: TEM pair connected by the same interconnector

The right side of Eqs. 2.29 and 2.30 are the difference between the Fourier conductive heat and the summation of volumetric and surface source and sink terms at the hot-side junction. The volumetric generation terms (i.e Thomson and Joule heating effect) are sources distributed evenly to both junctions of the pellet. The Peltier heat term is a surface effect that acts as a sink at the hot-side junctions and a source at the cold-side of hte junctions. The Seebeck coefficient is a function of the temperature at that point. Equations 2.29 and 2.30 assert that the difference between the Fourier conductive heat and the summation of volumetric and surface effects must equal the heat entering the hot-side junction; thus, ensuring energy balance at the hot-side junction.

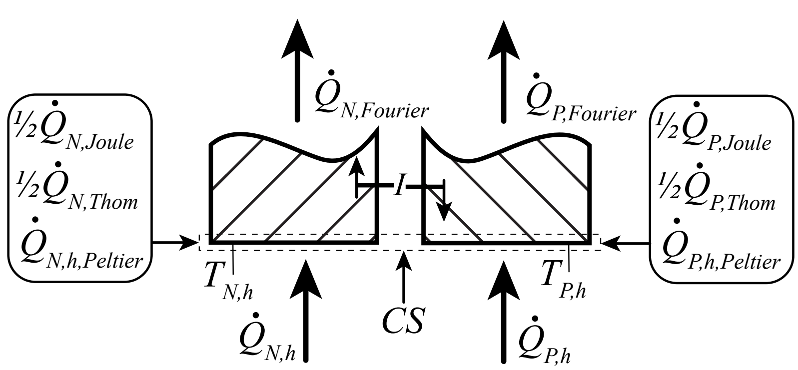

Figure 2.6: Controlled Surface of Hot-Side Junctions of TEM Pair

Figure 2.6 illustrates a TEM pair with the location of heat generation terms and direction of heat flow. The controlled surface (CS) indicated defines the input and output of heat at the hot-side junctions of the TEM pair. Here it can be seen that half of the heat from the volumetric source terms are idealized at the junctions and with the Peltier heat. Applying the temperature boundary conditions given by Eqs. 2.26-2.28, conservation of energy at the controlled surface shown in figure 2.6 can be mathematically expressed as the sum of equations 2.29 and 2.30. The resultant expression is given as:

$$\begin{aligned} \dot{Q}_{N,h} + \dot{Q}_{P,h} = K_N \Delta T + K_P \Delta T - \frac{1}{2} I^2 \big(R_{el,N} + R_{el,P}\big) + \\ I\big(|\alpha_N(T_h)| T_h + |\alpha_P(T_h)| T_h\big) - \frac{1}{2} I\big(|\tau_N| \Delta T + |\tau_P| \Delta T\big). \end{aligned} \tag{2.34}$$

The setup of Eq. 2.34 ensures that both hot- and cold-side junction temperatures, when solved, have numeric values dependent on the temperature of the heat source and the thermal impedance from the hot-side branch. Given Eq. 2.21, the explicit expression for the hot-side junction temperature is defined below as:

$$T_h = \frac{\dfrac{2T_{\infty,h}}{R_{th,pin} + R_{hex,h}} + (K_N + K_P)T_c + \dfrac{1}{2} I^2 \big(R_{el,N} + R_{el,P}\big) - \dfrac{1}{2} I\big(|\tau_N| + |\tau_P|\big) T_c}{\dfrac{2}{R_{th,pin} + R_{hex,h}} + (K_N + K_P) + I\big(|\alpha_N(T_h)| + |\alpha_P(T_h)|\big) - \dfrac{1}{2} I\big(|\tau_N| + |\tau_P|\big)}. \tag{2.35}$$

To solve both junction temperatures in terms of the temperatures of the heat source and sink, an additional equation related to the Dirichlet boundary condition is needed. Therefore, a similar approach is taken to evaluate the cold-side junction temperature based on the boundary temperatures of the heat sink. At the cold-side junctions, heat exits the TEM pellets, converge at the interconnector and continues toward the heat sink. This total heat leading from the interconnector towards the heat sink is a function of the temperature at each node of the thermal resistance network and the respective thermal resistances between said nodes. It is defined as:

$$\begin{aligned} \dot{Q}_{serial,c} = \dot{Q}_{N,c} + \dot{Q}_{P,c} = \frac{T_c - T_{\infty,c}}{R_{serial,c}} = K_N \Delta T + K_P \Delta T + \\ \frac{1}{2} I^2 \big(R_{el,N} + R_{el,P}\big) - I\big(|\alpha_N(T_h)| T_h + |\alpha_P(T_h)| T_h\big) + \frac{1}{2} I\big(|\tau_N| \Delta T + |\tau_P| \Delta T\big) \end{aligned} \tag{2.36}$$

where $R_{serial,c}$ is the equivalent resistance of the cold-side branch segment shown in figure 2.4. This equivalent resistance is defined as the complete sum of the thermal resistances defined by equations. 2.43, 2.45, 2.46 and 2.47.

A conservation of energy approach is taken about the volume of the TEM pair. Figure 2.7 illustrates the controlled volume for the TEM pair with inlet and outlet terms labeled. Given these conditions, a one-dimensional steady-state energy equation accounting for the Joule, Peltier and Thomson effects can be expressed as:

$$\dot{Q}_{N,h} + \dot{Q}_{P,h} - \dot{Q}_{N,c} - \dot{Q}_{P,c} = I\Big(\big(|\alpha_N(T_h)| + |\alpha_P(T_h)|\big)T_h - \big(|\alpha_N(T_c)| + |\alpha_P(T_c)|\big)T_c\Big) - I^2\big(R_{el,N} + R_{el,P}\big) - I\big(|\tau_N| + |\tau_P|\big)\Delta T \tag{2.37}$$

Equation 2.37 states the difference between the inlet and outlet heat must equal the generated power output of the system. The generated power output is equal in magnitude, but opposite in sign of the sum of heat generation terms (i.e Peltier, Thomson and Joule heating) defined within the controlled volume. The setup of Eq. 2.37 ensures that both hot- and cold-side junction temperatures have numeric values dependent on the temperature of the heat sink and the thermal impedance from the cold-side branch. Given Eq. 2.37, the explicit expression for the cold-side junction temperature is defined below as:

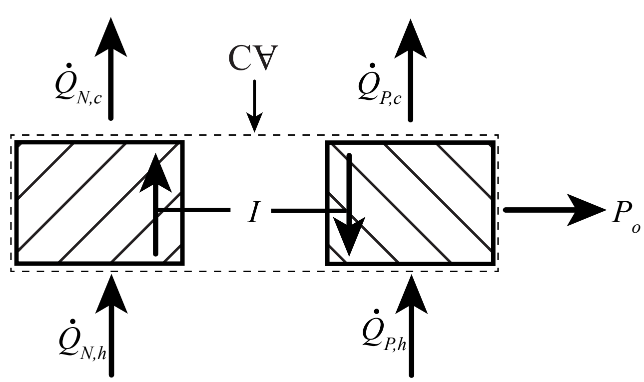

Figure 2.7: Controlled volume of TEM pair

$$T_c = \frac{\dfrac{2(T_{\infty,h} - T_h)}{R_{th,pin} + R_{hex,h}} + \dfrac{T_{\infty,c}}{R_{serial,c}} - I\big(\sum \alpha(T_h)\big)T_h + I^2\big(R_{el,N} + R_{el,P}\big) + I(\sum \tau)T_h}{\dfrac{1}{R_{serial,c}} - I\big(\sum \alpha(T_c)\big) + I\big(\sum \tau\big)\big)} \tag{2.38}$$

where the following terms have been compressed:

$$\sum \alpha(T_h) = |\alpha_N(T_h)| + |\alpha_P(T_h)| \tag{2.39}$$

$$\sum \alpha(T_c) = |\alpha_N(T_c)| + |\alpha_P(T_c)| \tag{2.40}$$

$$\sum \tau = |\tau_N(T_h, T_c)| + |\tau_P(T_h, T_c)| \tag{2.41}$$

Both Eqs. 2.35 and 2.38 are in terms of the hot- and cold-side junction temperatures. Solving the two simultaneously ensures both hot- and cold-side junction temperatures have numeric values dependent on the temperatures of both the heat source and sink.

The last segment by which heat travels is the cold-side branch, the portion of the thermal resistance network composed of nodal temperatures and thermal resistances from the cold-side junction to the heat sink. The total heat transfer in the cold-side branch (i.e $\dot{Q}_{serial,c}$) is the sum of heat leaving the n- and p-type junctions ($\dot{Q}_{N,c}$ and $\dot{Q}_{P,c}$) connected by the same interconnector. Equation 2.36 expresses this heat solely as a function of the junction temperatures. It can also be expressed as a function of the temperature at each node of the cold-side branch and the respective thermal resistances between said nodes. This total heat is defined as:

$$\begin{aligned} \dot{Q}_{serial,c} = \dot{Q}_{N,c} + \dot{Q}_{P,c} = \frac{T_{int,h} - T_{int,c}}{R_{th,int}} = \frac{T_{int,c} - T_{cer,h}}{R_{g,h}} = \\ \frac{T_{cer,h} - T_{cer,c}}{R_{th,cer}} = \frac{T_{cer,c} - T_{hex,c}}{R_{g,c}} = \frac{T_{hex,c} - T_{\infty,c}}{R_{hex,c}} \end{aligned} \tag{2.42}$$

where T_{int}, T_{cer} and $T_{hex,c}$ are the temperatures of the interconnector, ceramic and cold-branch heat exchanger respectively. The expression used to determine the conductive thermal resistance of the interconnector is given as:

$$R_{th,int} = \frac{t_{int}}{\lambda_{int} A_{int}} \tag{2.43}$$

where t_{int}, λ_{int} and A_{int} are the interconnector's thickness, isotropic, temperature dependent thermal conductivity and cross-sectional area respectively. Its thickness is taken to be 1 [mm] while its cross-sectional area is dependent on the spacing and size of the pin-fins. The expression used for the cross-sectional area is defined as:

$$A_{int} = S_T D_{pin} + \frac{\pi D_{pin}^2}{4}. \tag{2.44}$$

The expression used to determine the conductive thermal resistance of both grease layers is given as:

$$R_{g,h} = R_{g,c} = \frac{t_g}{\lambda_g A_g}. \tag{2.45}$$

where t_g, λ_g and A_g are the grease layer thickness, thermal conductivity and cross-sectional area respectively. It's thickness is taken to be $25.4 \cdot 10^{-6}$ [m] while the thermal conductivity is constant having a numeric value of 10 [$\mathrm{Wm^{-1}K^{-1}}$] [52]. The cross-sectional area of the grease layers is given the same numeric value defined by Eq. 2.44.

The expression used to determine the conductive thermal resistance of the ceramic substrate is given as:

$$R_{cer} = \frac{t_{cer}}{\lambda_{cer} A_{cer}} \tag{2.46}$$

where t_{cer}, λ_{cer} and A_{cer} are the ceramic substrate's thickness, isotropic, temperature dependent thermal conductivity and cross-sectional area respectively. It's thickness is taken to be 0.889 [mm]. The cross-sectional area of the ceramic substrate is given the same numeric value defined by Eq. 2.44.

Lastly, there is the cold branch conventional heat exchanger. The convective thermal resistance of the heat exchanger is defined as:

$$R_{hex,c} = \frac{1}{h_{hex,c} A_{hex,c}} \tag{2.47}$$

where $h_{hex,c}$ is the convective heat transfer coefficient at the cold-branch heat exchanger-fluid interface and $A_{hex,c}$ is the effective area of the heat exchanger. The convection coefficient and heat exchanger effective area are given numeric values in Chapter 3.

An equality of temperature condition is imposed on the hot-side portion of the interconnector. It asserts that its temperature is the same as the cold-side junction temperatures of the TEM pellets given that it is in direct contact with them. Given the temperature of the hot-side temperature of the interconnector, Eqs. 2.42 - 2.47 can be used to determine unknown temperatures of the cold-side branch; thus, solving the remaining nodal temperatures of the thermal resistance network. Once temperature solutions have been determined, they are used to evaluate the electrical solutions of the iTED.

2.1.3 Electrical domain solutions

Governing equations by Ohm and Jacobi are used to solve the electrical solutions of the iTED. Electrical solutions consists of potential differences(ΔV), steady-state electrical current and electrical resistance. The generation of potential difference is the result of the Seebeck effect. As discussed in Sec. 1.3, the imposition of a temperature gradient across TEM's generates a potential difference is given by the expression:

$$\Delta V_{N,P} = \alpha_{N,P} \Delta T \tag{2.48}$$

On a per row basis, the temperature gradient across TEM pellets are equivalent as discussed in Sec. 2.1.2. Simultaneously, given the setup of an individual iTED module as shown in figure 2.8, the number of n- and p-type pellets is equal to the number of pins in an individual row. Therefore, the summation of potential differences across an individual row can be defined as:

$$\Delta V_{row} = M(\alpha_N + \alpha_P)\Delta T \tag{2.49}$$

where M is the number of pins at the row being evaluated. The summation of potential differences across the entire iTED can be defined as:

$$V_{oc} = \sum_{i=1}^{N} M^i(\alpha_N^i + \alpha_P^i)\Delta T^i \tag{2.50}$$

where the superscript denotes the index of the row being evaluated. This potential difference is called the open-circuit voltage and is the driver of electrical power generated by the iTED.

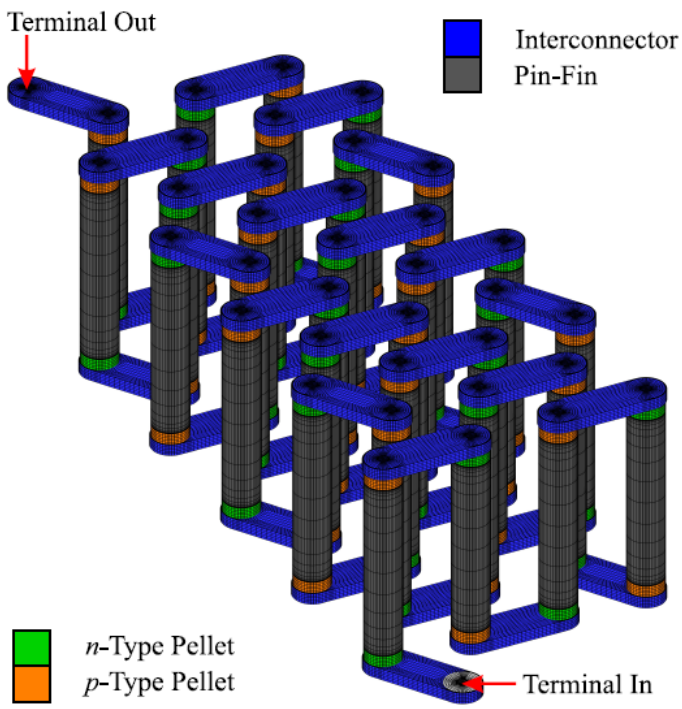

Figure 2.8: Isometric view of ITED without dielectric channel housing, reproduced with permission [53]

The electrical resistance of the iTED (R_{eq}) is the equivalent resistance of electrical conductive elements, housed in the dielectric channel, that carry the electrical current. This consists of the interconnector, pin-fin heat exchanger and n- and p-type materials. The electrical resistance of the interconnector is expressed as:

$$R_{el,int} = \frac{\rho_{el,int} L_{int}}{A_{int}}. \tag{2.51}$$

where $\rho_{el,int}$ is the isotropic, temperature dependent electrical resistivity and L_{int} is the length of the interconnector defined as:

$$L_{int} = \sqrt{S_T^2 + \left(\frac{S_L}{2}\right)^2}. \tag{2.52}$$

The electrical resistance of the pin-fin heat exchanger is defined as:

$$R_{el,pin} = \frac{4\rho_{el,pin} H_{pin}}{\pi D_{pin}^2}. \tag{2.53}$$

where $\rho_{el,int}$ is the isotropic, temperature dependent electrical resistivity of the pin.

Unlike TEM pellets and pins, the number of interconnectors is approximated to be the number of pins minus half of unity. This is due to the number of interconnectors in one row being equal to one less the number of pins in said row. Simultaneously, there exist a diagonal interconnector that acts as a transitional segment between each row. Therefore, an additional half of the interconnector is approximated to exist in each row.

As shown in figure 2.8, these elements are connected electrically in series. Therefore, the electrical resistance of the iTED can be defined as:

$$R_{el,tot} = \sum_{i=1}^{N} M^i \left(R_{el,pin}^i + R_{el,N}^i + R_{el,P}^i\right) + \left(M^i\right) R_{el,int}^i \tag{2.54}$$

where the superscript denotes the index of the row being evaluated.

Given the open-circuit voltage and the electrical resistance of the iTED, the maximum power transfer theorem defined by Jacobi is used to evaluate the steady-state current of the device. The maximum amount of electrical power can be obtained from the open-circuit voltage when a load element with an equivalent resistance of the iTED is used. The steady-state current is carried by these two elements. Therefore, the steady-state current can be defined as:

$$I = \frac{V_{oc}}{2R_{el,tot}}. \tag{2.55}$$

2.2 Solution Methodology

In the following section, a solution methodology is proposed to simultaneously solve the aforementioned set of mathematical equations in an iterative fashion. Considerations for temperature-dependent material properties and an iterative solution methodology that allows for convergence of all conserved quantities are made.

The incorporation of temperature dependency is one aspect of the novelty in this work. Cases exist where properties are evaluated at a single temperature value. There exist a subset of cases that evaluate the properties of the thermoelectric materials (i.e $\alpha_{N,P}$) and the exhaust (i.e $\lambda_{air}, \mu_{air}, \rho_{air}, Pr_s, Pr_{air}$) at single temperature values, which assumes said temperature is uniform in the domain of which they are evaluated in. There are also cases where material properties are evaluated about a temperature bound defined by a hot- and cold-side temperature. Properties of the thermoelectric materials (i.e $\rho_{el,(N,P)}, \lambda_{N,P}, \tau_{N,P}$), pin-fin heat exchanger (i.e $\rho_{el,pin}, \lambda_{pin}$), interconnectors (i.e $\rho_{el,int}, \lambda_{int}$), ceramic substrates (i.e λ_{cer}) and exhaust (i.e $C_{p,air}$) are evaluated in sub-domains where temperature bounds exist. As a result, these properties will be evaluated as the integral average, evaluated between the cold-side temperature (T_c) and the hold-side temperature (T_h) divided by the difference of the two temperatures. For a generic property (β) that is a function of temperature and evaluated about a temperature bound, the property is expressed as:

$$\beta(T) = \frac{1}{\Delta T} \int_{T_c}^{T_h} \beta(T) dT. \tag{2.56}$$

Tables 2.1 - 2.2 and 2.3 provide the coefficients for the thermo-physical properties of air, and aluminum and aluminum-oxide, respectively. Table 2.4 provides coefficients for the polynomial fits for the thermoelectric materials. Using said coefficients, a generic property (β) is expressed as:

$$\beta(\mathrm{T}) = \sum_{k=0}^{n} C_k \mathrm{T}^k \tag{2.57}$$

where k is the index of the property's coefficient C and n is the number of coefficients given for said property.

Given that material properties are a function of the temperatures that have yet to be solved, governing Eqs. 2.2 - 2.55 must be solved in an iterative fashion until convergence of all conserved quantities in the system of said equations is achieved. Empirical data supplied by Chandra and Žukauskas is also used to satisfy the following unknown variables f_c, f_p and X.

Initialized values for nodal temperatures and electrical current in the solid domain are estimated. Nodal temperatures are determined using a thermal resistance network shown in figure 2.4 using temperature boundary conditions for a given configuration and treating all thermal resistances as unity. Electrical current is taken to be 1 [μA]. This value was chosen so as to not overestimate the Joule, Thomson and Peltier heat contributions in the thermoelectric materials. The governing equations are then solved repeatedly using solutions determined from the previous iteration as inputs for the current iteration. This is done until all values of temperature, heat flux and electrical current of the current iteration achieves convergence. Convergence is achieved for a solution (γ) when its estimated relative error (ϵ) is less than or equal to a specified tolerance level. The estimated relative error is defined as:

$$\epsilon^j = \left| \frac{\gamma^j - \gamma^{j-1}}{\gamma^{j-1}} \right| \tag{2.58}$$

where the superscript denotes the iteration number. Once convergence of all conserved quantities has been achieved, device performance solutions of the iTED can be solved. The steps for the iterative approach are as follows:

1. Prescribe inlet conditions (Reynolds number, temperature) of the exhaust.
2. Initialize the steady-state electrical current and initial temperatures at each node in the solid domain (T_{pin}, $T_{N,h}$, $T_{P,h}$, $T_{N,c}$, $T_{P,c}$, $T_{int,h}$, $T_{int,c}$, $T_{cer,h}$, $T_{cer,c}$, $T_{hex,c}$) such that they reflect the direction of heat from the heat source to the heat sink.
3. Solve the thermal resistances for each of the components within the system using the temperatures found in Step 1 and Eqs. 2.2-2.5, 2.22-2.24 and 2.43 - 2.47.
4. Solve the hot-side and cold-side heat fluxes from Eqs. 2.21 and 2.42 using the temperatures found in Step 1.

5. Re-solve the nodal temperatures from the hot-side heat exchanger to the cold-side heat exchanger using the electrical current from Step 1, the thermal resistances solved in Step 2 and the heat fluxes solved in Step 3 using Eq. 2.21 for the hot-side branch, Eqs. 2.21, 2.25 - 2.42 for the TEM junction temperatures and Eq. 2.42 for the cold-side branch.
6. Repeat steps 2 through 4 using the re-solved nodal temperatures found in Step 4 for Steps 2 and 3 until the estimated relative error of component-wise heat fluxes and nodal temperatures in the solid domain is less than 1^{-10}.
7. Use Eq. 2.19 and the fully converged hot-side heat flux from Step 5 to solve the free stream temperature (T_{air}^{i+1}) in the next C$\forall$ until its estimated relative error is less than 1^{-10}. (Note: an empirical correlation relating specific enthalpy and temperature referenced to 293.15 [K] is used for initial guesses of temperature for the first and last row).
8. Solve the pressure drop, total heat extracted and potential difference in the current row using Eqs. 2.7 - 2.15, Eqs. 2.19-2.20 and Eq. 2.49 respectively.
9. Solve the free stream velocity and temperature in the next C$\forall$ using Eqs. 2.17.
10. Repeat steps 1 through 8 using the free stream temperature and velocity calculated in Steps 6 and 8 for every row in the fluids domain.
11. Re-solve the electrical current using Eq. 2.32 and Eqs. 2.50 - 2.55
12. Repeat steps 1 through 10 using the electrical current found in Step 10 instead of the estimated value from Step 1 until the estimated relative error for electrical current is less than 1^{-10}.

Steps 1 - 12 are succinctly shown in the flow chart shown in figure 2.9.

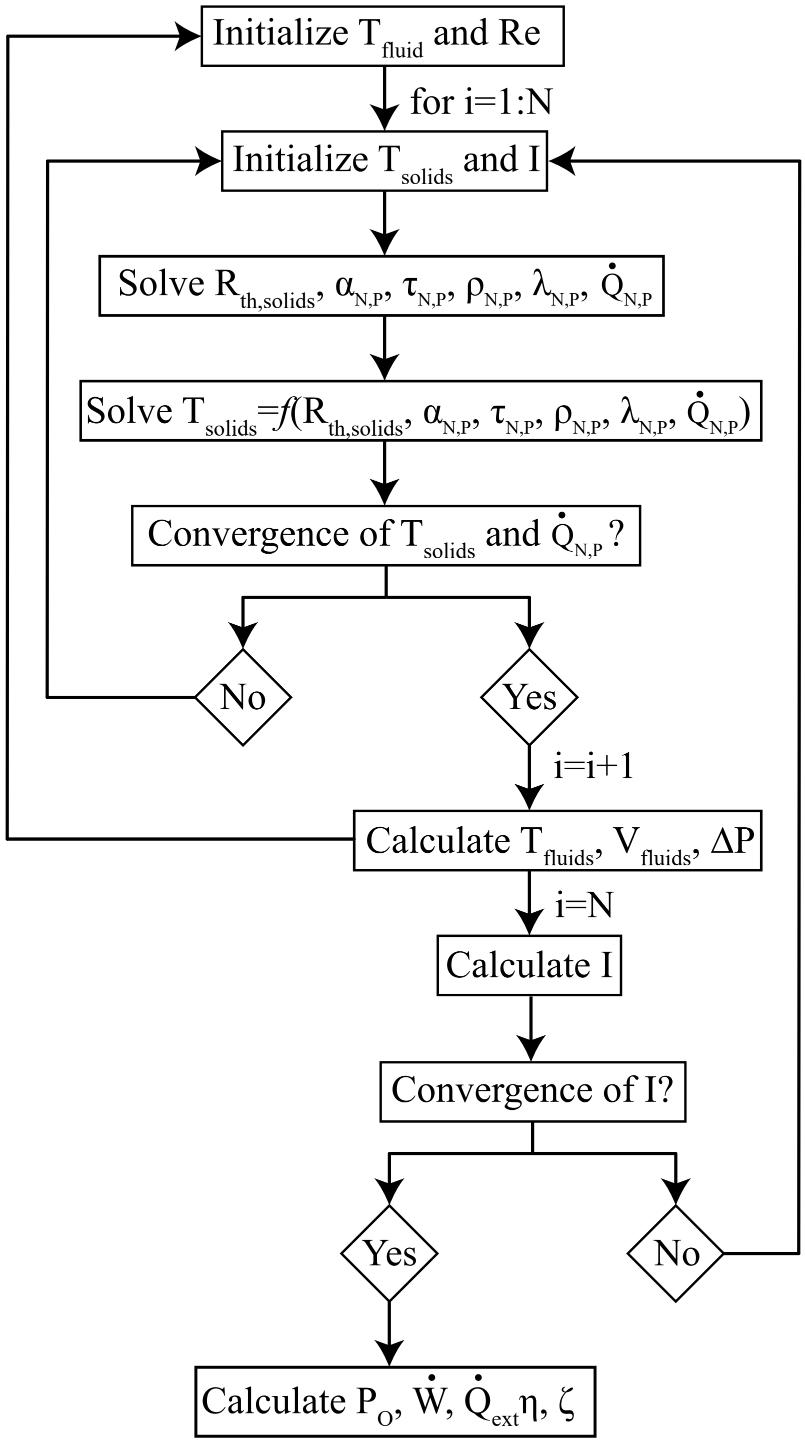

Figure 2.9: Flow chart of the solution methodology

Table 2.1: Coefficients for polynomial expressions used for temperature dependent thermal properties of exhaust gas treated as air

Temperature Dependent Thermal Properties of Air			
Coefficients	$C_{p,air}$ [kJ-kg^{-1}K^{-1}]	λ_{air} [Wm^{-1}K^{-1}]	$\mathscr{H}_{air}$ [kJ-kg^{-1}]
C_0	$-2.510583845996755 \cdot 10^{-7}$	$-1.495332662848001 \cdot 10^{-3}$	-10.5280149597594
C_1	$7.644215355586113 \cdot 10^{-8}$	$1.021911946960166 \cdot 10^{-4}$	1.03366729510056
C_2	$4.654143620499639 \cdot 10^{-11}$	$7.619562086824506 \cdot 10^{-7}$	-
C_3	$-1.338615668759098 \cdot 10^{-12}$	$-1.486884159237331 \cdot 10^{-8}$	-
C_4	$9.389665890526664 \cdot 10^{-15}$	$1.433819833176523 \cdot 10^{-10}$	
C_5	$-4.412211504098053 \cdot 10^{-17}$	$-9.144892530792689 \cdot 10^{-13}$	-
C_6	$1.545184004552245 \cdot 10^{-19}$	$4.162788046998359 \cdot 10^{-15}$	-
C_7	$-4.162639297794861 \cdot 10^{-22}$	$-1.401419105750576 \cdot 10^{-17}$	-
C_8	$8.717259785504756 \cdot 10^{-25}$	$3.552922870621147 \cdot 10^{-20}$	-
C_9	$-1.418656766891524 \cdot 10^{-27}$	$-6.825537072648714 \cdot 10^{-23}$	-
C_{10}	$1.777955973412966 \cdot 10^{-30}$	$9.895360787316968 \cdot 10^{-26}$	-
C_{11}	$-1.683670596972462 \cdot 10^{-33}$	$-1.066136765380712 \cdot 10^{-28}$	-
C_{12}	$1.165290648616006 \cdot 10^{-36}$	$8.279993186699540 \cdot 10^{-32}$	-
C_{13}	$-5.561472820389447 \cdot 10^{-40}$	$-4.382729828296852 \cdot 10^{-35}$	-
C_{14}	$1.635869598371633 \cdot 10^{-43}$	$1.415504830714931 \cdot 10^{-38}$	-
C_{15}	$-2.234828460469022 \cdot 10^{-47}$	$-2.104996356665985 \cdot 10^{-42}$	-

Table 2.2: Coefficients for polynomial expressions used for temperature dependent inertial properties of exhaust gas treated as air

Temperature Dependent Inertial Properties of Air		
Coefficients	μ_{air} [Pa-s]	ρ_{air} [kg-m^{-3}]
C_0	-2.510583845996755·10^{-7}	15.71450152389037
C_1	7.644215355586113·10^{-8}	-3.119297387879921·10^{-1}
C_2	4.654143620499639·10^{-11}	3.743540895135033·10^{-3}
C_3	-1.338615668759098·10^{-12}	-3.065419902627119·10^{-5}
C_4	9.389665890526664·10^{-15}	1.823021830651361·10^{-7}
C_5	-4.412211504098053·10^{-17}	-8.161820195506108·10^{-10}
C_6	1.545184004552245·10^{-19}	2.809645541111718·10^{-12}
C_7	-4.162639297794861·10^{-22}	-7.522178899751919·10^{-15}
C_8	8.717259785504756·10^{-25}	1.572459176350643·10^{-17}
C_9	-1.418656766891524·10^{-27}	-2.559354040844368·10^{-20}
C_{10}	1.777955973412966·10^{-30}	3.210623006538871·10^{-23}
C_{11}	-1.683670596972462·10^{-33}	-3.044302579995492·10^{-26}
C_{12}	1.165290648616006·10^{-36}	2.109949141192753·10^{-29}
C_{13}	-5.561472820389447·10^{-40}	-1.008392900450303·10^{-32}
C_{14}	1.635869598371633·10^{-43}	2.970043445459524·10^{-36}
C_{15}	-2.234828460469022·10^{-47}	-4.062510140242369·10^{-40}

Table 2.3: Polynomial expressions for temperature dependent properties of interconnector and pins treated as aluminum and ceramic substrates treated as Alumina Oxide

Aluminum Temperature Dependent Properties	
$\lambda_{\mathrm{Al}}\,[\mathrm{Wm^{-1}K^{-1}}]$	$= (402.1043)\mathrm{T} + (6.874{\cdot}10^{-2})$
$\rho_{el,\mathrm{Al}}\,[\Omega\mathrm{m}]$	$= (7.1220{\cdot}10^{-11})\mathrm{T} + (1.5113{\cdot}10^{-8})$
Aluminum Oxide Temperature Dependent Properties	
$\lambda_{\mathrm{Al_2O_3}}\,[\mathrm{Wm^{-1}K^{-1}}]$	$= (1.590936166093673{\cdot}10^{-21})\mathrm{T}^8 + (-8.888214436027726{\cdot}10^{-18})\mathrm{T}^7 + (1.982759392076562{\cdot}10^{-14})\mathrm{T}^6 + (-2.274431414830283{\cdot}10^{-11})\mathrm{T}^5 + (1.435688825890332{\cdot}10^{-8})\mathrm{T}^4 + (-4.961844485882746{\cdot}10^{-6})\mathrm{T}^3 + (9.355387514955410{\cdot}10^{-4})\mathrm{T}^2 + (-1.458207398665192{\cdot}10^{-1})\mathrm{T} + (36.923204985247708)$

Table 2.4: Polynomial expressions for temperature dependent properties of N- and P-Type Materials of Ag-Na semiconductor pairs

N-type Temperature Dependent Properties			
Coefficients	α_N [V-K^{-1}]	λ_N [W-m^{-1}K^{-1}]	$\rho_{el,N}$ [Ω-m]
C_0	-2.56145854736198$\cdot 10^{-3}$	5.47063393683237$\cdot 10^{1}$	8.20729721497388$\cdot 10^{-4}$
C_1	3.64698151674484$\cdot 10^{-5}$	-6.55298213920936$\cdot 10^{-1}$	-1.11491872022586$\cdot 10^{-5}$
C_2	-2.15109875689092$\cdot 10^{-7}$	3.39689599143903$\cdot 10^{-3}$	6.18825647429766$\cdot 10^{-8}$
C_3	6.49391089979452$\cdot 10^{-10}$	-9.30723131891380$\cdot 10^{-6}$	-1.78779907117923$\cdot 10^{-10}$
C_4	-1.07315231016137$\cdot 10^{-12}$	1.41046103507239$\cdot 10^{-8}$	2.83718320981461$\cdot 10^{-10}$
C_5	9.20358537130714$\cdot 10^{-16}$	-1.11922763127352$\cdot 10^{-11}$	-2.33750677388805$\cdot 10^{-16}$
C_6	-3.20211846500991$\cdot 10^{-19}$	3.63421886723793$\cdot 10^{-15}$	7.81287156202503$\cdot 10^{-20}$
P-type Temperature Dependent Properties			
Coefficients	α_P [V-K^{-1}]	λ_P [W-m^{-1}K^{-1}]	$\rho_{el,P}$ [Ω-m]
C_0	-1.36589737015684$\cdot 10^{-3}$	1.10029312339031$\cdot 10^{1}$	-1.54141521393943$\cdot 10^{-3}$
C_1	1.82288315590685$\cdot 10^{-5}$	-8.06341803814208$\cdot 10^{-2}$	2.07956226027221$\cdot 10^{-5}$
C_2	-1.01050133039802$\cdot 10^{-7}$	2.90944639598397$\cdot 10^{-4}$	-1.14252596939032$\cdot 10^{-7}$
C_3	3.04259091207328$\cdot 10^{-10}$	-5.64280445071754$\cdot 10^{-7}$	3.27548789104988$\cdot 10^{-10}$
C_4	-5.01471471424515$\cdot 10^{-13}$	5.84439024194443$\cdot 10^{-10}$	-5.16115084380221$\cdot 10^{-13}$
C_5	4.29333868014866$\cdot 10^{-16}$	-2.92763677023191$\cdot 10^{-13}$	4.25077235567454$\cdot 10^{-16}$
C_6	-1.50081382644629$\cdot 10^{-19}$	5.23808654960887$\cdot 10^{-17}$	-1.43160948020673$\cdot 10^{-19}$

2.3 Device Performance Solutions

The convergence of all conserved quantities across the entire iTED domain yield numeric values for temperatures in the solid and fluid domain, steady-state electrical current, pressure drop per row and heat extracted per row. Given these values, performance solutions such as power output (P_o), thermal conversion efficiency (η_{th}) and performance index (ζ) can be evaluated for a given set of inlet conditions and a device configuration. Given the converged solutions of steady-state electrical current and the open-circuit voltage, the electrical power output is defined as:

$$P_o = I^2 R_{el,tot}. \tag{2.59}$$

After quantifying the contributions of pressure drop from the pin-fin heat exchanger, head loss and corbels, the total pressure drop from the inlet to the outlet of the iTED is determined via superposition. The total pressure drop across the iTED is expressed as:

$$\Delta P = \sum_{i=1}^{N} (\Delta P^i_{pins} + H^i_{\ell,2} + \Delta P^i_c) + H_{\ell,1} + H_{\ell,3} \tag{2.60}$$

where the superscript denotes the index of the row being evaluated. Once evaluated, the pumping power required to overcome the pressure drop can be quantified using the following expression:

$$W = \frac{\dot{m}\Delta P}{\bar{\rho}_{air}}. \tag{2.61}$$

The mass flow remains constant throughout the iTED channel because it adheres to continuity. The term $\bar{\rho}_{air}$ is the arithmetic mean of the working fluid density at the channel's inlet and outlet.

Heat is extracted from the exhaust by the pins via the convective heat transfer effect. The quantity of heat extracted by an individual pin is defined by Eq. 2.19 shown below:

$$Q_{pin} = \dot{m}\tilde{C}_p (T^{i+1}_{air} - T^i_{air}). \tag{2.62}$$

There are M pins per row that extract an equivalent quantity of heat within their respective C∀'s. Given that there are N rows of pins within the iTED, the total heat extracted by the pin-fin heat exchanger across the iTED can be expressed as:

$$Q_{ext} = \sum_{i=1}^{N} M^i(\dot{Q}^i_{pin}) \tag{2.63}$$

where the superscript denotes the row number being evaluated.

The magnitude of the electrical power produced is measured relative to the pumping power needed to push the working fluid and the heat it extracts from the medium. The thermal conversion efficiency quantifies this. Given the power output, pumping power and extracted heat, the thermal conversion efficiency can be determined. It is given by the expression:

$$\eta_{th} = \left(\frac{P_o}{Q_{ext} + W}\right). \tag{2.64}$$

The performance index relates the electrical power output to the pumping power needed to push the exhaust given inlet conditions and device configurations. It is given by the expression:

$$\zeta = \frac{P_o}{W} - 1. \tag{2.65}$$

A value of ζ greater than zero indicates the device is producing more power that is what is required to move the fluid through the pin-fin heat exchanger.

3.0 Results And Discussion

The order of operations described in Section 2.2 was performed for various independent inlet thermal-fluid conditions, geometric configurations, and cold-side atmospheric boundary conditions, as listed in table 3.1. The set of parameters listed in table 3.1 reflects a design space of 42,000 unique geometric configurations operating under 1,000 unique thermal-fluid conditions. Thus, 42,000,000 scenarios were analyzed through a parametric study. In this chapter, model validation, rigorous parametric study, and non-linear regression analysis are presented. The model proposed herein was validated to an existing, thermal-fluid-electric coupled numeric modeled executed in ANSYS Fluent, as described in Section 3.1. The results of the parametric study and the non-linear regression analysis will be presented and used to develop a set of equations that can be used for further design optimization of the iTED with regards to its performance solutions.

The performance solutions of interest are the electrical power output, thermal conversion efficiency and performance index. In Section 3.1, the effects of the independent variables are discussed to determine which have the greatest linear correlation with the performance solutions. This is done by determining Spearman rho coefficients (SCC's) via uni-variate linear regression. Statistical values are presented to exhibit the validity of the SCC's by highlighting the samples taken, the domain they exist in and the quantity of outliers. The independent variables, whose SCC's significantly differ from zero, will then be selected for defining each performance solution as a function thereof.

In Section 3.2, the maximum numeric value for each performance solution are presented along with their respective configurations. These configurations will be the basis for a set of equations that prioritizes the maximum value of one performance solution over another. The generic form of these sets of equations are then presented.

In Section 3.3, each performance solution is plotted against their respective independent variables chosen from Section 3.1. These performance solutions will be plotted over a finer domain to illustrate its behavior with respect to the independent variables. The results of a uni-variate non-linear regression analysis are presented.

Table 3.1: Independent parameters and their numeric values

Independent Parameters	
Parameter, Variable, [Units]	Range
Inlet Temperature, $T_{\infty,h}$, [K]	[350, 400, 450, 500, 550, 600, 650, 700]
Inlet Reynolds Number, Re	[$3{\cdot}10^3$, $6{\cdot}10^3$, $9{\cdot}10^3$, $12{\cdot}10^3$, $15{\cdot}10^3$]
Maximum Pins Per Row, M_{max}	[4, 6, 10, 25, 50, 75, 100]
Number of Rows, N	[10, 20, 30, 40, 50, 60, 70, 80, 90, 100]
Pin Diameter, D_{pin}, [mm]	[1.5875, 3.1750, 4.7625, 6.3500]
Pin Height, H_{pin}, [mm]	[12.700, 18.275, 23.850, 29.425, 35.000]
Material Length, $t_{N,P}$, [mm]	[0.5, 0.7, 0.8, 1, 3.5, 5]
Cold HEX Area, $A_{hex,c}$, [m^2]	[$1{\cdot}10^{-5}$, $1{\cdot}10^{-4}$, $1{\cdot}10^{-3}$, $1{\cdot}10^{-2}$, $1{\cdot}10^{-1}$]
Convection Coefficient, h_c, [Wm^{-2}K^{-1}]	[300, 400, 500, 750, 1000]
Heat Sink Temperature, $T_{\infty,c}$, [K]	[273.15, 283.15, 293.15, 303.15, 313.15]

Finally, in Section 3.4 the results of a multivariate non-linear regression analysis are presented. The coefficients are determined using the iterative least squares estimation algorithm using a convergence tolerance of 1^{-9}. The coefficient estimates and model fit functions from Section 3.3 with the greatest R^2 value are used for the required initial estimates of the least square estimation algorithm. The resultant non-linear multivariate models are presented along with their respective R^2 value.

3.1 Validation

Previous research efforts have been made to use high-fidelity, Finite Volume Method (FVM)-based models to simultaneously characterize the behavior of the thermal-fluid and thermal-electric, i.e. fully-coupled thermal-fluid-electric behavior, of an iTED. Details about the FVM modeling, including the casting of the constitutive thermoelectric equations in a finite volume form, and the application of Reynolds-Average Navier Stokes (RANS) equations, of the iTED can be found in [54, 55, 56, 53]. To mimic the behavior of the numeric model, which imposed a Dirichlet boundary condition on the top and bottom of the upper and lower electrical interconnectors, the following modifications to cold-side branch, as shown in figure 2.4, were made to the analytic model:

1. The grease between the interconnector and ceramic and ceramic and exchanger was removed, and the fifth and seventh terms of Eq. 2.42 containing the the variable described by Eq. 2.45 was omitted;
2. The ceramic plate was removed, and the sixth term of Eq. 2.42 containing the variable described by Eq. 2.46 was omitted;
3. The heat exchanger was removed, and the eight term of Eq. 2.42 containing the variable described by Eq. 2.47 was omitted;
4. A temperature of 300 [K] was imposed on the exterior surface of the interconnector. The fourth term of Eq. 2.42 was modified such that $T_{int,c}$ was equal to 300 [K].

The parameters that were used for the validation study, mimicking those of the numerical study, are as follows:

1. The flow rate was varied between Re=3,000 and 15,000 in increments of 3,000;
2. The inlet fluid temperature was varied between T_{in} =350 [K] and 750 [K] in increments of 50 [K]
3. The flow channel height was kept invariant at 15.875 [mm], which is the same as the pin height;
4. The flow channel width was kept invariant at 31.85 [mm];
5. The pin and thermoelectric material diameter was kept invariant at 3.175 [mm],

6. The transverse pin spacing was $S_T = 2.5D_{pin}$;
7. The longitudinal pin spacing was $S_L = 2D_{pin}$;
8. There were 10 rows of pins, alternating between 3 and 4 pins per row, totalling 35 pin;
9. The thermoelectric material height was kept invariant at 1 [mm].

The entirety of the device's thermal-electric performance is predicated upon the temperature difference established across the junctions. The establishment of this gradient is dependent upon many factors, including but not limited to, the convective heat transfer coefficient developed on the pin-fin surface, the thermal resistance of heat exchange and thermoelectric systems, the quantity of heat removed by the Peltier effects, as well as the quantities of heat produced by the Peltier, Thomson and Joule effects. It is noted that the use of Eqs. 2.29 and 2.30 introduces error in terms of predicting the desired quantity, namely heat input, given junction temperatures, or conversely, junction temperatures, given heat input, due to the assumptions made during the construction of said equations. The crux of these equations is that the material properties are assumed constant [57, 58]. Although integral-averaged material properties are used to provide a better description of the constant populating the equation, deviation from an assumption-free FVM is expected.

We first compare the average hot-side junction temperature, T_{avg}, as predicted by the numeric and analytic models, for the range of flow rates and inlet fluid temperatures. This comparison is shown in figure 3.1, where the analytic data is overlayed to the numeric data. It is noted the error bars associated with the numeric values on all the following validation figures comes from the summation of numeric uncertainty associated with discretization and model form uncertainty. The error bars represent a 95% confidence interval. The maximum disagreement occurs at Re=3,000 and T_{in} = 750 [K], which reflects a percent difference of 10.0%. It is noted that as Re increases for a fixed T_{in}, the percent difference decreases. For instance, given a T_{in} of 750 [K], the percent difference decreases from 10.0% to 6.29% as Re increases from 3,000 to 15,000.

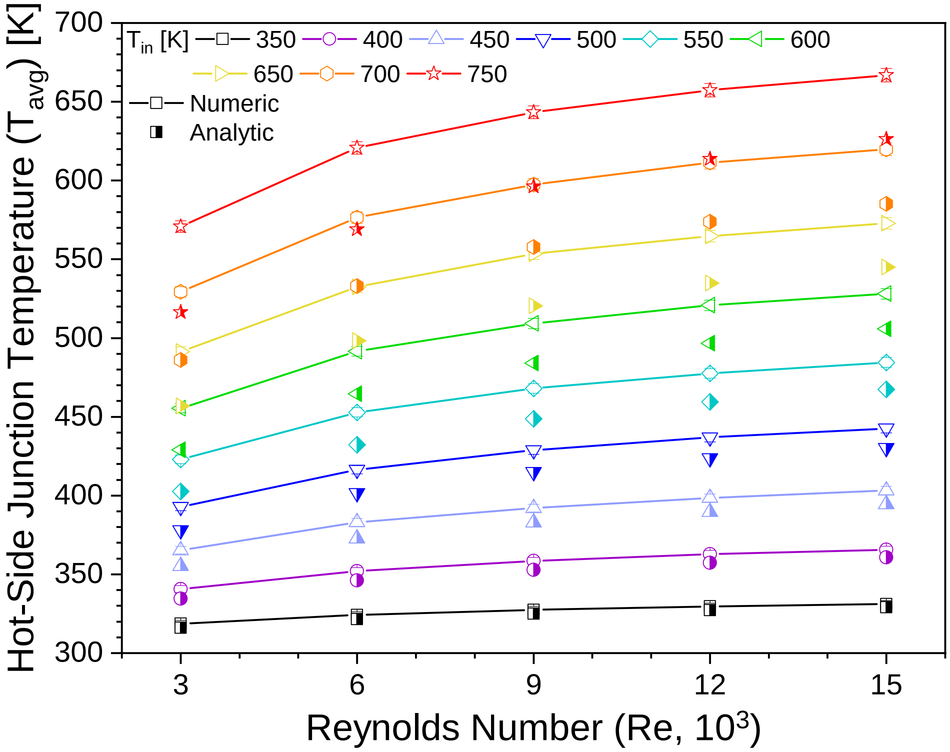

Figure 3.1: Comparison of analytic to numeric results for average hot-side junction temperatures, T_{avg}, for various Re and T_{in} values

As T_{in} increases for a fixed Re, the percent difference once again increases. For instance, for a fixed Re of 15,000, as T_{in} increases from 350 [K] to 750 [K], the percent difference increases from 0.64% to 6.29%. It is seen there is more of an under-prediction of T_{vag} at low Re, and this under-prediction decreases as Re increases. When T_{in} is less than 550 [K], and for all Re, the percent difference is sub-5%, indicating good agreement between the two models. This can be attributed to both the predictions of RANS models and empirical correlations at such low Re, which is in the transition region between laminar and turbulent flow. Although there is an under-prediction, the trend of T_{avg} follows that of the numeric data, illustrating a monotonic, near-linear increase with T_{in}, and an increase with Re that fits a power law.

Next, we compare the calculated internal electrical resistance of the device, as shown in figure 3.2. It is seen that the predictions for $R_{el,tot}$ are in agreement with those predicted by the numeric model over the range of Re and T_{in} values. Once again, this is an under-prediction of values calculated by the analytic model in comparison to the numeric for low Re, in particular, when Re equals 3,000 and 6,000. The maximum percent difference is 9.61% at a maximal inlet temperature and minimum flow rate. Above a flow rate of Re=6,000, the predicted analytic values are within the range of uncertainty of the numeric results, indicating agreement between the models.

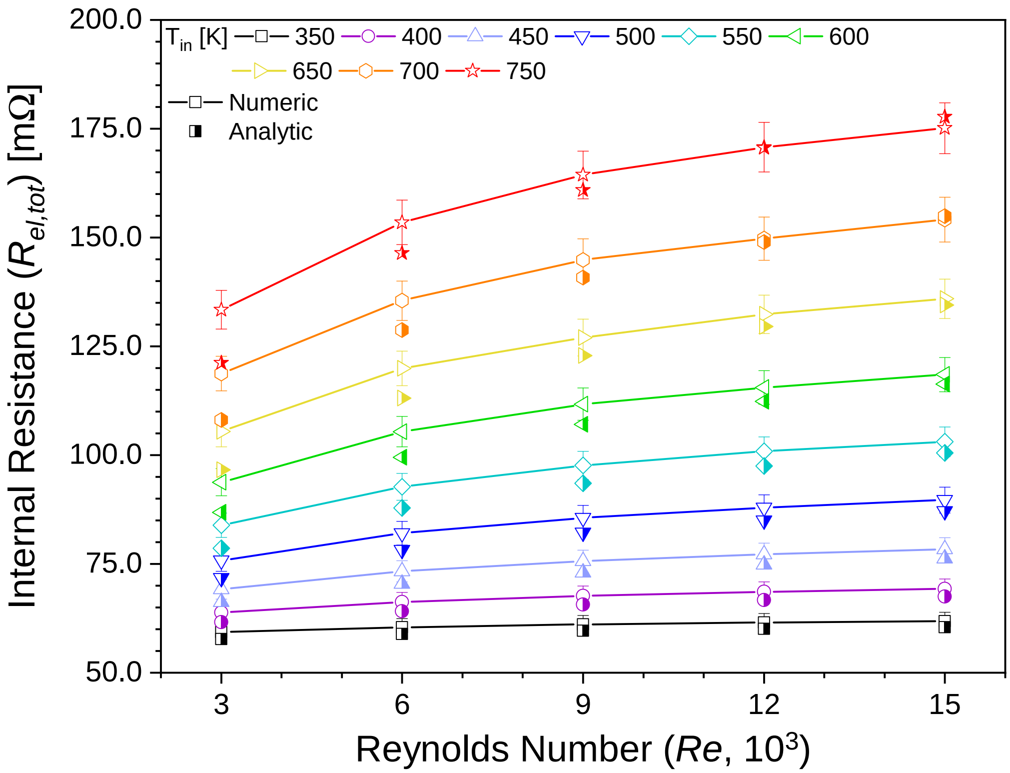

Figure 3.2: Comparison of analytic to numeric results for total internal electrical resistance, $R_{el,tot}$, for various Re and T_{in} values

The predictions of Seebeck voltage, denoted as V_{oc}, which is commonly referred to the open-circuit voltage, which is the Seebeck voltage during an open-circuit situation, is compared to numeric predictions in figure 3.3. Note the determination of the Seebeck voltage is determined by Eqs. 2.48 - 2.50, and is dependent upon the the temperature difference established across the junctions, as well as the temperature dependent Seebeck coefficients of the n- and p-type materials. It is seen the disagreement between the numeric and analytic results is exacerbated by low-flow conditions, and the difference increases with increasing inlet temperatures. The maximum percent difference occurs at Re=3,000 and T_{in}=750 [K], with a value of 27.46%. The percent difference increases by increase the flow rate, such that as Re=15,000 for a T_{in} of 750 [K], the percent difference is more than halved.

The reason for the disagreement is solely due to the developed temperature difference across the device. With an under-predicted temperature gradient across the junctions, there is a lesser developed Seebeck voltage due to a smaller ΔT. Simultaneously, the magnitude of the Seebeck coefficients $\alpha_{N,P}$ will be lesser than that of the numeric model, for the lesser temperature gradient imposed across the material results in a lesser electromotive force characterized by this coefficients. These two happenings compound, resulting in a substantially lesser V_{oc} prediction than the numeric values. However, the trend of behavior of V_{oc} with respect to Re and T_{in} follows that of numeric predictions.

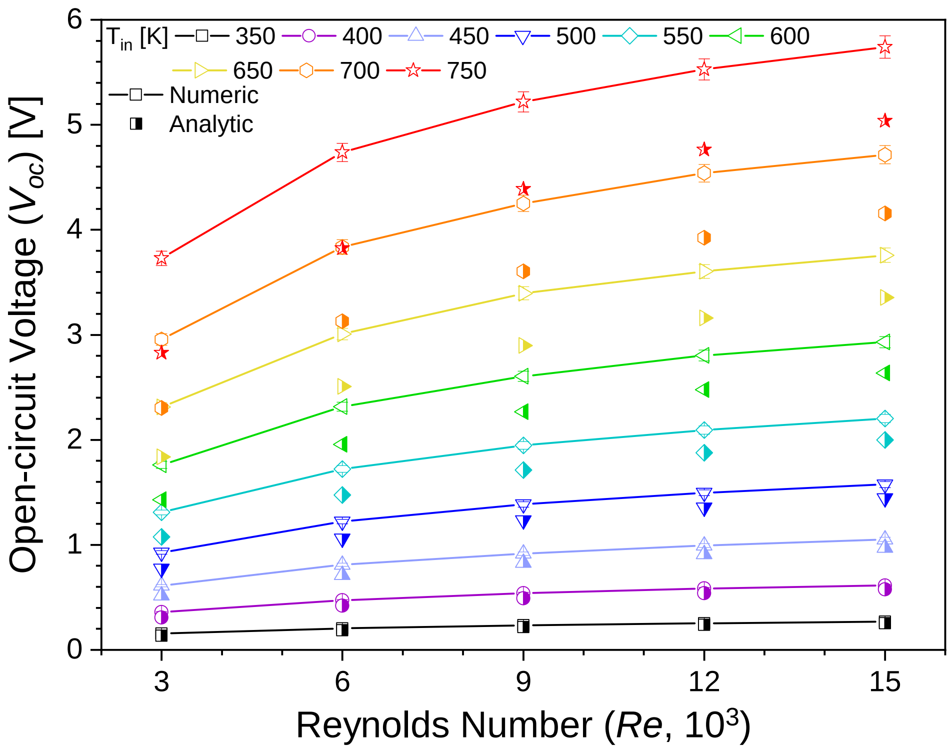

Figure 3.3: Comparison of analytic to numeric results for Seebeck voltage, V_{oc}, for various Re and T_{in} values

With an under-predicted Seebeck voltage, there will be an obvious under-prediction of current I, as shown in figure 3.4. The current is calculated via Eq. 2.55 as a result of the

Seebeck voltage per twice the internal electrical resistance, maximizing power output. Once again, a trend of increasing disagreement with low Re values is observed. The maximum percent difference occurs at a maximum Re and minimum T_{in} value, with a value of 17.97%; this value decreases to 14.51% by increasing Re to a value of 15,000, and reaches a minimum of 3.12% at a maximal Re and minimal T_{in}. The trend of predictions of I with respect to Re and T_{in} is aligned with the numeric predictions.

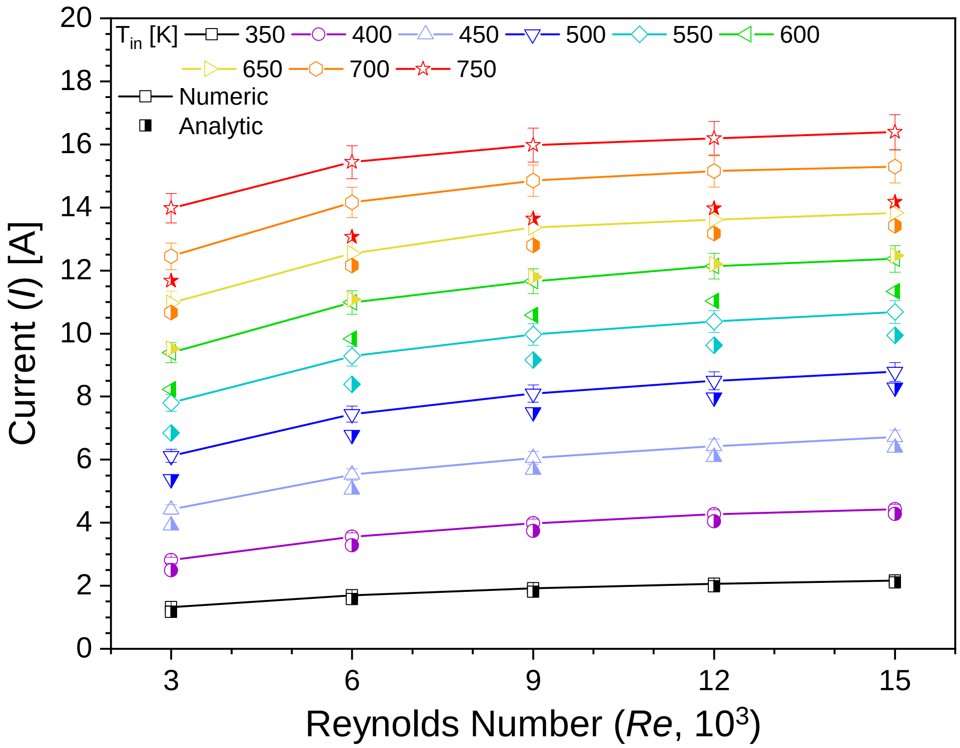

Figure 3.4: Comparison of analytic to numeric results for current, I, for various Re and T_{in} values

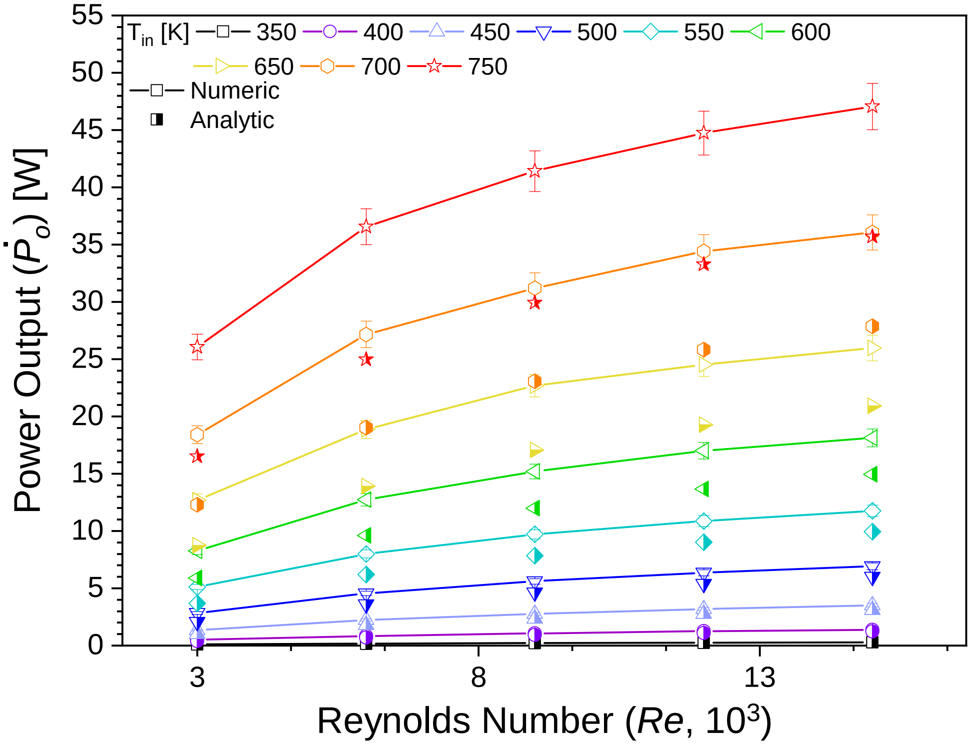

Figure 3.5: Comparison of analytic to numeric results for power output, $\dot{P}_o$, for various Re and T_{in} values

The power output, as defined by equation. 2.59, takes the square of the generated current, times the load resistance. With a high percent difference associated with the predicted current values by the analytic model, an even high percent difference associated with electrical power output values is expected, and observed, as seen in figure 3.5. The maximum percent difference occurs at minimal Re and maximal T_{in} values, with a value of 44.88%. The decrease in percent difference follows that observed when comparing analytic values of I to their numeric counterparts; increasing Re decreases this difference by a factor of 3.1 to 1.6 as T_{in} increases from a minimum to a maximum. Although prediction of P_o are substantially below those predicted by the numeric model for T_{in} greater than or equal to 600 [K], the trend of P_o follows that of the numeric values with respect to Re and T_{in}.

The agreement between the hydraulic behavior of the fluid, namely pressure drop through the channel and across the pin-fin array, between the analytic and numeric models is in better agreement than the preceding thermal-electric behavior. As seen in figure 3.6, the analytic predictions of pumping power are near or within the bounds of uncertainty of the numeric predictions for the entire range of Re and T_{in} values. The maximum percent difference occurs at Re=3,000 and $T_{in} = 750$ [K], with a value of 22.16%; this decreases to 9.39% with maximizing Re and to a value of 7.74% while decreasing T_{in} while maximizing Re. The trends of predictions are also in agreement.

The proposed analytic model over-predicts heat input with increasing T_{in}, as shown in figure 3.7. At low T_{in} values, up to and including 450 [K], and for all Re, the analytic predictions are almost all within the uncertainty of the numeric results. Although the numeric models achieved a y$^+$ less than unity, there is still differing behavior of the RANS-based models to experimental correlations used within the analytic model, and this is evidenced once T_{in} exceeds 450 [K]. The maximum percent difference occurs at the highest Re and T_{in} values, with a value of 56.285 %. Albeit the high percent difference, the trend of behavior as a function of Re and T_{in} is the same of the analytic and numeric models.

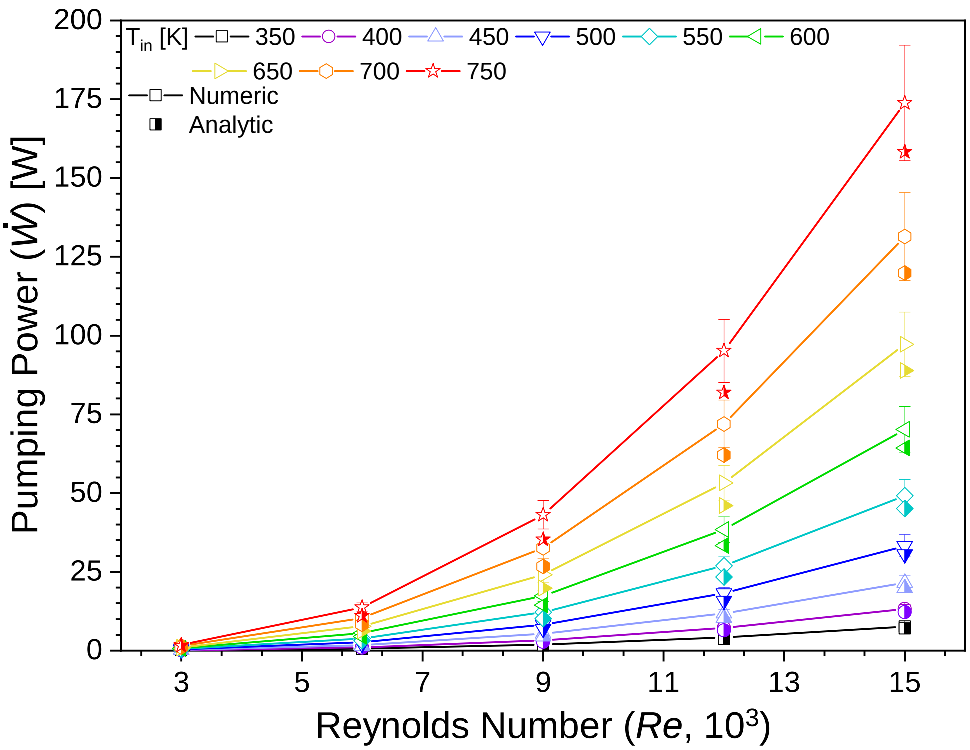

Figure 3.6: Comparison of analytic to numeric results for pumping power, $\dot{W}$, for various Re and T_{in} values

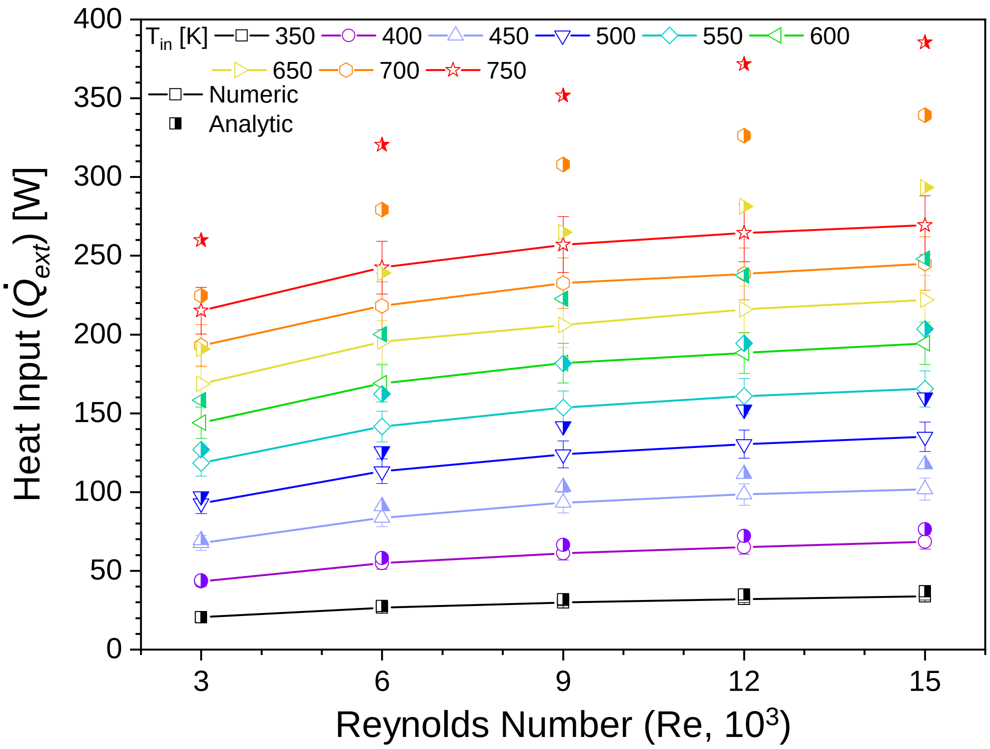

Figure 3.7: Comparison of analytic to numeric results for heat extracted, $\dot{Q}_{ext}$, for various Re and T_{in} values

The proposed analytic model substantially under-predicts the thermal conversion efficiency once T_{in} exceeds 350 [K] for all considered Re, as shown in figure 3.8. This is due to the under-prediction of power output and over-prediction of heat input. Although the analytic model is predicting half the efficiency at maximal T_{in} values, the behavior of η_{th} with respect to T_{in} and Re follow the same trend between modeling techniques.

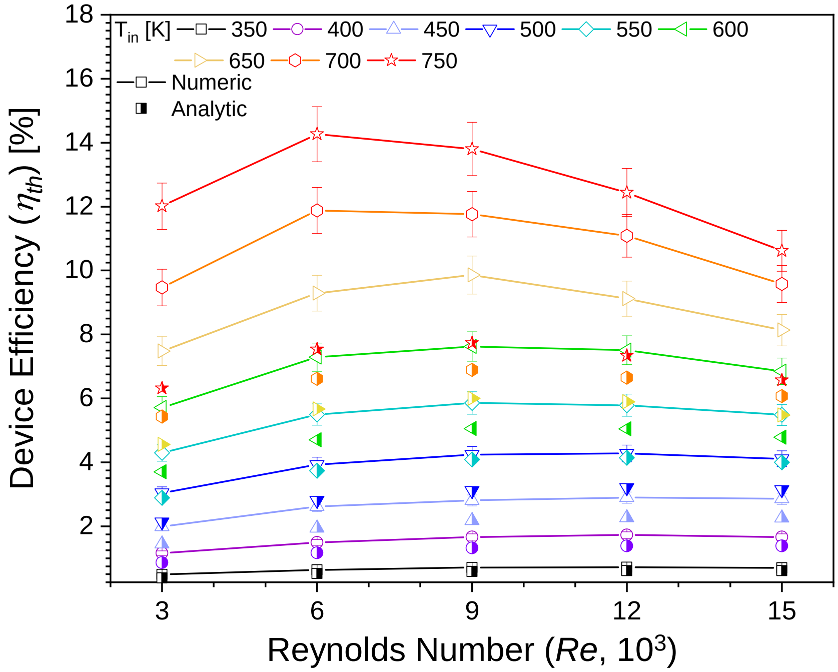

Figure 3.8: Comparison of analytic to numeric results for device thermal conversion efficiency, η_{th}, for various Re and T_{in} values

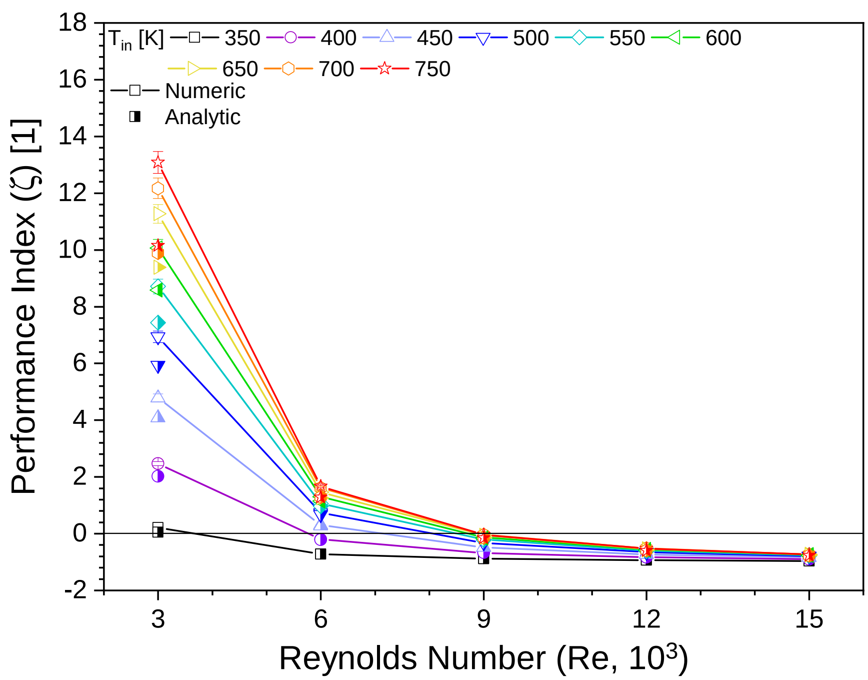

Figure 3.9: Comparison of analytic to numeric results for performance index, ζ, for various Re and T_{in} values

Lastly, when comparing the performance index of the analytic and numeric models, it is seen from figure 3.9 that the analytic model is in relatively better agreement with the numeric than previous predictions (i.e. thermal conversion efficiency), due to the better agreement of pumping power requirements. The deviation between the analytic and numeric is due to the under-prediction of the power output of the analytic model.

It can be seen by comparing performance metrics of the iTED predicted by the fully-coupled thermal-fluid-electric coupled model to its numeric counterpart, that there are situations of agreement and disagreement. Although the most sought-after numeric values, namely power output, pumping power, and device efficiency, as determined by the analytic model have relatively high average percent differences of 23.83%, 15.89% and 48.23%, respectively, they exhibit the same trends as the numeric values with respect to inlet thermal-fluid conditions. This is important, for the disparity between predictions can be rectified by the using of multi-fidelity modeling techniques. The low-fidelity and rapidly generated analytic results can be correlated to the few, high-fidelity numeric results, increasing the confidence of the predictions. As will be discussed in Section 4.2, the modeling presented within serves as the basis of a multi-fidelity modeling approach to generate reliable predictions of the iTED's performance applied to automotive WHR applications.

3.2 Linear Correlations

Data solutions that either did not adhere to the 10^{-9} residual criterion or fell out the applicable range of correlations were eliminated from the solution populations. Thus, 31,168,200 of the 42,000,000 configurations were able to be confidently analyzed. The solutions from these configurations were used as populations for uni-variate linear regression to determine the SCC's between each pair of numeric variables. The equation for the SCC between two populations is defined as:

$$\rho_{X,Y} = \frac{\text{cov}(X,Y)}{\sigma_X \sigma_Y} \tag{3.1}$$

where $\rho_{X,Y}$ is the SCC, X and Y are two random populations, the numerator term is the co-variance between said populations and σ is the standard deviation of a population. The SCC's mathematical algorithm was chosen because it assumes a monotonic relationships among ordinal variables and is generally practiced for large populations. The mathematical algorithm by which Pearson correlation coefficients are determined assume direct and proportional changes between ordinal variables. This was not an acceptable assumption given that the behavior of the performance solutions with respect to the independent variables are unknown. The mathematical algorithms by which Kendall's tau coefficients are determined assume monotonic behavior and are less susceptible to errors; however, the algorithm is $O(n^2)$ in complexity compared to that of Spearman rho's which is $O(n \log n)$ in complexity. Given the number of usable data points in the population, the SCC's can be determined approximately six times faster than the coefficients resultant from the Kendall tau mathematical algorithm.

The correlation matrix shown in figure 3.10 shows the SCC's between the independent variables listed in table 3.1 and the three resultant performance solutions. Given the correlation matrix, the independent variables with the most direct, linear influence for a given performance solution can be investigated with greater depth for uni-variate non-linear regression.

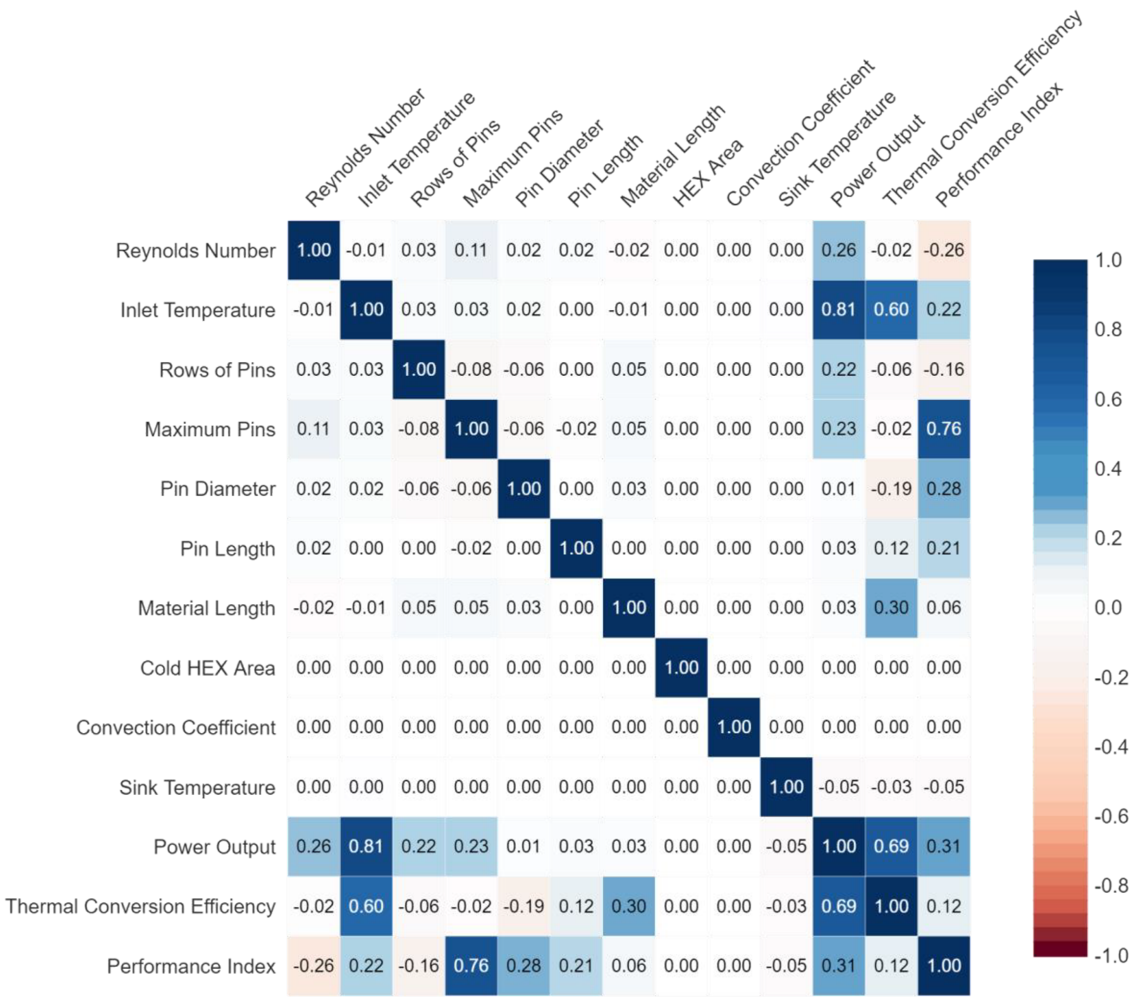

Figure 3.10: Correlation matrix of independent and dependent variables

Observing the correlation matrix, several assertions can be made based on the Spearman rho correlation measure:

1. The power output has relatively high positive correlations with the inlet fluid temperature, inlet Reynolds number, row of pins and the maximum number of pins per row compared to the remaining independent variables.
2. The thermal conversion efficiency has relatively high positive correlations with inlet temperature and thermoelectric material length as well as a relatively high negative correlation with the pin diameter compared to the remaining independent variables.
3. The performance index has the strongest negative linear correlation, among all solutions, with the inlet Reynolds number while also having relatively high positive correlations

with the maximum number of pins per row, pin diameter, inlet fluid temperature and pin length compared to the remaining independent variables.

3.2.1 Effect of Inlet Conditions

According to the SCC's shown in figure 3.10, the inlet conditions (i.e inlet Reynolds number and inlet fluid temperature) have significant linear correlations with the performance solutions. The only exception is the correlation between the inlet Reynolds number and the thermal conversion efficiency. The effects of inlet conditions on the performance solutions are examined in Sections 3.2.1.1 - 3.2.1.3.

3.2.1.1 Electrical Power Output The data distribution of the electrical power output is represented by the boxplots shown in figure 3.11a and b. Figure 3.11a is the data distribution for said performance solution grouped by inlet Reynolds numbers while figure 3.11b is the data distribution of the same solution grouped by inlet fluid temperatures. The population size, median, 75%-quartile, 25%-quartile, minimum and maximum values for the boxplots grouped by inlet Reynolds number and inlet fluid temperature are presented in tables 3.2 and 3.3 respectively.

Table 3.2: Statistical values of boxplots for electrical power output, with units of [W], grouped by inlet Reynolds number

Independent Variable: Inlet Reynolds Number						
Re	Population	Median	75%-Quartile	25%-Quartile	Maximum	Minimum
3,000	5,038,859	15.181	42.466	4.039	267.441	0.009
6,000	6,383,196	29.166	83.128	7.637	508.611	0.009
9,000	6,523,715	40.566	117.427	10.211	774.925	0.009
12,000	6,592,500	50.046	148.325	12.238	1,027.745	0.009
15,000	6,628,728	57.986	176.413	13.963	1,248.338	0.009

a)

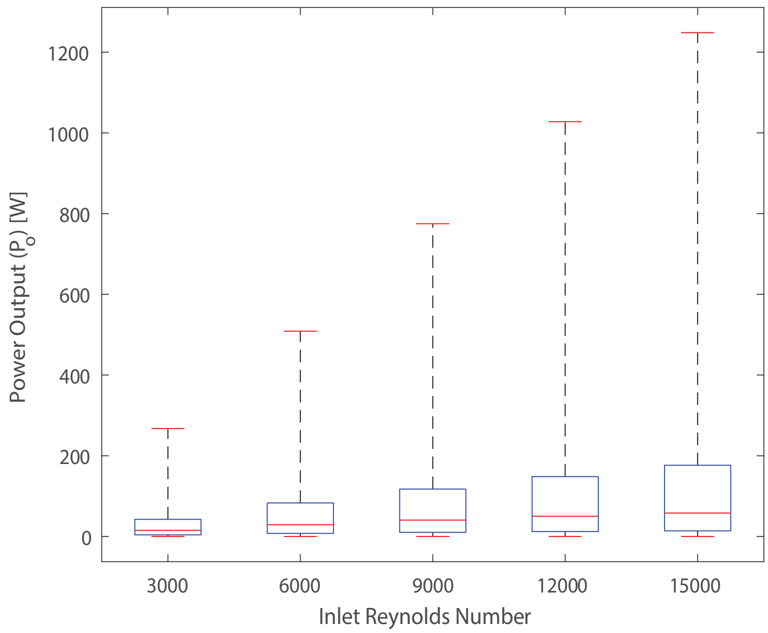

a)

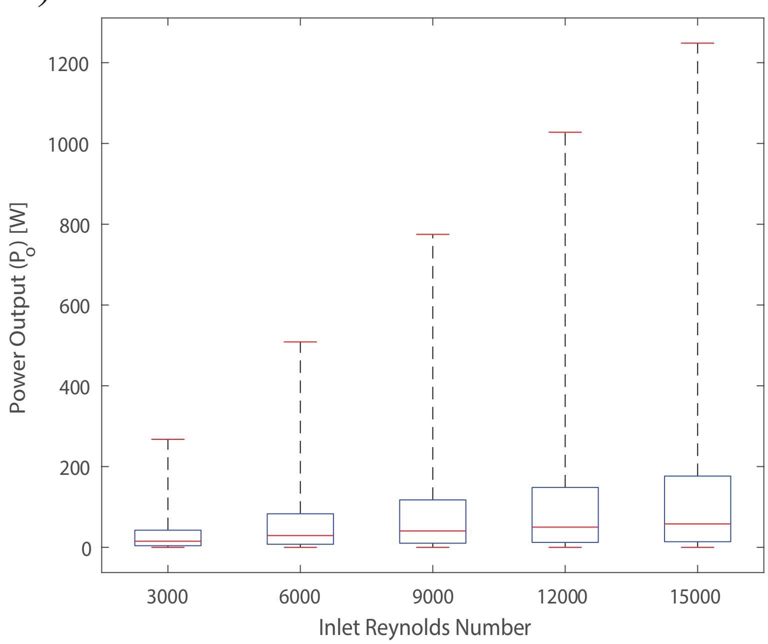

Figure 3.11: Boxplots of power output grouped by a) inlet Reynolds number and b) inlet fluid temperature.

Table 3.3: Statistical values of boxplots for electrical power output, with units of [W], grouped by inlet fluid temperature

Independent Variable: Inlet Fluid Temperature						
T_{in}	Population	Median	75%-Quartile	25%-Quartile	Maximum	Minimum
350 [K]	3,629,781	1.562	3.081	0.734	18.199	0.009
400 [K]	3,744,153	6.821	12.776	3.361	59.960	0.054
450 [K]	3,842,515	16.820	31.569	8.295	136.427	0.139
500 [K]	3,914,574	32.584	61.613	15.905	257.685	0.264
550 [K]	3,964,374	55.103	104.941	26.613	427.657	0.428
600 [K]	3,998,790	85.222	163.495	40.773	648.062	0.628
650 [K]	4,025,879	123.558	238.663	58.534	918.525	0.860
700 [K]	4,046,932	170.840	331.187	80.019	1,248.338	1.120

The change in statistical values exhibit monotonically increasing behavior with each increasing group of inlet Reynolds number and inlet fluid temperature. Given this observation, the behavior of the electrical power output, as a function of the two aforementioned independent variables, is estimated to exhibit behavior similar to that of an exponential function or power function. While polynomials can exhibit monotonically increasing behavior, they also contain inflection points which do not appear evident with maximum, minimum, median or quartile values. The behavior of said function, however, is still considered.

3.2.1.2 Thermal Conversion Efficiency The data distribution of the thermal conversion efficiency is represented by the boxplots shown in figure 3.12a and b. Figure 3.12a is the data distribution for said performance solution grouped by inlet Reynolds numbers while figure 3.12b is the data distribution of the same solution grouped by inlet fluid temperatures. The population size, median, 75%-quartile, 25%-quartile, minimum and maximum values for the boxplots grouped by inlet Reynolds number and inlet fluid temperature are presented in tables 3.4 and 3.5 respectively.

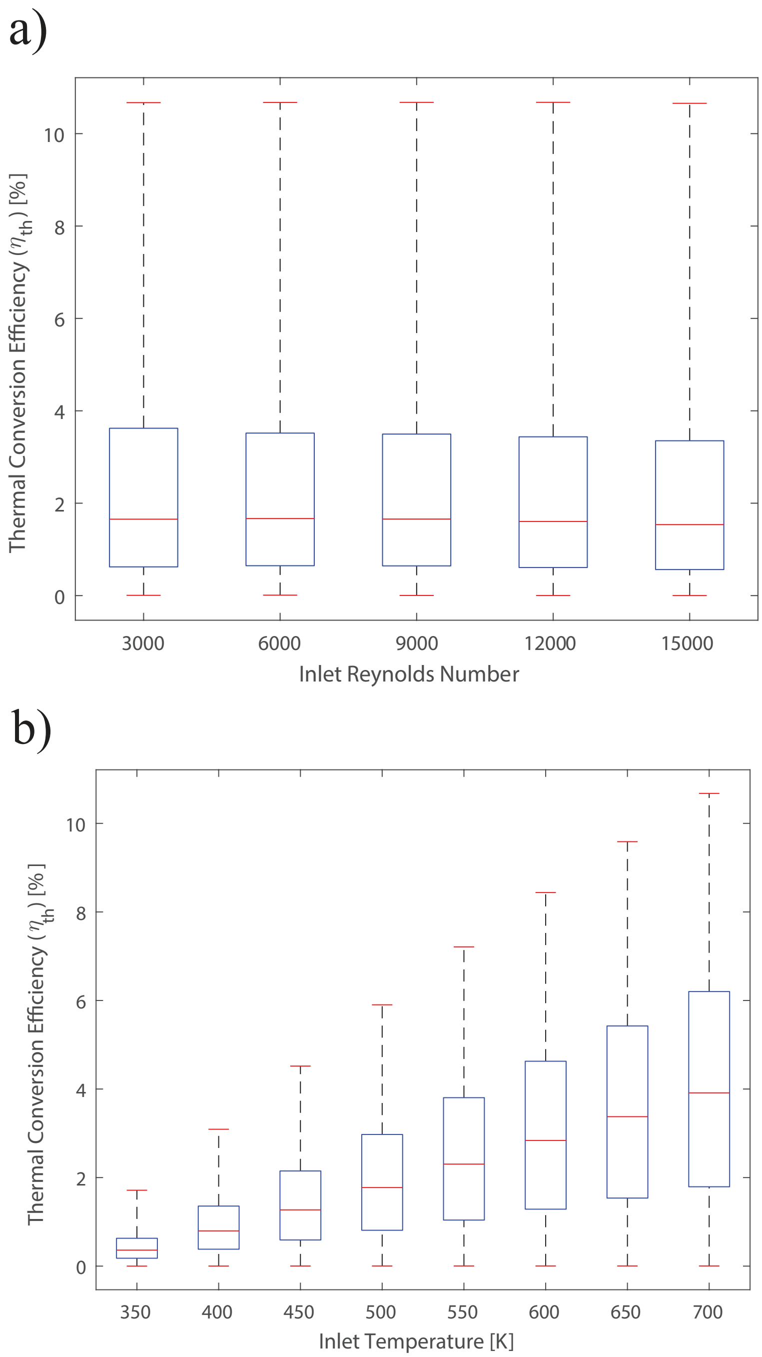

Figure 3.12: Boxplots of thermal conversion efficiency grouped by a) inlet Reynolds number and b) inlet fluid temperature.

Table 3.4: Statistical values of boxplots for thermal conversion efficiency, reported as percent, grouped by inlet Reynolds number

Independent Variable: Inlet Reynolds Number						
Re	Population	Median	75%-Quartile	25%-Quartile	Maximum	Minimum
3,000	5,038,859	1.654	3.622	0.622	10.671	0.005
6,000	6,383,196	1.667	3.518	0.647	10.675	0.010
9,000	6,523,715	1.657	3.496	0.643	10.676	0.003
12,000	6,592,500	1.604	3.437	0.608	10.677	0.001
15,000	6,628,728	1.537	3.352	0.564	10.656	0.001

Table 3.5: Statistical values of boxplots for thermal conversion efficiency, reported as percent, grouped by inlet fluid temperature

Independent Variable: Inlet Fluid Temperature						
T_{in} [K]	Population	Median	75%-Quartile	25%-Quartile	Maximum	Minimum
350	3,629,781	0.361	0.629	0.178	1.714	0.001
400	3,744,153	0.796	1.356	0.382	3.091	0.002
450	3,842,515	1.270	2.150	0.591	4.519	0.003
500	3,914,574	1.774	2.973	0.809	5.902	0.004
550	3,964,374	2.304	3.805	1.040	7.211	0.004
600	3,998,790	2.838	4.628	1.286	8.438	0.004
650	4,025,879	3.376	5.425	1.537	9.587	0.004
700	4,046,932	3.913	6.201	1.793	10.677	0.004

The change in statistical values exhibit negligible change with each increasing group of inlet Reynolds number while exhibiting monotonically increasing behavior between each group of inlet fluid temperature. It is not evident, as of yet, the behavior of the thermal conversion efficiency as a function of the inlet Reynlods number. Based on the SCC provided in figure 3.10, this was to be expected given the linear correlation is close to zero.

The behavior of the thermal conversion efficiency, as a function of inlet fluid temperature, is estimated to exhibit behavior similar to that of an exponential function or power function. While polynomials can exhibit monotonically increasing behavior, they also contain inflection points which do not appear evident with maximum, minimum, median or quartile values. The behavior of said function, however, is still considered.

3.2.1.3 Performance Index The data distribution of the performance index is represented in the boxplots shown in figure 3.13a and b. Figure 3.13a is the data distribution for said performance solution grouped by inlet Reynolds numbers while figure 3.13b is the data distribution of the same solution grouped by inlet fluid temperatures. The population size, median, 75%-quartile, 25%-quartile, minimum and maximum values for the boxplots grouped by inlet Reynolds number and inlet fluid temperature are presented in tables 3.6 and 3.7 respectively.

Table 3.6: Statistical values of boxplots for performance index, a dimensionless quantity, grouped by inlet Reynolds number

Independent Variable: Inlet Reynolds Number						
Re	Population	Median	75%-Quartile	25%-Quartile	Maximum	Minimum
3,000	5,038,859	5.321	36.546	0.003	5,259.13	-0.999
6,000	6,383,196	2.808	30.677	-0.623	5,249.718	-0.999
9,000	6,523,715	0.781	15.127	-0.843	2,353.384	-0.999
12,000	6,592,500	-0.011	8.652	-0.920	1,321.260	-0.999
15,000	6,628,728	-0.382	5.329	-0.954	830.319	-0.999

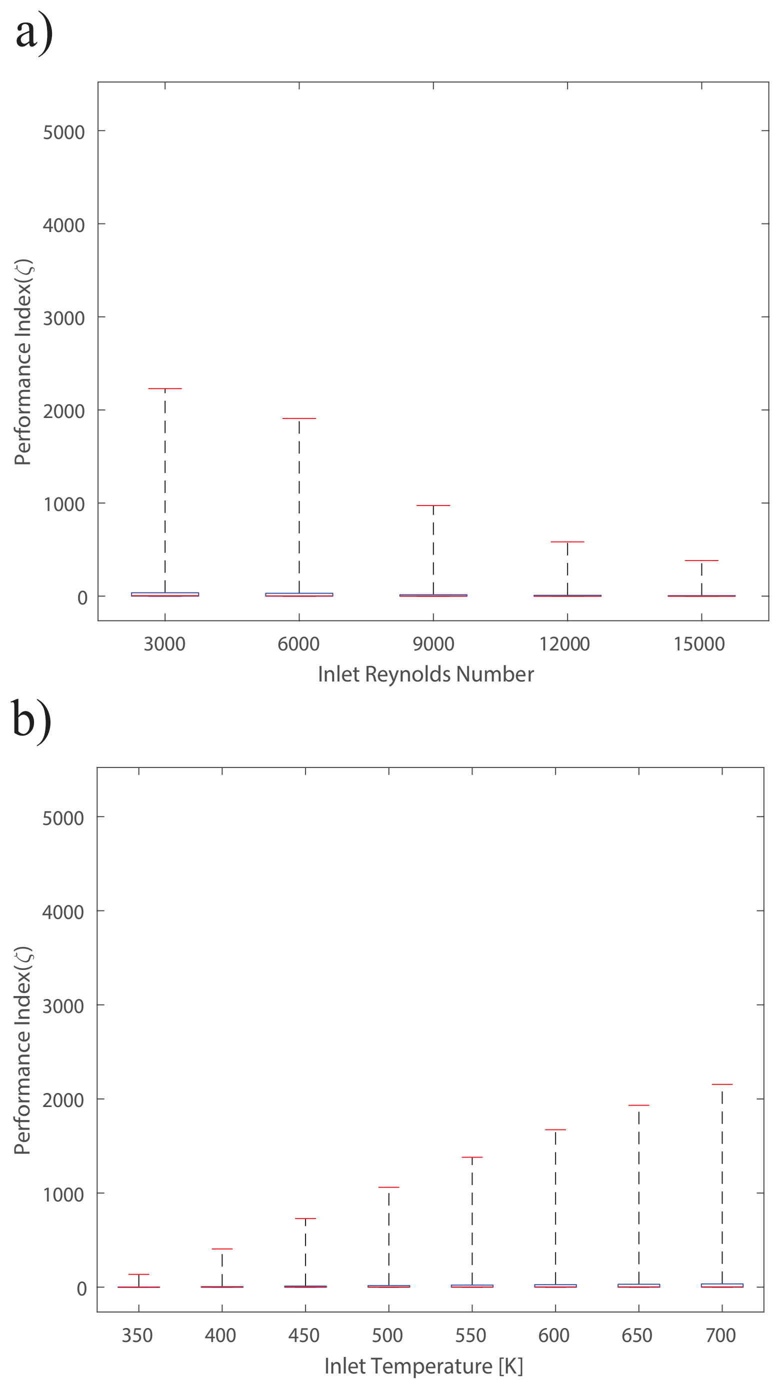

Figure 3.13: Boxplots of performance index grouped by a) inlet Reynolds number and b) inlet fluid temperature.

Table 3.7: Statistical values of boxplots for performance index, a dimensionless quantity, grouped by inlet fluid temperature

Independent Variable: Inlet Fluid Temperature						
T_{in} [K]	Population	Median	75%-Quartile	25%-Quartile	Maximum	Minimum
350	3,629,781	-0.673	1.283	-0.963	888.450	-0.999
400	3,744,153	-0.005	5.777	-0.895	1,793.392	-0.999
450	3,842,515	0.780	11.136	0.591	-0.829	-0.999
500	3,914,574	1.527	16.627	-0.777	3,460.487	-0.999
550	3,964,374	2.183	21.899	-0.740	4,117.660	-0.999
600	3,998,790	2.688	26.722	-0.719	4,635.904	-0.999
650	4,025,879	3.031	30.992	-0.712	5,013.204	-0.999
700	4,046,932	3.254	34.634	-0.713	5,259.130	-0.999

The change in statistical values exhibit monotonically decreasing behavior with increasing inlet Reynolds number while exhibiting monotonically increasing behavior with increasing inlet fluid temperature. The behavior of the performance index, as a function of inlet Reynolds number, is estimated to exhibit behavior similar to that of an inverse exponential function or an inverse power function. While polynomials can exhibit monotonically decreasing behavior, they also contain inflection points which do not appear evident with maximum, minimum, median or quartile values. The behavior of said function, however, is still considered.

The behavior of the performance index, as a function of inlet fluid temperature,is estimated to exhibit behavior similar to that of a linear function, a power function, or a logarithmic curve. The selection of the aforementioned models are predicted due to the ambiguity of the performance index's behavior with respect to the inlet fluid temperature.

3.2.2 Effect of Pin-Fin Heat Exchanger Geometry

According to the SCC's shown in figure 3.10, the pin-fin heat exchanger geometry (i.e maximum pins per row, rows of pins, pin diameter and pin height) has, on average, a moderate linear correlation with the performance solution. In the scope of pin-fin heat exchanger geometry, the electrical power output has a relatively larger linear correlation with the maximum pins per row and the number of pin rows relative to the pin diameter and pin height; therefore, the latter is ignored. The thermal conversion efficiency has a relatively larger linear correlation with pin diameter and pin height compared to the maximum pins per row and the rows of pin; therefore, the latter is ignored. Lastly, the performance index has significant linear correlation will all independent variables that constitute the pin-fin heat exchanger geometry; therefore, the effects of all four variables will be examined. The effects of the pin-fin geometry on the performance solutions are examined in following sub-sections.

3.2.2.1 Electrical Power Output The data distribution of the electrical power output is represented by the boxplots shown in figure 3.17a and b. Figure 3.17a is the data distribution for said performance solution grouped by maximum pins per row while figure 3.17b is the data distribution of the same solution grouped by the number of pin rows. The population size, median, 75%-quartile, 25%-quartile, minimum and maximum values for the boxplots grouped by maximum pins per row and number of pin rows are presented in tables 3.8 and 3.9 respectively.

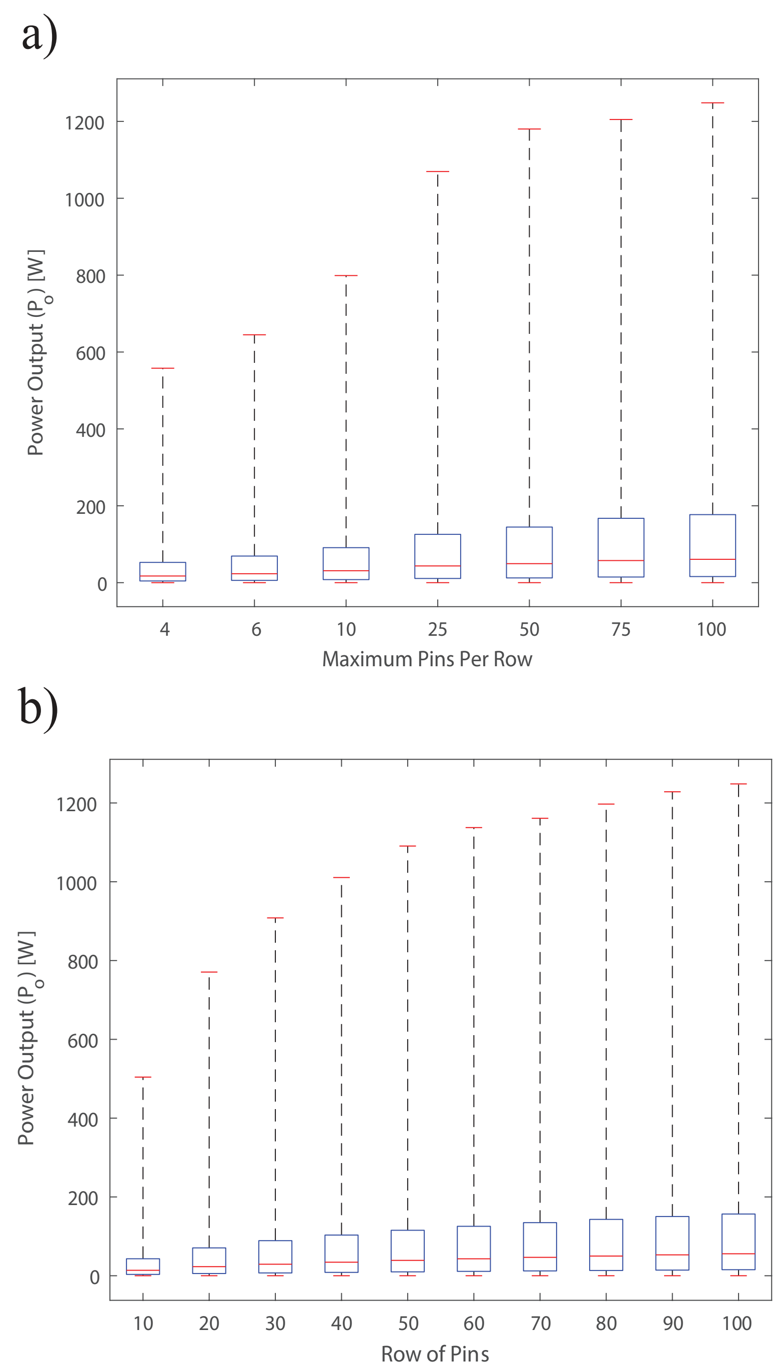

Figure 3.14: Boxplots of electrical power output grouped by a) maximum pins per row count and b) the number of pin rows.

Table 3.8: Statistical values of boxplots for electrical power output, with units of [W], grouped by maximum pins per row

Independent Variable: Maximum Pins Per Row						
M	Population	Median	75%-Quartile	25%-Quartile	Maximum	Minimum
5	4,744,363	17.367	52.754	4.466	557.910	0.009
6	4,768,547	23.244	69.255	5.976	644.883	0.0138
10	4,789,660	31.078	91.069	7.970	798.938	0.020
25	4,746,865	43.538	125.725	10.944	1,069.581	0.025
50	4,558,975	49.473	144.683	12.352	1,180.187	0.025
75	3,922,061	57.544	167.444	14.697	1,204.937	0.013
100	3,636,527	57.544	177.022	15.927	1,248.338	0.0137

Table 3.9: Statistical values of boxplots for electrical power output, with units of [W] grouped by row of pins

Independent Variable: Row of Pins						
N	Population	Median	75%-Quartile	25%-Quartile	Maximum	Minimum
10	3,291,259	13.796	43.106	3.357	504.187	0.009
20	3,288,018	23.066	70.681	5.626	770.828	0.016
30	3,283,336	26.209	89.039	7.125	908.297	0.0156
40	3,244,923	34.333	103.247	8.496	1,010.729	0.014
50	3,183,806	38.958	115.382	9.840	1,090.676	0.025
60	3,113,609	43.007	125.459	11.083	1,137.499	0.033
70	3,041,966	46.660	134.767	12.246	1,161.067	0.031
80	2,972,996	49.963	143.015	13.033	1,197.182	0.043
90	2,905,671	52.999	150.308	14.317	1,228.362	0.044
100	2,841,414	55.761	156.658	15.312	1,248.338	0.042

The change in statistical values exhibit monotonically increasing behavior with each increasing group of maximum pins per row and row of pins. The behavior of the electrical power output, as a function of the aforementioned independent variables is estimated to exhibit behavior similar to that of a logarithmic curve or power function. While polynomials can exhibit monotonically increasing behavior, they also contain inflection points which do not appear evident with maximum, minimum, median or quartile values.

3.2.2.2 Thermal Conversion Efficiency The data distribution of the thermal conversion efficiency is represented by the boxplots shown in figure 3.15a and b. Figure 3.15a is the data distribution for said performance solution grouped by pin diameter while figure 3.15b is the data distribution of the same solution grouped by pin height. The population size, median, 75%-quartile, 25%-quartile, minimum and maximum values for the boxplots grouped by pin diameter and pin height are presented in tables 3.10 and 3.11 respectively.

Table 3.10: Statistical values of boxplots for thermal conversion efficiency, reported as percent, grouped by pin diameter

Independent Variable: Pin Diameter						
D_{pin} [mm]	Population	Median	75%-Quartile	25%-Quartile	Maximum	Minimum
1.587	9,103,694	2.124	4.372	0.725	10.677	0.001
3.175	8,100,500	1.953	3.695	0.867	10.303	0.005
4.763	7,249,652	1.433	3.061	0.582	9.912	0.001
6.350	6,713,152	0.998	2.404	0.383	9.582	0.005

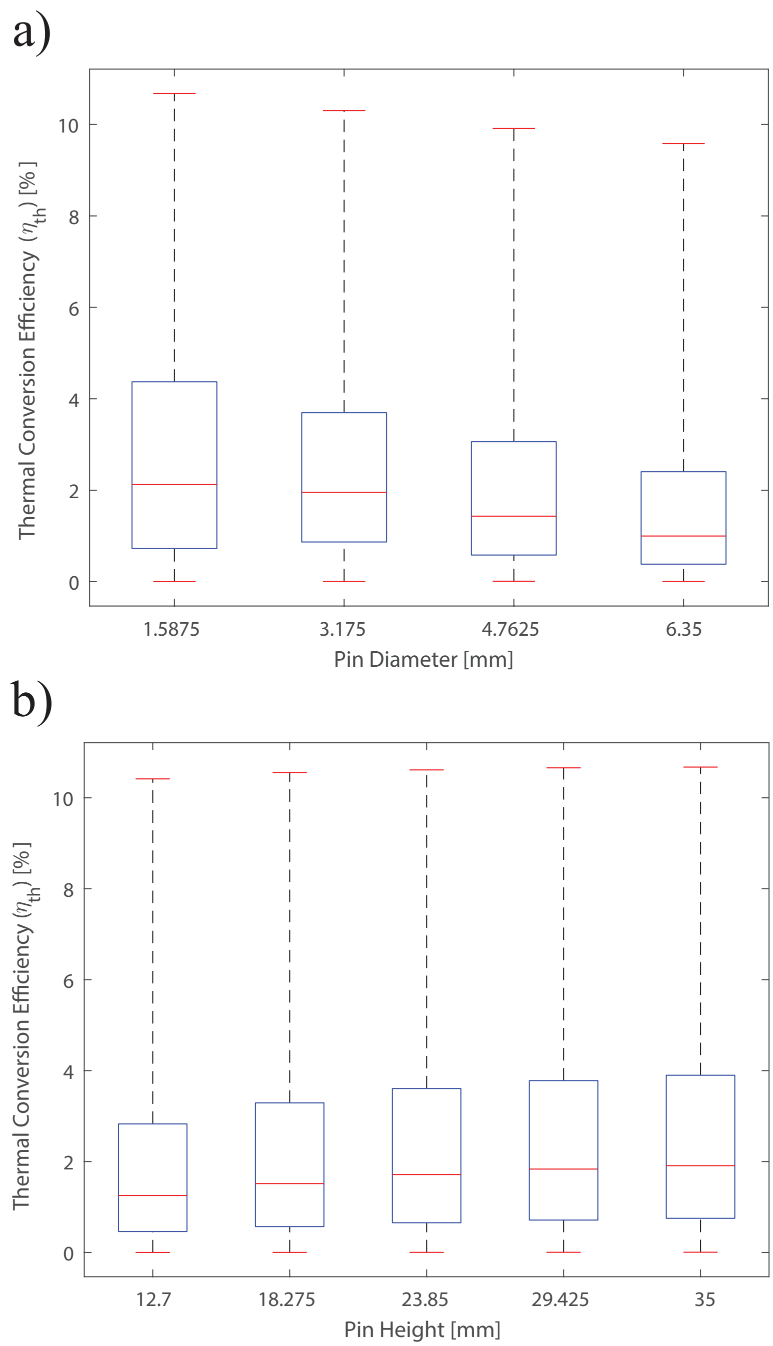

Figure 3.15: Boxplots of thermal conversion efficiency grouped by a) pin diameter and b) pin height.

Table 3.11: Statistical values of boxplots for thermal conversion efficiency, reported as percent, grouped by pin height

Independent Variable: Pin Height						
H_{pin} [mm]	Population	Median	75%-Quartile	25%-Quartile	Maximum	Minimum
12.700	6,523,629	1.254	2.827	0.461	10.417	0.001
18.275	6,317,399	1.515	3.290	0.570	10.556	0.001
23.850	6,131,734	1.715	3.607	0.654	10.614	0.002
29.425	6,106,270	1.834	3.780	0.712	10.659	0.004
35.000	6,087,966	1.910	3.898	0.751	10.677	0.005

The change in statistical values exhibit monotonically decreasing behavior between each increasing group of the pin diameter while exhibiting monotonically increasing behavior between each increasing group of pin height, but at a smaller rate. The behavior of the thermal conversion efficiency, as a function of pin diameter, is estimated to exhibit behavior similar to that of a negative linear function with a significant offset or an inverse power function.

The behavior of the thermal conversion efficiency, as a function of pin height, is similar to that of a polynomial. While faint, the inflection point appears to occur at a pin height value of 23.85 [mm]. Afterwards, a subtle, yet existing decrease in value appears to occur. The behavior also appears to be similar to a logarithmic curve with a significant offset. The growth of the efficiency at low values for the pin height seem apparent and gradually dissipates with an increasing pin height.

3.2.2.3 Performance Index The data distribution of the performance index is represented by the boxplots grouped by maximum pins per row, number of row of pins, pin diameter and pin height shown in figure 3.16a and b, and figure 3.17a and b, respectively. The population size, median, 75%-quartile, 25%-quartile, minimum and maximum values for the boxplots grouped by maximum pins per row, number of row of pins, pin diameter and pin height are presented in tables 3.12 - 3.15 respectively.

Table 3.12: Statistical values of boxplots for performance index, a dimensionless quantity, grouped by maximum pins per row

Independent Variable: Maximum Pins Per Row						
M	Population	Median	75%-Quartile	25%-Quartile	Maximum	Minimum
4	4,744,363	-0.945	-0.737	-0.991	22.797	-1.000
6	4,768,547	-0.855	-0.353	-0.974	54.931	-1.000
10	4,789,660	-0.533	0.950	-0.909	180.451	-1.000
25	4,746,865	2.274	11.330	-0.254	1,333.622	-1.000
50	4,558,975	11.475	42.961	2.215	5,259.130	-0.993
75	3,922,061	19.723	62.378	5.107	2,990.822	-0.978
100	3,636,527	31.100	94.009	9.171	5,249.718	-0.957

Table 3.13: Statistical values of boxplots for performance index, a dimensionless quantity, grouped by row of pins

Independent Variable: Row of Pins						
N	Population	Median	75%-Quartile	25%-Quartile	Maximum	Minimum
10	3,291,259	2.668	34.967	-0.769	5,259.130	-1.000
20	3,288,018	2.376	29.296	-0.772	4,473.216	-1.000
30	3,283,336	1.995	24.003	-0.782	3,721.493	-1.000
40	3,244,923	1.551	19.272	-0.799	3,099.910	-1.000
50	3,183,806	1.143	15.603	-0.818	2,589.012	-1.000
60	3,113,609	0.812	12.851	-0.836	2,188.141	-1.000
70	3,041,966	0.550	10.856	-0.853	1,871.123	-1.000
80	2,972,996	0.338	9.285	-0.867	1,632.741	-1.000
90	2,905,671	0.166	7.989	-0.880	1,436.882	-1.000
100	2,841,414	0.028	6.890	-0.891	1,277.620	-1.000

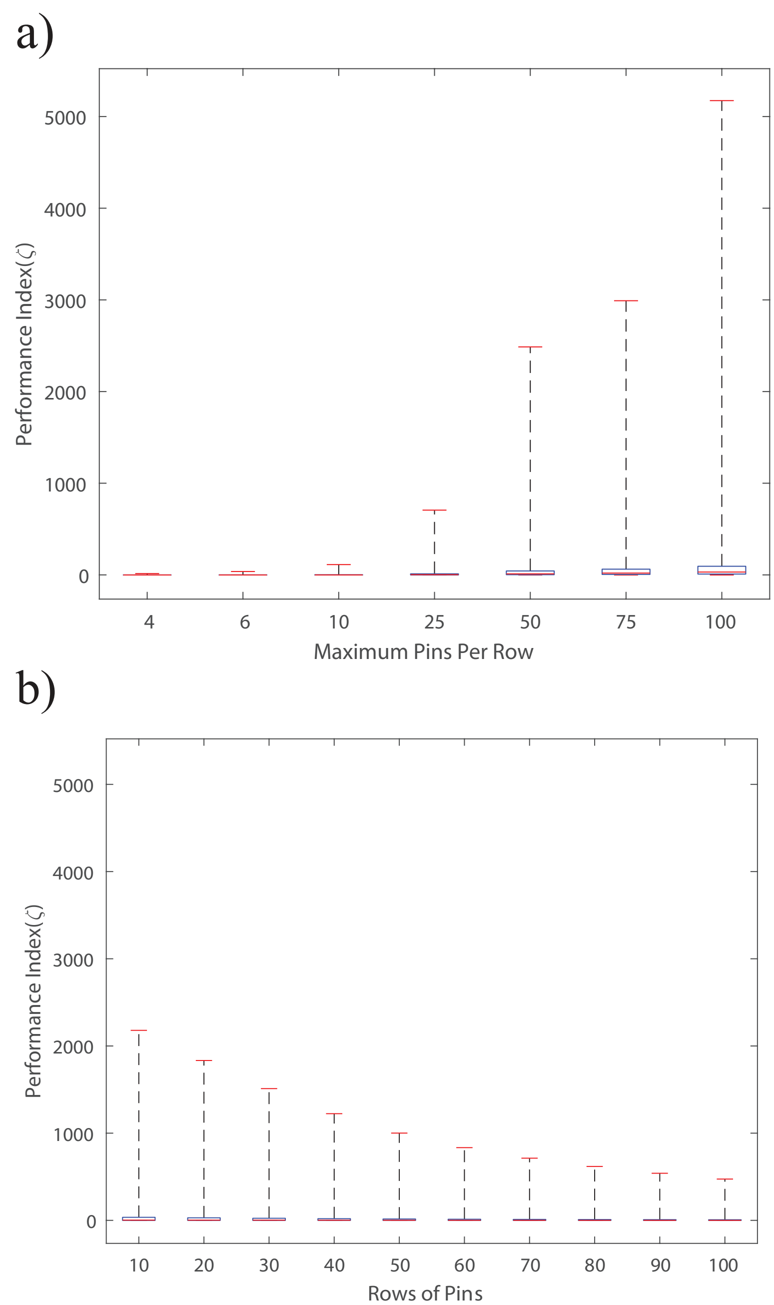

Figure 3.16: Boxplots of performance index grouped by a) maximum pins per row count and b) the number of pin rows.

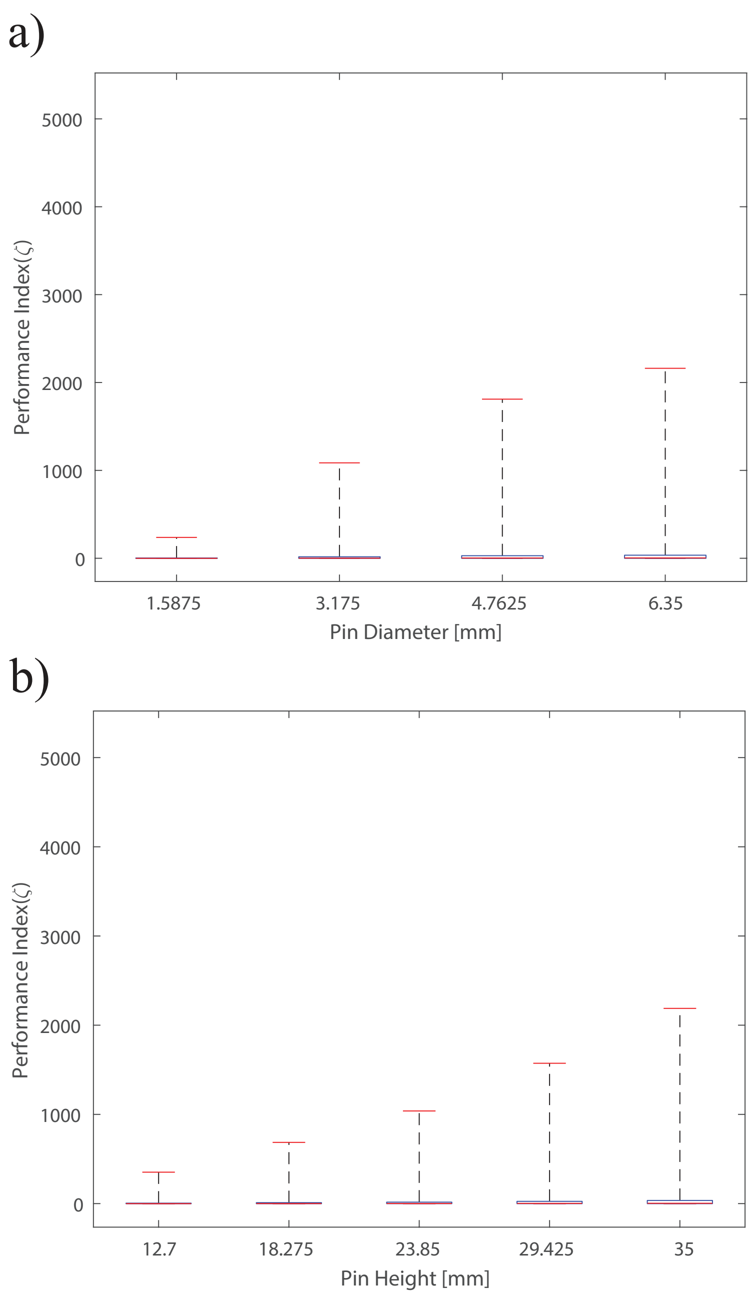

Figure 3.17: Boxplots of performance index grouped by a) pin diameter and b) pin height.

Table 3.14: Statistical values of boxplots for performance index, a dimensionless quantity, grouped by pin diameter

Independent Variable: Pin Diameter						
D_{pin} [mm]	Population	Median	75%-Quartile	25%-Quartile	Maximum	Minimum
1.587	9103694	-0.607	3.241	-0.982	237.417	-1.000
3.175	8100500	1.141	16.977	-0.839	1,173.676	-0.1.000
4.763	7249652	3.127	29.123	-0.571	2,951.266	-1.000
6.350	6713152	4.085	35.089	-0.353	5,259.130	-1.000

Table 3.15: Statistical values of boxplots for performance index, a dimensionless quantity, grouped by pin height

Independent Variable: Pin Height						
H_{pin} [mm]	Population	Median	75%-Quartile	25%-Quartile	Maximum	Minimum
12.700	6,523,629	-0.287	4.849	-0.941	1,948.815	-1.000
18.275	6,317,399	0.414	10.387	-0.877	2,793.432	-1.000
23.850	6,131,734	1.194	16.238	-0.804	2,403.697	-1.000
29.425	6,106,270	2.320	25.096	-0.705	3,709.050	-1.000
35.000	6,087,966	3.626	35.295	-0.591	5,259.130	-1.000

The change in statistical values exhibit monotonically decreasing behavior with each increasing group of row count. However, they exhibit monotonically increasing behavior with with each increasing group of maximum pins per row, pin diameter and pin height. The performance index, as a function of maximum pins per row or pin height, is estimated to exhibit behavior similar to that of an exponential function or a power function. While polynomials can exhibit monotonically increasing behavior, they also contain inflection points which do not appear evident with maximum, minimum, median or quartile values. The behavior of said function, however, is still considered.

The behavior of the performance index, as a function of the number of pin rows, is estimated to exhibit behavior similar to that of an inverse exponential curve or an inverse power function. While the outliers appear to represent this behavior, the median and quartiles are to small to backup this estimation. As a result, all possible fits will be considered.

As a function of the number of pin rows, the performance index is estimated to exhibit behavior similar to that of a logarithmic curve. Once again, the outliers appear to represent this behavior since the median and quartile values are significantly smaller. Likewise, all possible fits will be considered.

3.2.3 Effect of Thermoelectric Material Length

According to the SCC's shown in figure 3.10, the thermoelectric material length has a negligible linear correlations with the electrical power output and performance index. Therefore, the effects of the thermometric material length will be ignored. The only exception is the correlation between the thermoelectric materials length and the thermal conversion efficiency. This relationship will be examined.

3.2.3.1 Thermal Conversion Efficiency The data distribution of the thermal conversion efficiency is represented by the boxplot, grouped by thermoelectric material length, shown in figure 3.18. The population size, median, 75%-quartile, 25%-quartile, minimum and maximum values are presented in table 3.16.

The change in statistical values exhibit monotonically increasing behavior between each increasing group of the thermoelectric material length. The thermal conversion efficiency, as a function of thermoelectric material length, is estimated to exhibit behavior similar to that of a logarithmic curve or a power function. While polynomials can exhibit monotonically increasing behavior, they also contain inflection points which do not appear evident with maximum, minimum, median or quartile values.

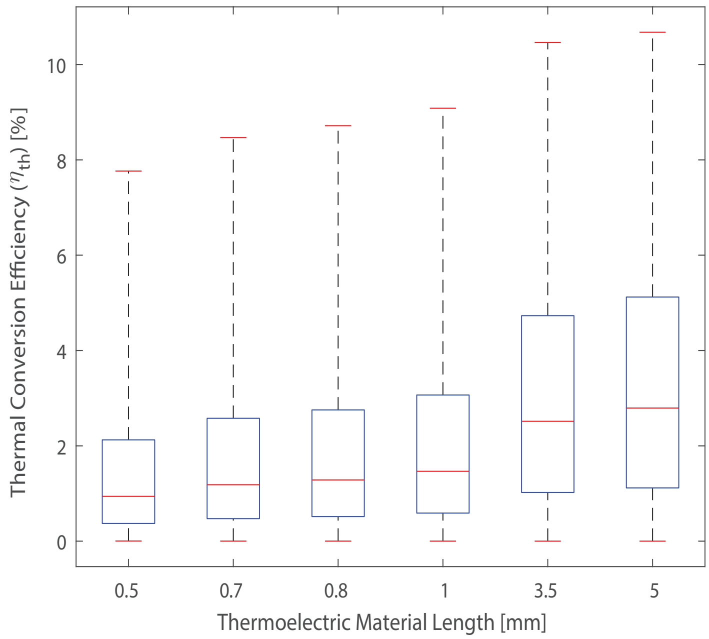

Figure 3.18: Boxplot of thermal conversion efficiency grouped by thermoelectric material length

Table 3.16: Statistical values of boxplots for thermal conversion efficiency, reported as percent, grouped by thermoelectric material length

Independent Variable: Thermoelectric Material Length						
$t_{N,P}$ [mm]	Population	Median	75%-Quartile	25%-Quartile	Maximum	Minimum
0.5	4,634,061	0.940	2.126	0.372	7.765	0.004
0.7	4,862,177	1.184	2.578	0.473	8.468	0.002
0.8	4,950,073	1.285	2.754	0.517	8.717	0.002
1.0	5,065,681	1.466	3.067	0.589	9.083	0.001
3.5	5,759,771	2.515	4.732	1.021	10.463	0.001
5.0	5,895,235	2.793	5.122	1.118	10.677	0.001

3.2.4 Effect of Cold-Side Thermal Impedance

According to the SCC's shown in figure 3.10, the cold-side thermal impedance (i.e cold-side heat exchanger area, cold-side convection coefficient and heat sink temperature) has, on average, a very low linear correlation with the performance solutions. Given this observation, model fits for the performance solutions as a function of cold-side heat exchanger area, cold-side convection coefficient and heat sink temperature will not be considered.

3.2.5 Variable Selection

The influence of significant independent variables on the performance solutions have been discussed in Sections 3.2.1 - 3.2.4. In order for a set of design equations to be developed, the performance solutions must be defined in terms of their independent variables via multivariate regression. The three highest independent variables with the greatest linear correlation are selected for this task. While the addition of more independent variables better reflects the behavior of the solution, the deviation of the model fit with actual data points is predicted to be too large for acceptable results.

Based on the SCC's of the correlation matrix, the performance solutions will be represented by functions put in terms of their respective independent variables with the greatest influence. The generic functions are given as follows:

$$P_o = f(T_{\infty,h}, \mathrm{Re}, M_{max}), \tag{3.2}$$

$$\eta_{th} = f(T_{\infty,h}, t_{N,P}, D_{pin}), \tag{3.3}$$

$$\zeta = f(M_{max}, D_{pin}, \mathrm{Re}). \tag{3.4}$$

A set of equations for design optimization is based on the configurations that yield the maximum values of each performance solution. In Section 3.2, the formulation of said equations is discussed.

3.3 Maximum Configuration For Optimization

The maximum values for each performance solutions with their corresponding configuration are listed in table 3.17.

Table 3.17: Configurations of maximum performance solutions

Maximum Performance Solutions			
Variable	$P_{o,max}$	$\eta_{th,max}$	ζ_{max}
Re	15,000	12,000	3,000
$T_{\infty,h}$	700 [K]	700 [K]	700 [K]
M_{max}	100	100	50
N	100	10	10
D_{pin}	3.175 [mm]	1.5875 [mm]	6.35 [mm]
H_{pin}	35 [mm]	35 [mm]	35 [mm]
$t_{N,P}$	3.5 [mm]	5 [mm]	5 [mm]
$A_{hex,c}$	$1{\cdot}10^{-1}$ [m^2]	$1{\cdot}10^{-1}$ [m^2]	$1{\cdot}10^{-1}$ [m^2]
h_c	1,000 [Wm^{-2}K^{-1}]	1,000 [Wm^{-2}K^{-1}]	1,000 [Wm^{-2}K^{-1}]
$T_{\infty,c}$	273.15 [K]	273.15 [K]	273.15 [K]
Solution	**1,248.338 [W]**	**10.677 %**	**5,259.130**

Design optimization of the iTED is centered around obtaining the maximum possible values of the performance solutions; however, this requires all performance solutions to be solved in terms of the same independent variables while also being solved in the same domain of variables held constant. It is evident that the numeric values of the independent variables corresponding to the maximum value of one performance solution are different from the numeric values of the independent variables corresponding to the maximum value of another performance solution. Concurrently, the generic functions provided in Section 3.2.5 defines the performance solutions in terms of different independent variables; thus, the local maximum or minimum values of dependent solutions can not be solved in terms the same independent variables. Given these observations, three sets of equations must be formulated to satisfy the need of design optimization.

The equations of each set must define the performance solutions as non-linear functions in terms of the same three variables while holding the remaining seven variables constant. This results in each set being defined by the remaining independent variables that are held constant. The numeric value for these seven variables will be based on the configuration of the maximum value of the performance solution. As a result, the set of equations can be defined as follows:

$$\mathbb{Z}_1 \equiv \begin{cases} P_o = f_1(T_{\infty,h}, \mathrm{Re}, M_{max}) \in \mathbb{A}_1 & (3.5a) \\ \eta_{th} = f_2(T_{\infty,h}, \mathrm{Re}, M_{max}) \in \mathbb{A}_1 & (3.5b) \\ \zeta = f_3(T_{\infty,h}, \mathrm{Re}, M_{max}) \in \mathbb{A}_1 & (3.5c) \end{cases}$$

$$\mathbb{Z}_2 \equiv \begin{cases} P_o = f_4(T_{\infty,h}, t_{N,P}, D_{pin}) \in \mathbb{A}_2 & (3.6a) \\ \eta_{th} = f_5(T_{\infty,h}, t_{N,P}, D_{pin}) \in \mathbb{A}_2 & (3.6b) \\ \zeta = f_6(T_{\infty,h}, t_{N,P}, D_{pin}) \in \mathbb{A}_2 & (3.6c) \end{cases}$$

$$\mathbb{Z}_3 \equiv \begin{cases} P_o = f_7(M_{max}, D_{pin}, \mathrm{Re}) \in \mathbb{A}_3 & (3.7a) \\ \eta_{th} = f_8(M_{max}, D_{pin}, \mathrm{Re}) \in \mathbb{A}_3 & (3.7b) \\ \zeta = f_9(M_{max}, D_{pin}, \mathrm{Re}) \in \mathbb{A}_3 & (3.7c) \end{cases}$$

where $\mathbb{Z}_1$, $\mathbb{Z}_2$ and $\mathbb{Z}_3$ are the set denotations based on maximum electrical power output, thermal conversion efficiency and performance index, respectively. Functions $f_1 - f_9$ are non-linear functions yet to be determined, and sets $\mathbb{A}_1$, $\mathbb{A}_2$ and $\mathbb{A}_3$ are finite sets containing numeric values of independent variables based on the configurations of the maximum power output, thermal conversion efficiency and performance index, respectively. Here, $\mathbb{A}_1$, $\mathbb{A}_2$ and $\mathbb{A}_3$ are defined as:

$$\begin{aligned} \mathbb{A}_1 \equiv \{Re = 15,000\, T_{\infty,h} = 700 \text{ [K]}\, M_{max} = 100\, N = 100,\ D_{pin} = 3.175 \text{ [mm]}, \\ H_{pin} = 35 \text{ [mm]},\ t_{N,P} = 3.5 \text{ [mm]},\ A_{hex,c} = 1 \cdot 10^{-1} [\text{m}^2], \\ h_c = 1,000 \text{ [Wm}^{-2}\text{K}^{-1}],\ T_{\infty,c} = 273.15 \text{ [K]}\} \end{aligned} \tag{3.8}$$

$$\mathbb{A}_2 \equiv \{Re = 12,000\, T_{\infty,h} = 700 \text{ [K]}\, M_{max} = 100\, N = 10,\ D_{pin} = 1.5875 \text{ [mm]},$$
$$H_{pin} = 35 \text{ [mm]},\ t_{N,P} = 5 \text{ [mm]},\ A_{hex,c} = 1 \cdot 10^{-1} [\text{m}^2],$$
$$h_c = 1,000 \text{ [Wm}^{-2}\text{K}^{-1}],\ T_{\infty,c} = 273.15 \text{ [K]}\} \qquad (3.9)$$

$$\mathbb{A}_3 \equiv \{Re = 3,000\, T_{\infty,h} = 700 \text{ [K]}\, M_{max} = 50\, N = 10,\ D_{pin} = 6.35 \text{ [mm]},$$
$$H_{pin} = 35 \text{ [mm]},\ t_{N,P} = 5 \text{ [mm]},\ A_{hex,c} = 1 \cdot 10^{-1} [\text{m}^2],$$
$$h_c = 1,000 \text{ [Wm}^{-2}\text{K}^{-1}],\ T_{\infty,c} = 273.15 \text{ [K]}\} \qquad (3.10)$$

The non-linear function $f_1 - f_9$ are yet to be determined. Prelude to this, a uni-variate non-linear regression is performed to determine model fits for each function in Section 3.4.

3.4 Uni-Variate Nonlinear Regression

Initial estimates for coefficients and model fits are necessary for non-linear multivariate models of each solution. Concurrently, it is useful to understand the behavior of the solutions so as to modify initial estimations obtained. Uni-variate non-linear regression is an acceptable form of regression analysis to obtain initial estimations. In the section, the regression analysis uses the method of least squares with a convergence criterion of 1^{-9}. Additionally, the performance solutions are plotted over a finer domain of their respective independent variables. The results of the regression analysis as well as the plots are presented in sub-sections 3.4.1 - 3.4.3.

3.4.1 Equation Set $\mathbb{Z}_1$

The equations of set $\mathbb{Z}_1$ define independent variables with numeric values that ensure the iTED is rated to produce the maximum possible electrical power output based on the data of the parametric study. Each performance solution of this set exists in the domain $\mathbb{A}_1$, where the independent variables are defined in table 3.17. Inlet fluid temperature, inlet

Reynolds number and the maximum pins per row are varied when they are the independent variable being plotted over. In the following subsections, each performance solution will be plotted over a finer domain of the aforementioned variables.

3.4.1.1 Electrical Power Output Based on R^2 values, the best fit for the power output as a function of inlet fluid temperature is the second order polynomial function. The model was chosen due to its R^2 value being the highest and its root mean squared error (RMSE) being the lowest among other models. Figure 3.19 shows the power output plotted over a finer interval of inlet fluid temperature. Included are the predicted values of the model fit and the 95% confidence intervals, of which has an average half-width of 3.421 [W]. The results of other less useful model fits are listed in table 3.18.

Based on R^2 values, the best fit for the power output as a function of inlet Reynolds number is the root function. The model was chosen due to its R^2 value being one of the highest and its RMSE being one of the lowest among other models. While the second order polynomial has a higher R^2 value and a lower RMSE, it is predicted its inflection point will deviate the model from the power output at larger Reynolds numbers compared to the root function. Figure 3.20 shows the power output plotted over a finer interval of inlet Reynolds number. Included are the predicted values of the model fit and the 95% confidence intervals, of which has an average half-width of 2.849 [W]. The results of other less useful model fits are listed in table 3.18.

Based on R^2 values, the best fit for the power output as a function of maximum pins per row is the power function. The model was chosen due to its R^2 value being one of the highest and its RMSE being one of the lowest among other models. While the second order polynomial has a higher R^2 value and a lower RMSE, it is predicted its inflection point will deviate the model from the power output at a larger count of maximum pins per row compared to the power function. Figure 3.21 shows the power output plotted over a finer interval of maximum pins per row. Included are the predicted values of the model fit and the 95% confidence intervals, of which has an average half-width of 11.587 [W]. The results of other less useful model fits are listed in table 3.18.

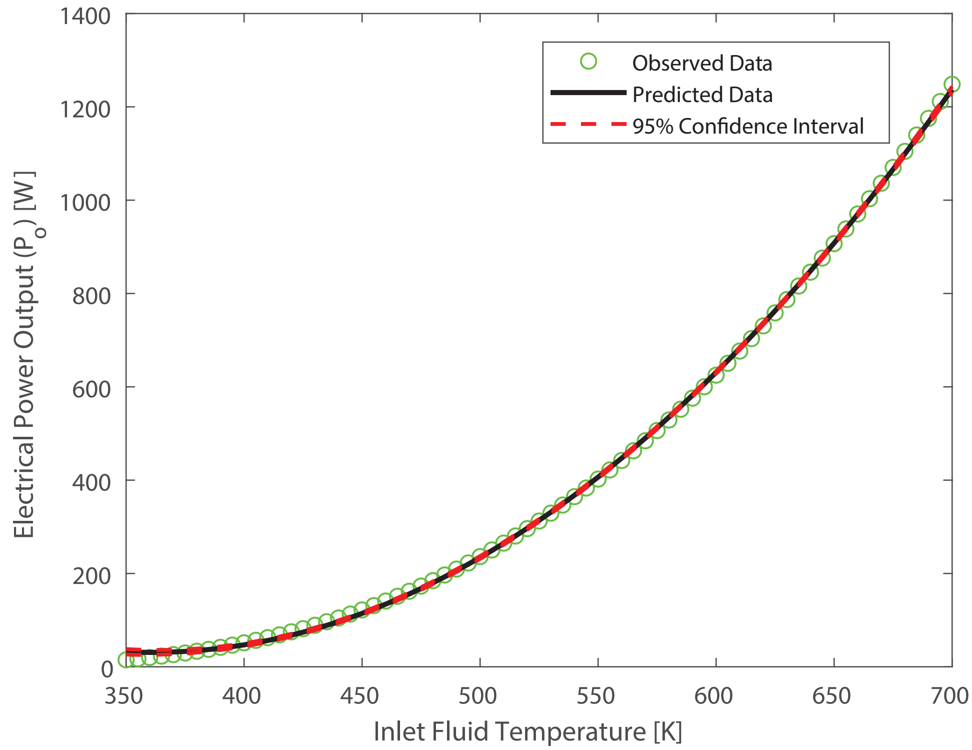

Figure 3.19: Electrical power output versus inlet fluid temperature

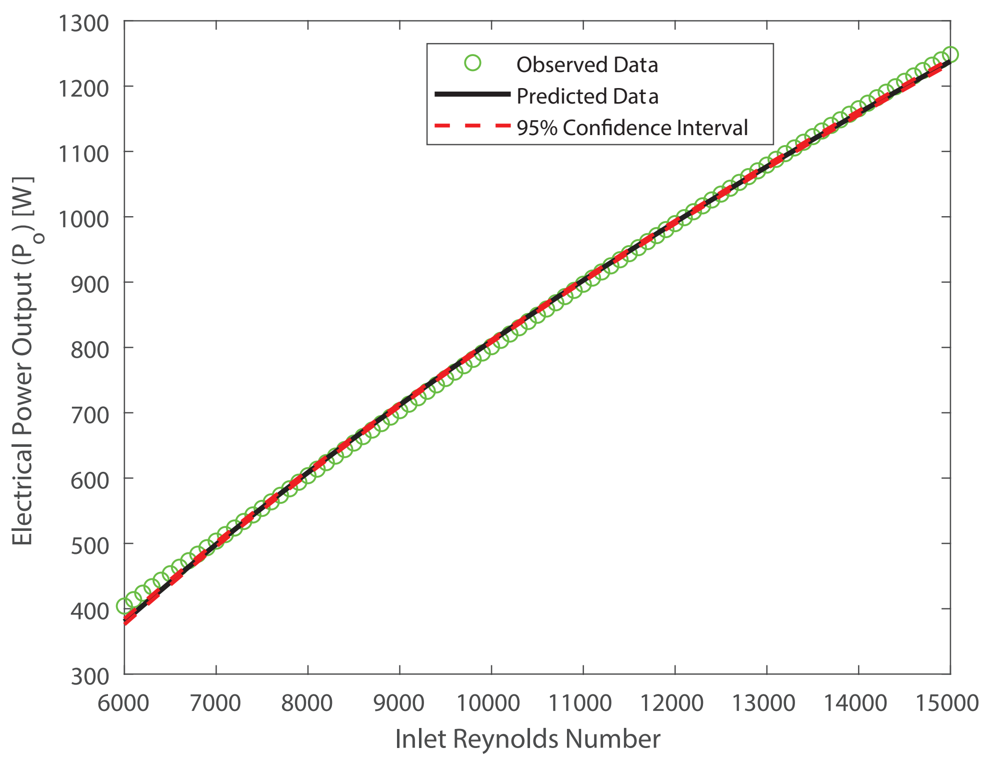

Figure 3.20: Electrical power output versus inlet Reynolds number

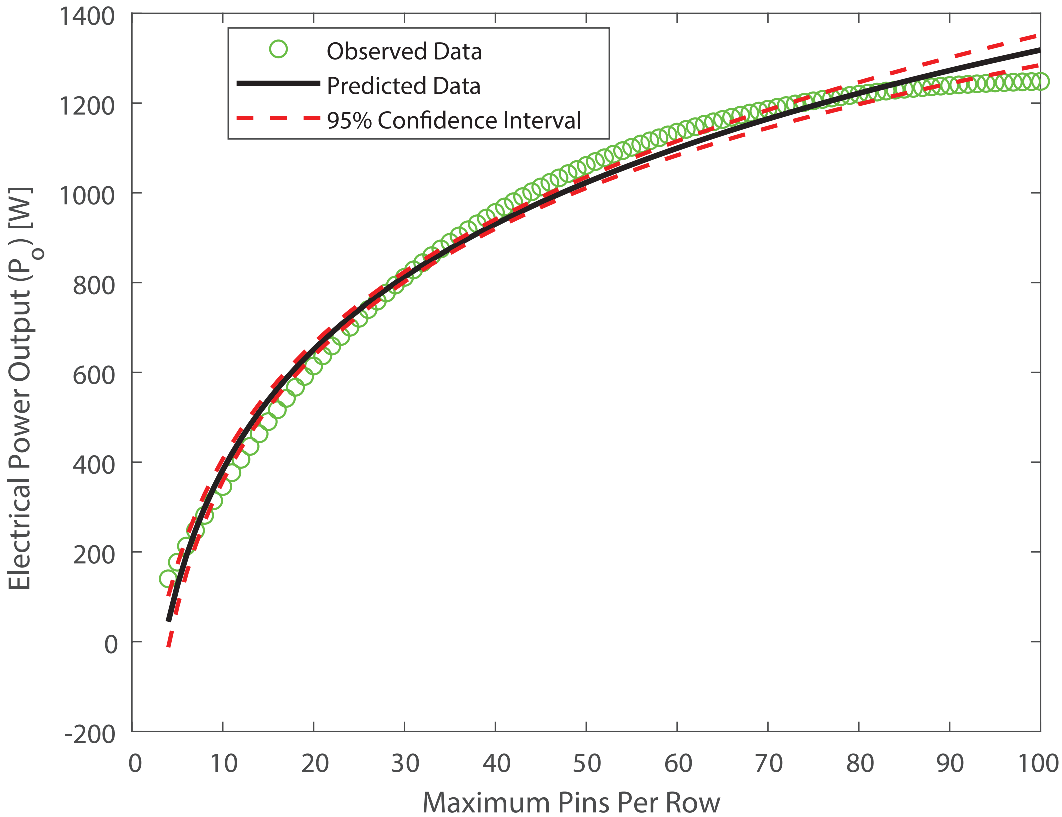

Figure 3.21: Electrical power output versus maximum pins per row

Table 3.18: Uni-variate non-linear regression results for electrical power output versus independent variables in domain $\mathbb{A}_1$

Electrical Power Output Model Fits				
Independent variable	Model Fits	R^2	RMSE	Observations
$T_{\infty,h}$	$K_1 + K_2 X^{K_3}$	NaN	∞	-
	$K_1 + K_2\sqrt{X}$	0.903	116	71
	$K_1 + K_2 X + K_3 X^2$	1	6	71
	$K_1 + K_2 \frac{\log(X)}{\log(K_3)}$	NaN	∞	-
	$K_1 + K_2^{XK_3}$	NaN	∞	-
Re	$K_1 + K_2 X^{K_3}$	NaN	∞	-
	$K_1 + K_2\sqrt{X}$	0.999	7.92	91
	$K_1 + K_2 X + K_3 X^2$	1	1.33	91
	$K_1 + K_2 \frac{\log(X)}{\log(K_3)}$	NaN	∞	-
	$K_1 + K_2^{XK_3}$	0	250	91
M_{max}	$K_1 + K_2 X^{K_3}$	0.988	34.4	97
	$K_1 + K_2\sqrt{X}$	0.949	70.7	97
	$K_1 + K_2 X + K_3 X^2$	0.993	26	97
	$K_1 + K_2 \frac{\log(X)}{\log(K_3)}$	NaN	∞	-
	$K_1 + K_2^{XK_3}$	0	310	97

Table 3.19: Selected uni-variate non-linear fits for electrical power output in domain $\mathbb{A}_1$

Summary of Results			
Independent Variable	Model Fit	R^2	RMSE
$T_{\infty,h}$	$1,394.2 - 7.56X + 0.0105X^2$	1	6
Re	$-1,095.6 + 19.054\sqrt{X}$	0.999	7.92
M_{max}	$-5,964.7 + 5,531.6X^{0.05973}$	0.988	34.4

3.4.1.2 Thermal Conversion Efficiency Based on R^2 values, the best fit for the thermal conversion efficiency as a function of inlet fluid temperature is the power function. The model was chosen due to its R^2 value being one of the highest and its RMSE being one of the lowest among other models. While the second order polynomial has a higher R^2 value and a lower RMSE, it is predicted its inflection point will deviate the model from the thermal conversion efficiency at larger inlet fluid temperatures compared to the power function. Figure 3.22 shows the thermal conversion efficiency plotted over a finer interval of inlet fluid temperature. Included are the predicted values of the model fit and the 95% confidence intervals, of which has an average half-width of 0.289 percentage points. The results of other less useful model fits are listed in table 3.20.

Based on R^2 values, the best fit for the thermal conversion efficiency as a function of inlet Reynolds number is the power function. The model was chosen due to its R^2 value being the highest and its RMSE being the lowest among other models. Figure 3.23 shows the thermal conversion efficiency plotted over a finer interval of inlet Reynolds number. Included are the predicted values of the model fit and the 95% confidence intervals, of which has an average half-width of 0.010 percentage points. The results of other less useful model fits are listed in table 3.20.

Based on R^2 values, the best fit for the thermal conversion efficiency as a function of maximum pins per row is the second order polynomial function. The model was chosen due to its R^2 value being the highest and its RMSE being the lowest among other models. Figure 3.24 shows the thermal conversion efficiency plotted over a finer interval of maximum pins per row. Included is the predicted values of the model fits and the 95% confidence intervals with an average confidence interval half-width of 0.477 percentage points. The results of other less useful model fits are listed in table 3.20.

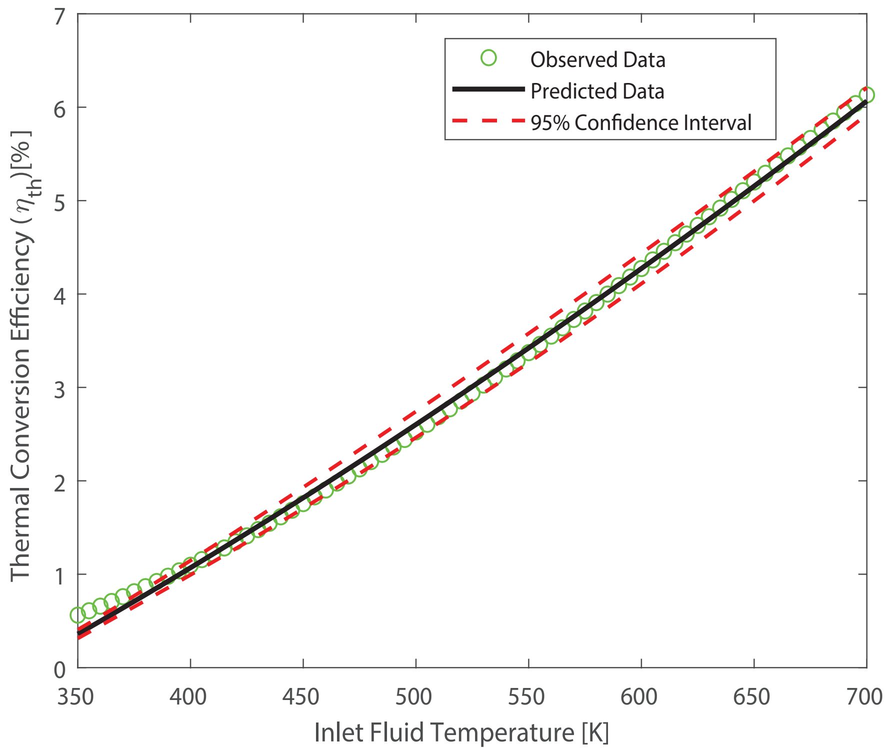

Figure 3.22: Thermal conversion efficiency versus inlet fluid temperature

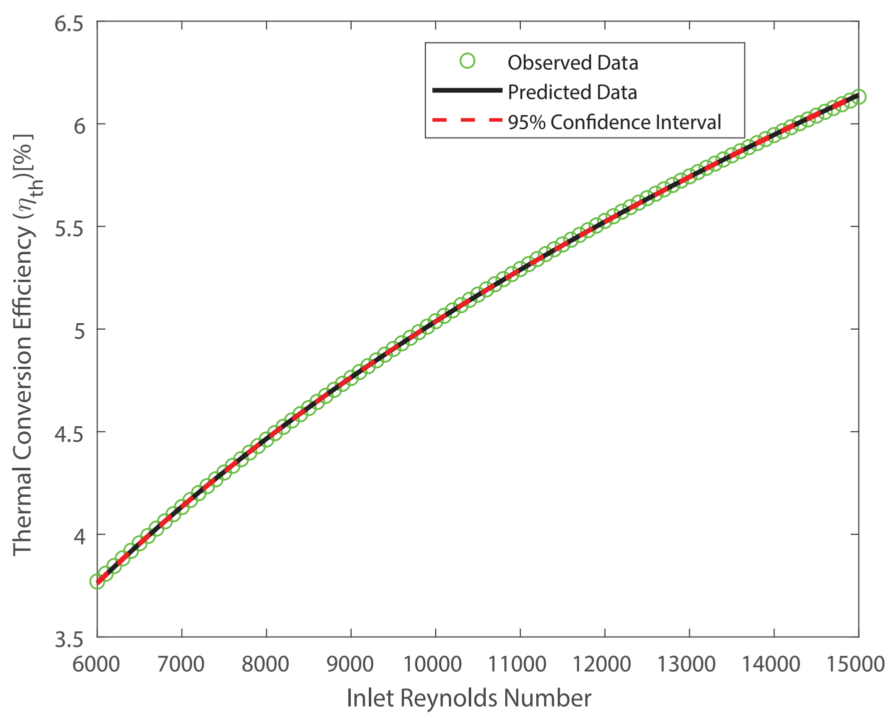

Figure 3.23: Thermal conversion efficiency versus inlet Reynolds number

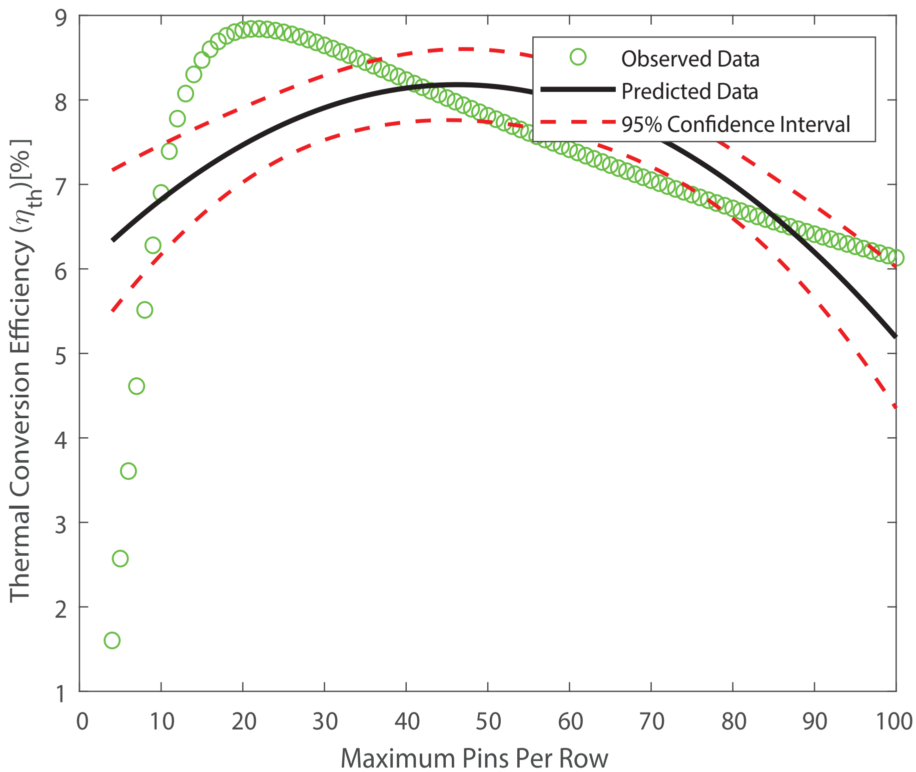

Figure 3.24: Thermal conversion efficiency versus maximum pins per row

Table 3.20: Uni-variate non-linear regression results for thermal conversion efficiency versus independent variables in domain $\mathbb{A}_1$

Thermal Conversion Efficiency Model Fits				
Independent variable	Model Fits	R^2	RMSE	Observations
$T_{\infty,h}$	$K_1 + K_2\mathrm{X}^{K_3}$	0.996	0.113	71
	$K_1 + K_2\sqrt{\mathrm{X}}$	0.985	0.205	71
	$K_1 + K_2\mathrm{X} + K_3\mathrm{X}^2$	1	0.03	71
	$K_1 + K_2\dfrac{\log(\mathrm{X})}{\log(K_3)}$	0.973	0.281	71
	$K_1 + K_2^{\mathrm{X}K_3}$	0	1.69	71
Re	$K_1 + K_2\mathrm{X}^{K_3}$	1	0.0121	91
	$K_1 + K_2\sqrt{\mathrm{X}}$	0.999	0.0265	91
	$K_1 + K_2\mathrm{X} + K_3\mathrm{X}^2$	1	0.016	91
	$K_1 + K_2\dfrac{\log(\mathrm{X})}{\log(K_3)}$	1	0.0154	91
	$K_1 + K_2^{\mathrm{X}K_3}$	NaN	∞	-
M_{max}	$K_1 + K_2\mathrm{X}^{K_3}$	0.003	34.4	97
	$K_1 + K_2\sqrt{\mathrm{X}}$	0.0179	1.26	97
	$K_1 + K_2\mathrm{X} + K_3\mathrm{X}^2$	0.405	0.984	97
	$K_1 + K_2\dfrac{\log(\mathrm{X})}{\log(K_3)}$	NaN	∞	-
	$K_1 + K_2^{\mathrm{X}K_3}$	0	1.26	97

Table 3.21: Selected uni-variate non-linear fits summarized for thermal conversion efficiency in domain $\mathbb{A}_1$

Summary of Results			
Independent Variable	Model Fit	R^2	RMSE
$T_{\infty,h}$	$-4.614 + (6.963 \cdot 10^{-3})\mathrm{X}^{1.118}$	0.996	0.113
Re	$-3.158 + 0.429\mathrm{X}^{0.320}$	1	0.012
M_{max}	$5.966 + 0.0958\mathrm{X} - (1.036 \cdot 10^{-3})\mathrm{X}^2$	0.405	0.984

3.4.1.3 Performance Index

Based on R^2 values, the best fit for the performance index as a function of inlet fluid temperature is a second order polynomial function. The model was chosen due to its R^2 value being the highest and its RMSE being the lowest among other models. Figure 3.25 shows the performance index plotted over a finer interval of inlet fluid temperature. Included are the predicted values of the model fit and the 95% confidence intervals, of which has an average half-width of 0.465. The results of other less useful model fits are listed in table 3.22.

Based on R^2 values, the best fit for the performance index as a function of inlet Reynolds number is the second order polynomial function. The model was chosen due to its R^2 value being the highest and its RMSE being the lowest among other models. Figure 3.26 shows the performance index plotted over a finer interval of inlet Reynolds number. Included are the predicted values of the model fit and the 95% confidence intervals, of which has an average half-width of 3.167. The results of other less useful model fits are listed in table 3.22.

Based on R^2 values, the best fit for the performance index as a function of maximum pins per row is the power function. The model was chosen due to its R^2 value being the highest and its RMSE being the lowest among other models. Figure 3.27 shows the performance index plotted over a finer interval of maximum pins per row. Included are the predicted values of the model fit and the 95% confidence intervals, of which has an average half-width of 0.116. The results of other less useful model fits are listed in table 3.22.

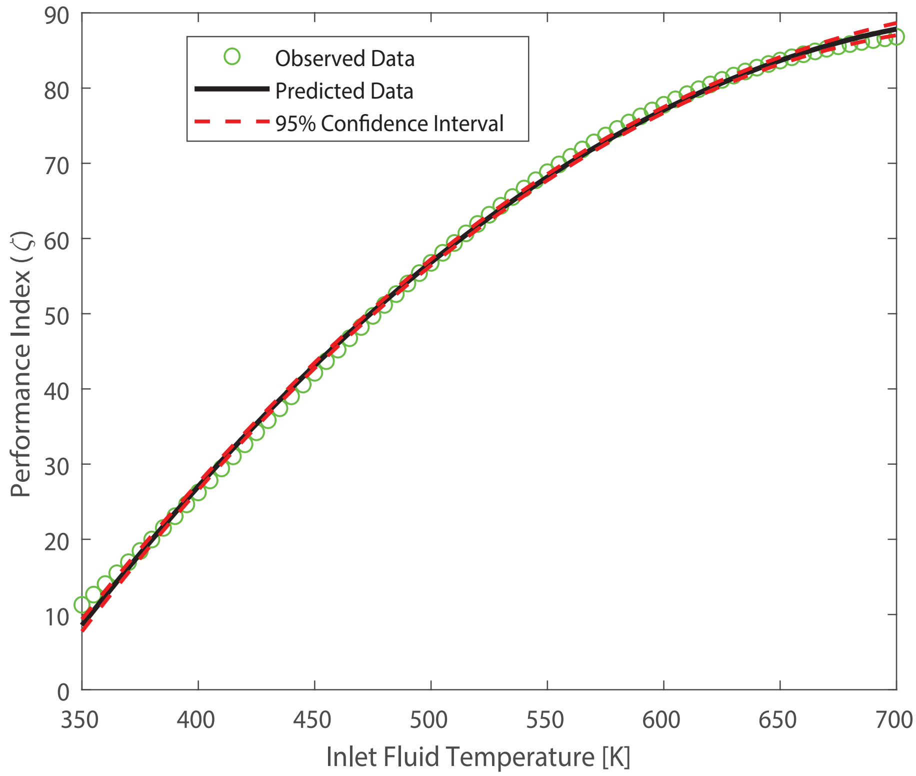

Figure 3.25: Performance index versus inlet fluid temperature

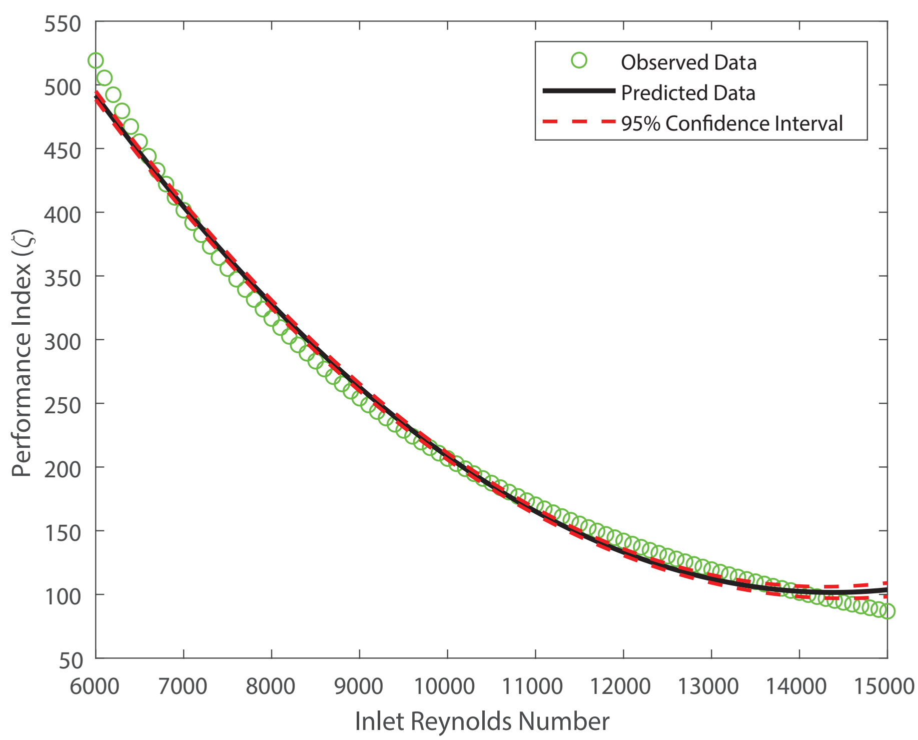

Figure 3.26: Performance index versus inlet Reynolds number

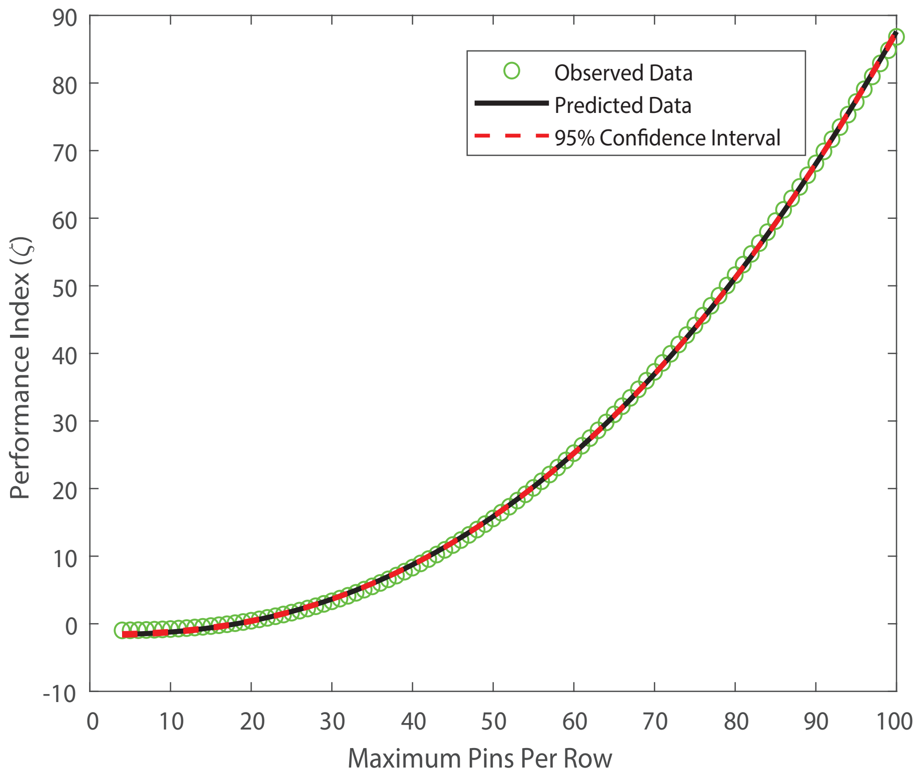

Figure 3.27: Performance index versus maximum pins per row

Table 3.22: Uni-variate non-linear regression results for performance index versus independent variables in domain $\mathbb{A}_1$

Performance Index Model Fits				
Independent variable	Model Fits	R^2	RMSE	Observations
$T_{\infty,h}$	$K_1 + K_2 X^{K_3}$	0.978	3.63	71
	$K_1 + K_2\sqrt{X}$	0.978	3.60	71
	$K_1 + K_2 X + K_3 X^2$	1	0.815	71
	$K_1 + K_2 \frac{\log(X)}{\log(K_3)}$	NaN	∞	-
	$K_1 + K_2^{XK_3}$	0.795	10.9	71
Re	$K_1 + K_2 X^{K_3}$	0.005	119	91
	$K_1 + K_2\sqrt{X}$	0.941	29	91
	$K_1 + K_2 X + K_3 X^2$	0.995	8.78	91
	$K_1 + K_2 \frac{\log(X)}{\log(K_3)}$	NaN	∞	-
	$K_1 + K_2^{XK_3}$	NaN	∞	-
M_{max}	$K_1 + K_2 X^{K_3}$	1	0.34	97
	$K_1 + K_2\sqrt{X}$	0.804	11.8	97
	$K_1 + K_2 X + K_3 X^2$	1	0.439	97
	$K_1 + K_2 \frac{\log(X)}{\log(K_3)}$	NaN	∞	-
	$K_1 + K_2^{XK_3}$	0.947	6.17	97

Table 3.23: Selected uni-variate non-linear fits summarized for performance index in domain $\mathbb{A}_1$

Summary of Results			
Independent Variable	Model Fit	R^2	RMSE
$T_{\infty,h}$	$-187.440 + 0.727X - (4.764 \cdot 10^{-4})X^2$	1	0.815
Re	$1250 - 0.159X + (5.549 \cdot 10^{-6})X^2$	0.995	8.78
M_{max}	$-1.622 + (1.777 \cdot 10^{-3})X^{2.350}$	1	0.340

3.4.2 Equation Set $\mathbb{Z}_2$

The equations of set $\mathbb{Z}_2$ define independent variables with numeric values that ensure the iTED is rated to produce the maximum possible thermal conversion efficiency based on the data of the parametric study. Each performance solution of this set exists in the domain $\mathbb{A}_2$, where the independent variables are defined in table 3.17. Inlet fluid temperature, thermoelectric material length and pin diameter are varied when they are the independent variable being plotted over. In the following subsections, each performance solution will be plotted over a finer domain of the aforementioned variables.

3.4.2.1 Electrical Power Output Based on R^2 values, the best fit for the power output as a function of inlet fluid temperature is the second order polynomial function. The model was chosen due to its R^2 value being the highest and its RMSE being the lowest among other models. Figure 3.28 shows the power output plotted over a finer interval of inlet fluid temperature. Included are the predicted values of the model fit and the 95% confidence intervals, of which has an average half-width of 0.163 [W]. The results of other less useful model fits are listed in table 3.24.

Based on R^2 values, the best fit for the power output as a function of thermoelectric material length is the power function. The model was chosen due to its R^2 value being the highest and its RMSE being the lowest among other models. Figure 3.29 shows the power output plotted over a finer interval of thermoelectric material length. Included are the predicted values of the model fit and the 95% confidence intervals, of which has an average half-width of 1.781 [W]. The results of other less useful model fits are listed in table 3.24.

Based on R^2 values, the best fit for the power output as a function of pin diameter is the second order polynomial. The model was chosen due to its R^2 value being the highest and its RMSE being the lowest among other models. Figure 3.30 shows the power output plotted over a finer interval of pin diameter. Included are the predicted values of the model fit and the 95% confidence intervals, of which has an average half-width of 2.712 [W]. The results of other less useful model fits are listed in table 3.24.

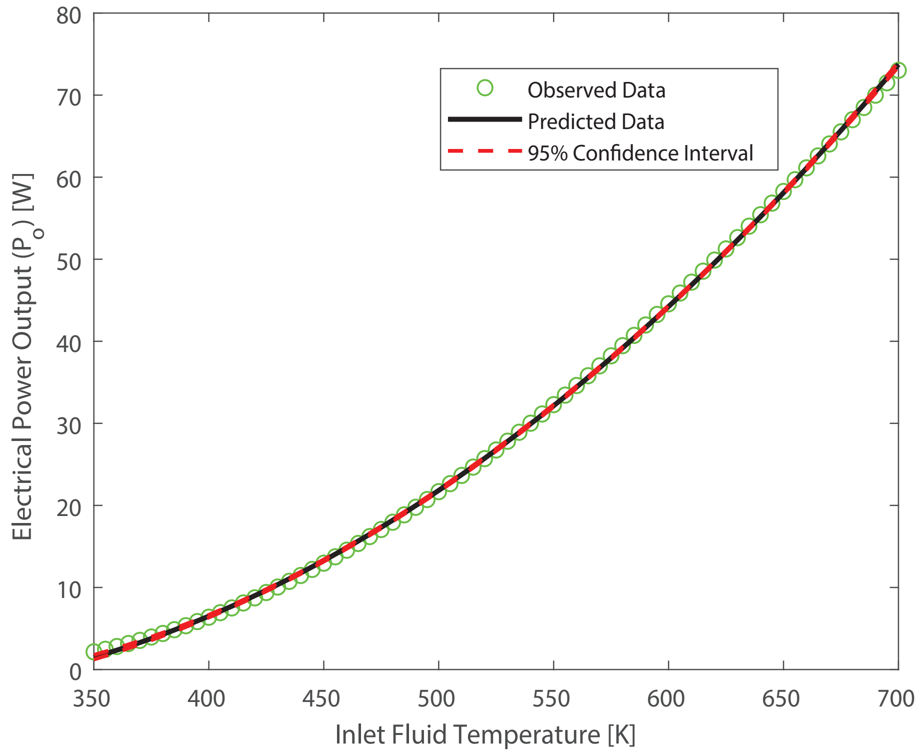

Figure 3.28: Thermal conversion efficiency versus inlet fluid temperature

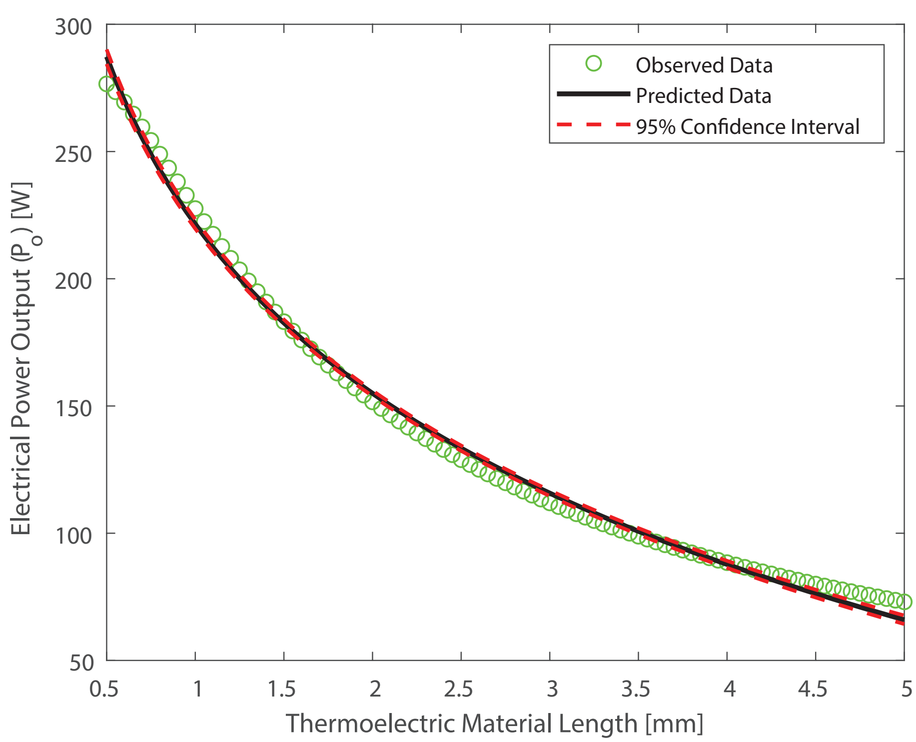

Figure 3.29: Thermal conversion efficiency versus thermoelectic material length

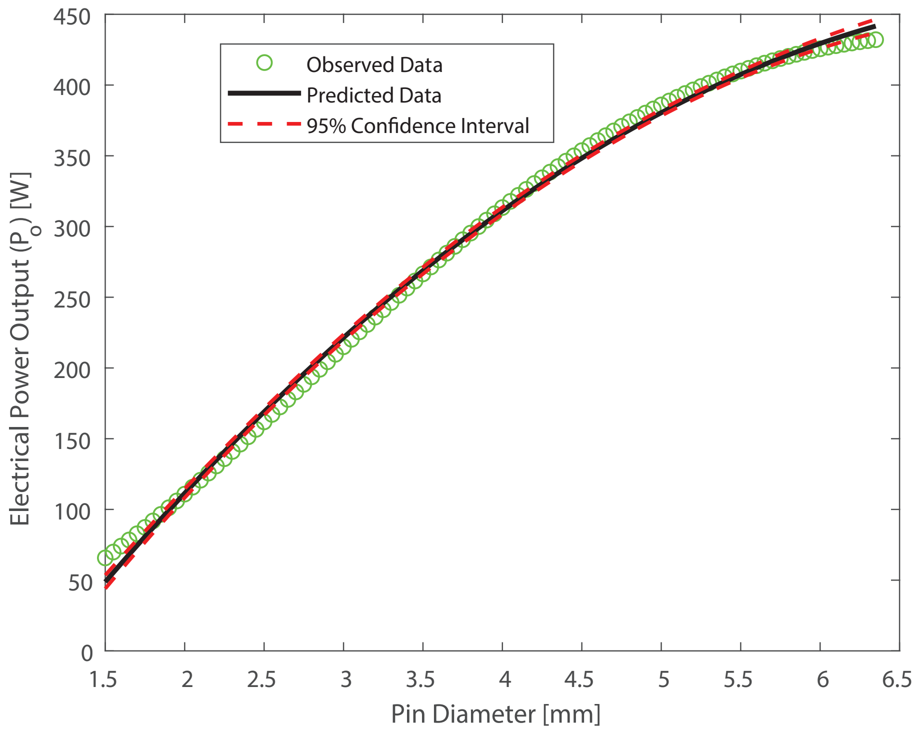

Figure 3.30: Thermal conversion efficiency versus pin diameter

Table 3.24: Uni-variate non-linear regression results for thermal conversion efficiency versus independent variables in domain $\mathbb{A}_2$

Electrical Power Output Model Fits				
Independent variable	Model Fits	R^2	RMSE	Observations
$T_{\infty,h}$	$K_1 + K_2X^{K_3}$	0.995	1.58	71
	$K_1 + K_2\sqrt{X}$	0.960	4.34	71
	$K_1 + K_2X + K_3X^2$	1	0.285	71
	$K_1 + K_2\frac{\log(X)}{\log(K_3)}$	NaN	∞	-
	$K_1 + K_2^{XK_3}$	0.982	2.9	71
$t_{N,P}$	$K_1 + K_2X^{K_3}$	0.995	3.96	91
	$K_1 + K_2\sqrt{X}$	0.966	10.8	91
	$K_1 + K_2X + K_3X^2$	0.994	4.49	91
	$K_1 + K_2\frac{\log(X)}{\log(K_3)}$	NaN	∞	-
	$K_1 + K_2^{XK_3}$	NaN	∞	-
D_{pin}	$K_1 + K_2X^{K_3}$	0.994	9.39	98
	$K_1 + K_2\sqrt{X}$	0.991	11.1	98
	$K_1 + K_2X + K_3X^2$	0.998	5.63	97
	$K_1 + K_2\frac{\log(X)}{\log(K_3)}$	NaN	∞	-
	$K_1 + K_2^{XK_3}$	0.621	72.7	98

Table 3.25: Best uni-variate non-linear fits summarized for electrical power output in domain $\mathbb{A}_2$

Summary of Results			
Independent Variable	Model Fit	R^2	RMSE
$T_{\infty,h}$	$16.076 - 0.166X + (3.543 \cdot 10^{-4})X^2$	1	0.285
$t_{N,P}$	$6454.8 - 6233.4X^{0.015}$	0.995	3.960
D_{pin}	$-169.790 + 160.970X - 10.185X^2$	0.998	5.63

3.4.2.2 Thermal Conversion Efficiency Based on R^2 values, the best fit for the thermal conversion efficiency as a function of inlet fluid temperature is the root function. The model was chosen due to its R^2 value being one of the highest and its RMSE being one of the lowest among other models. While the second order polynomial has an equal R^2 value and a lower RMSE, it is predicted its inflection point will deviate the model from the thermal conversion efficiency at larger inlet fluid temperatures compared to the root function. Figure 3.31 shows the thermal conversion efficiency plotted over a finer interval of inlet fluid temperature. Included are the predicted values of the model fit and the 95% confidence intervals, of which has an average half-width of 0.015 percentage points. The results of other less useful model fits are listed in table 3.26.

Based on R^2 values, the best fit for the thermal conversion efficiency as a function of thermoelectric material length is a logarithmic function. The model was chosen due to its R^2 value being one of the highest and its RMSE being one of the lowest among other models. While the second order polynomial has a higher R^2 value and a lower RMSE, it is predicted its inflection point will deviate the model from the thermal conversion efficiency at larger thermoelectric material lengths compared to the logarithmic function. Figure 3.32 shows the thermal conversion efficiency plotted over a finer interval of thermoelectric material length. Included are the predicted values of the model fit and the 95% confidence intervals, of which has an average half-width of 0.078 percentage points. The results of other less useful model fits are listed in table 3.26.

Based on R^2 values, the best fit for the thermal conversion efficiency as a function of pin diameter is a second order polynomial. The model was chosen due to its R^2 value being one the highest and its RMSE being the lowest among other models. Figure 3.33 shows the power output plotted over a finer interval of pin diameter. Included are the predicted values of the model fit and the 95% confidence intervals, of which has an average half-width of 2.712 [W]. The results of other less useful model fits are listed in table 3.26. These results will be discussed later in the work.

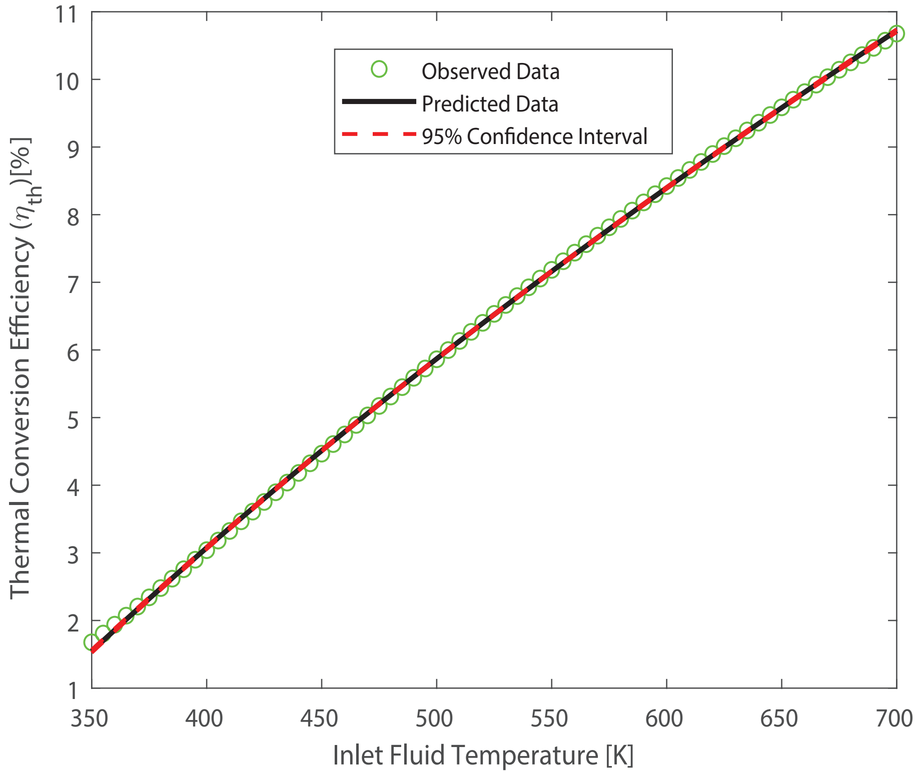

Figure 3.31: Thermal conversion efficiency versus inlet fluid temperature

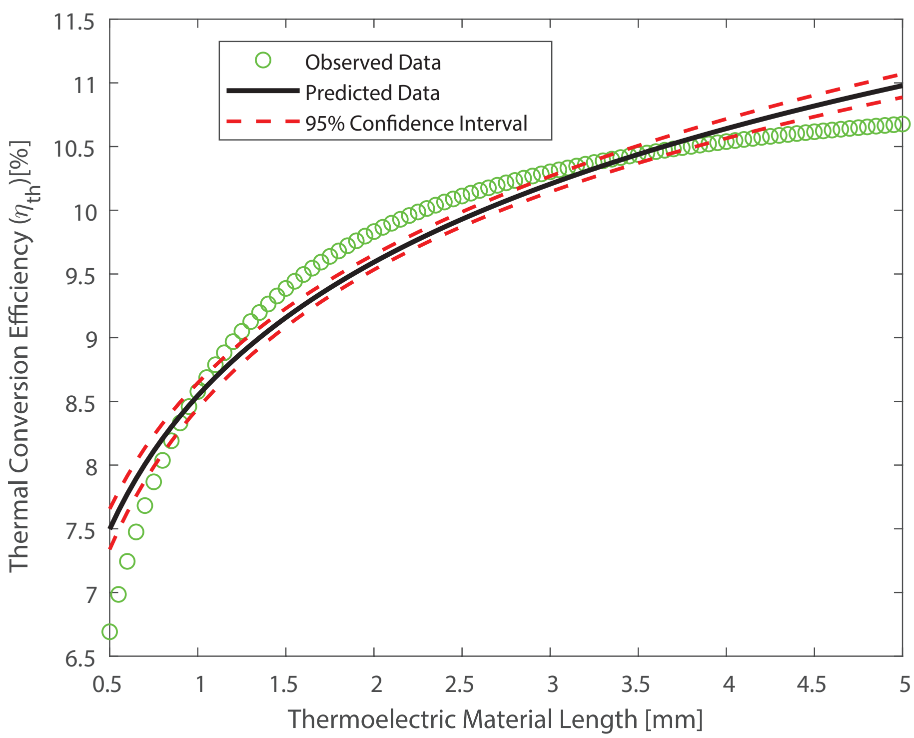

Figure 3.32: Thermal conversion efficiency versus thermoelectric material length

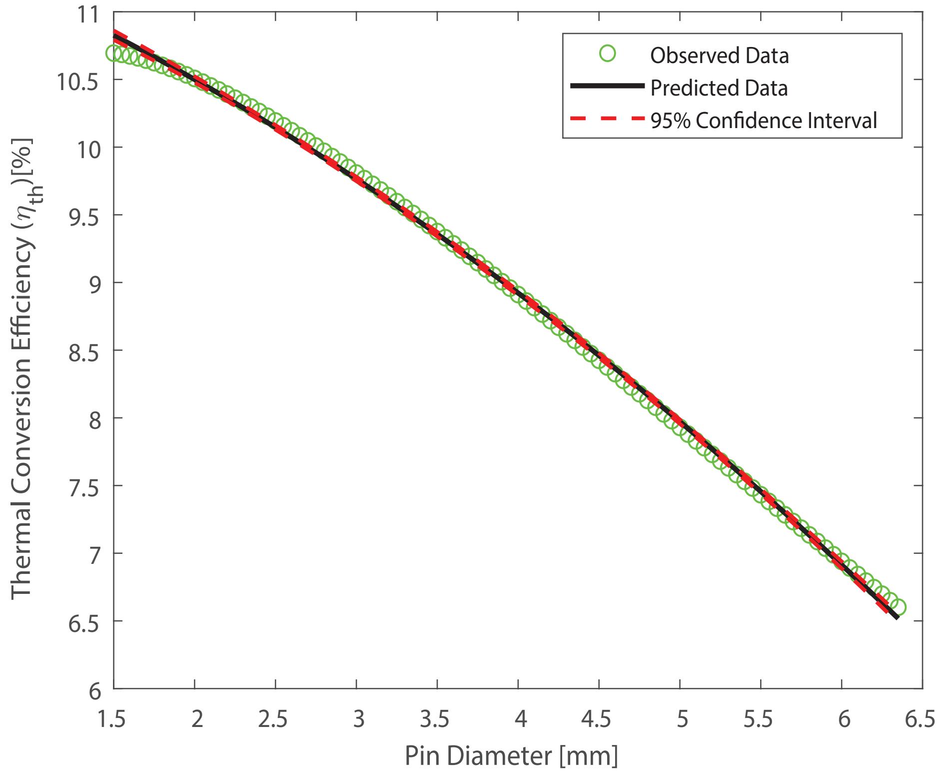

Figure 3.33: Thermal conversion efficiency versus pin diameter

Table 3.26: Uni-variate non-linear regression results for thermal conversion efficiency versus independent variables in domain $\mathbb{A}_2$

Thermal Conversion Efficiency Model Fits				
Independent variable	Model Fits	R^2	RMSE	Observations
$T_{\infty,h}$	$K_1 + K_2\mathrm{X}^{K_3}$	1	0.036	71
	$K_1 + K_2\sqrt{\mathrm{X}}$	1	0.022	71
	$K_1 + K_2\mathrm{X} + K_3\mathrm{X}^2$	1	0.026	71
	$K_1 + K_2\dfrac{\log(\mathrm{X})}{\log(K_3)}$	0.982	2.9	71
	$K_1 + K_2^{\mathrm{X}K_3}$	0.958	0.56	71
$t_{N,P}$	$K_1 + K_2\mathrm{X}^{K_3}$	0.945	0.22	91
	$K_1 + K_2\sqrt{\mathrm{X}}$	0.862	0.350	91
	$K_1 + K_2\mathrm{X} + K_3\mathrm{X}^2$	0.949	0.213	91
	$K_1 + K_2\dfrac{\log(\mathrm{X})}{\log(K_3)}$	0.946	0.219	91
	$K_1 + K_2^{\mathrm{X}K_3}$	0.644	0.565	91
D_{pin}	$K_1 + K_2\mathrm{X}^{K_3}$	0.931	0.335	98
	$K_1 + K_2\sqrt{\mathrm{X}}$	0.971	0.217	98
	$K_1 + K_2\mathrm{X} + K_3\mathrm{X}^2$	0.999	0.041	98
	$K_1 + K_2\dfrac{\log(\mathrm{X})}{\log(K_3)}$	NaN	∞	-
	$K_1 + K_2^{\mathrm{X}K_3}$	0.203	1.14	98

Table 3.27: Best uni-variate non-linear fits summarized for thermal conversion efficiency in domain $\mathbb{A}_2$

Summary of Results			
Independent Variable	Model Fit	R^2	RMSE
$T_{\infty,h}$	$-20.606 + 1.184\sqrt{\mathrm{X}}$	1	0.022
$t_{N,P}$	$8.545 - 0.166\dfrac{\log(\mathrm{X})}{\log(0.892)}$	0.946	0.219
D_{pin}	$11.646 - 0.465\mathrm{X} - 0.054\mathrm{X}^2$	0.999	0.041

3.4.2.3 Performance Index

Based on R^2 values, the best fit for the performance index as a function of inlet fluid temperature is the second order polynomial function. The model was chosen due to its R^2 value being the highest and its RMSE being the lowest. Figure 3.34 shows the performance index plotted over a finer interval of inlet fluid temperature. Included are the predicted values of the model fit and the 95% confidence intervals, of which has an average half-width of 0.235. The results of other less useful model fits are listed in table 3.28.

Based on R^2 values, the best fit for the performance index as a function of thermoelectric material length is the power function. The model was chosen due to its R^2 value being one of the highest and its RMSE being one of the lowest among other models. While the second order polynomial has a higher R^2 value and a lower RMSE, it is predicted its inflection point will deviate the model from the performance index at larger thermoelectric material lengths compared to the power function. Figure 3.35 shows the performance index plotted over a finer interval of thermoelectric material length. Included are the predicted values of the model fit and the 95% confidence intervals, of which has an average half-width of 0.307. The results of other less useful model fits are listed in table 3.28.

Based on R^2 values, the best fit for the performance index as a function of pin diameter is the power function. The model was chosen due to its R^2 value being one of the highest and its RMSE being the lowest. While the second order polynomial has a higher R^2 value and a lower RMSE, it is predicted its inflection point will deviate the model from the performance index at a larger pin diameter compared to the power function. Figure 3.36 shows the power output plotted over a finer interval of pin diameter. Included are the predicted values of the model fit and the 95% confidence intervals, of which has an average half-width of 5.0457. The results of other less useful model fits are listed in table 3.28.

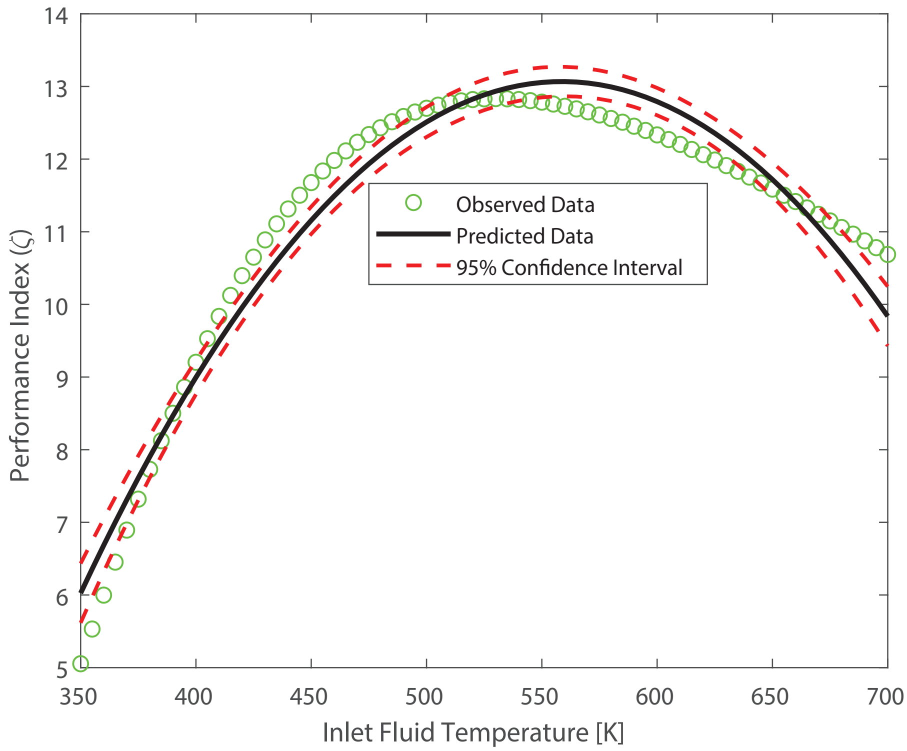

Figure 3.34: Performance index versus inlet fluid temperature

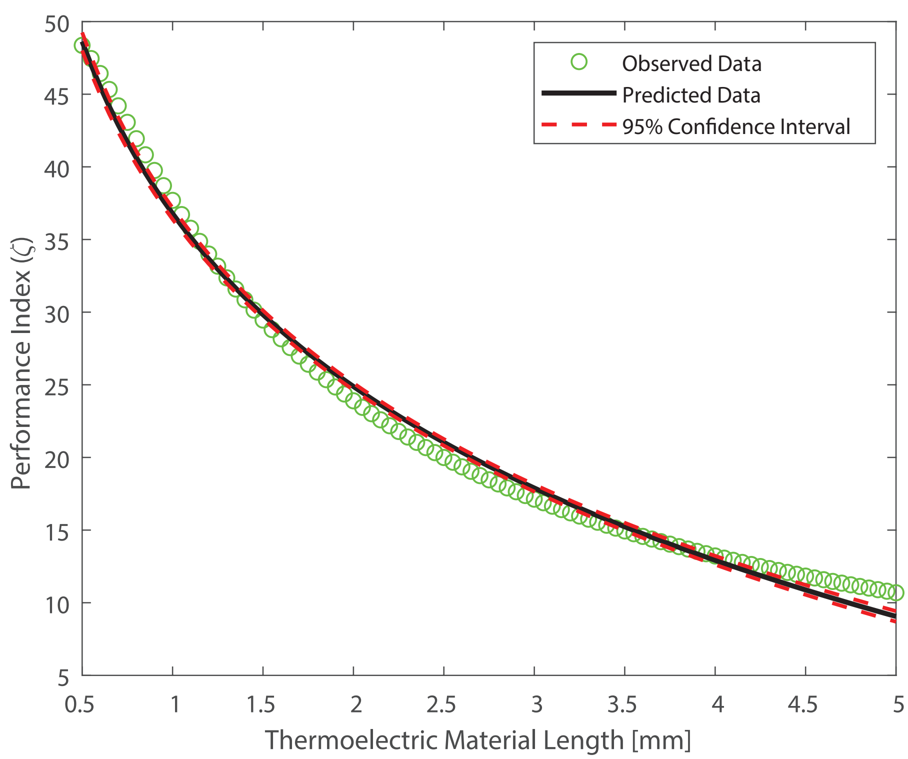

Figure 3.35: Performance index versus thermoelectic material length

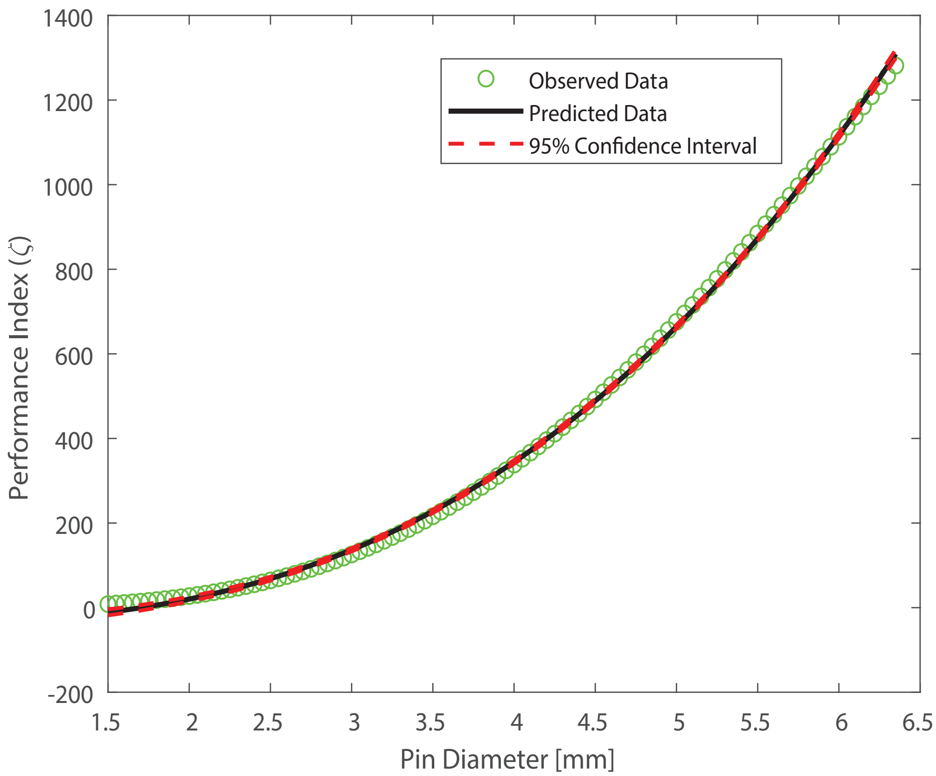

Figure 3.36: Performance index versus pin diameter

Table 3.28: Uni-variate non-linear regression results for performance index versus independent variables in domain $\mathbb{A}_2$

Performance Index Model Fits				
Independent variable	Model Fits	R^2	RMSE	Observations
$T_{\infty,h}$	$K_1 + K_2\mathrm{X}^{K_3}$	0.409	1.510	71
	$K_1 + K_2\sqrt{\mathrm{X}}$	0.378	0.369	71
	$K_1 + K_2\mathrm{X} + K_3\mathrm{X}^2$	0.956	0.026	71
	$K_1 + K_2\dfrac{\log(\mathrm{X})}{\log(K_3)}$	NaN	∞	-
	$K_1 + K_2^{\mathrm{X}K_3}$	NaN	∞	-
$t_{N,P}$	$K_1 + K_2\mathrm{X}^{K_3}$	0.997	0.570	91
	$K_1 + K_2\sqrt{\mathrm{X}}$	0.953	2.26	91
	$K_1 + K_2\mathrm{X} + K_3\mathrm{X}^2$	0.99	1.04	91
	$K_1 + K_2\dfrac{\log(\mathrm{X})}{\log(K_3)}$	NaN	∞	-
	$K_1 + K_2^{\mathrm{X}K_3}$	NaN	∞	-
D_{pin}	$K_1 + K_2\mathrm{X}^{K_3}$	0.999	10.5	98
	$K_1 + K_2\sqrt{\mathrm{X}}$	NaN	∞	-
	$K_1 + K_2\mathrm{X} + K_3\mathrm{X}^2$	1	4.27	98
	$K_1 + K_2\dfrac{\log(\mathrm{X})}{\log(K_3)}$	NaN	∞	-
	$K_1 + K_2^{\mathrm{X}K_3}$	0.875	139	98

Table 3.29: Best uni-variate non-linear fits summarized for performance index in domain $\mathbb{A}_2$

Summary of Results			
Independent Variable	Model Fit	R^2	RMSE
$T_{\infty,h}$	$-37.412 + 0.181\mathrm{X} - (1.617 \cdot 10^{-4})\mathrm{X}^2$	0.956	0.412
$t_{N,P}$	$-67.621 + 10.330\mathrm{X}^{-0.184}$	0.997	0.57
D_{pin}	$-37.336 + 8.694\mathrm{X}^{2.728}$	0.999	10.5

3.4.3 Equation Set $\mathbb{Z}_3$

The equations of set $\mathbb{Z}_3$ define independent variables with numeric values that ensure the iTED is rated to produce the maximum possible performance index based on the data of the parametric study. Each performance solution of this set exists in the domain $\mathbb{A}_3$, where the independent variables are defined in table 3.17. Maximum pin per row count, pin diameter and inlet Reynolds number are varied when they are the independent variable being plotted over. In the following subsections, each performance solution will be plotted over a finer domain of the aforementioned variables.

3.4.3.1 Electrical Power Output Based on R^2 values, the best fit for the power output as a function of maximum pins per row is the logarithmic function. The model was chosen due to its R^2 value being one of the highest and its RMSE being one of the lowest among other models. While the second order polynomial has a higher R^2 value and a lower RMSE, it is predicted its inflection point will deviate the model from the power output at a larger maximum pins per row compared to the logarithmic function. Figure 3.37 shows the power output plotted over a finer interval of maximum pins per row. Included are the predicted values of the model fit and the 95% confidence intervals, of which has an average half-width of 1.258 [W]. The results of other less useful model fits are listed in table 3.30.

Based on R^2 values, the best fit for the power output as a function of pin diameter is the second order polynomial function. The model was chosen due to its R^2 value being the highest and its RMSE being the lowest among other models. Figure 3.38 shows the power output plotted over a finer interval of pin diameter. Included are the predicted values of the model fit and the 95% confidence intervals, of which has an average half-width of 0.525 [W]. The results of other less useful model fits are listed in table 3.30.

Based on R^2 values, the best fit for the power output as a function of inlet Reynolds number is a logarithmic function. The model was chosen due to its R^2 value being one of the highest and its RMSE being one of the lowest among other models. While the second order polynomial has an equivalent R^2 value and a lower RMSE, it is predicted its inflection point will deviate the model from the power output at a larger pin diameter values compared to the logarithmic function. Figure 3.39 shows the power output plotted over a finer interval of inlet Reynolds number. Included are the predicted values of the model fit and the 95% confidence intervals, of which has an average half-width of 0.2770 [W]. The results of other less useful model fits are listed in table 3.30.

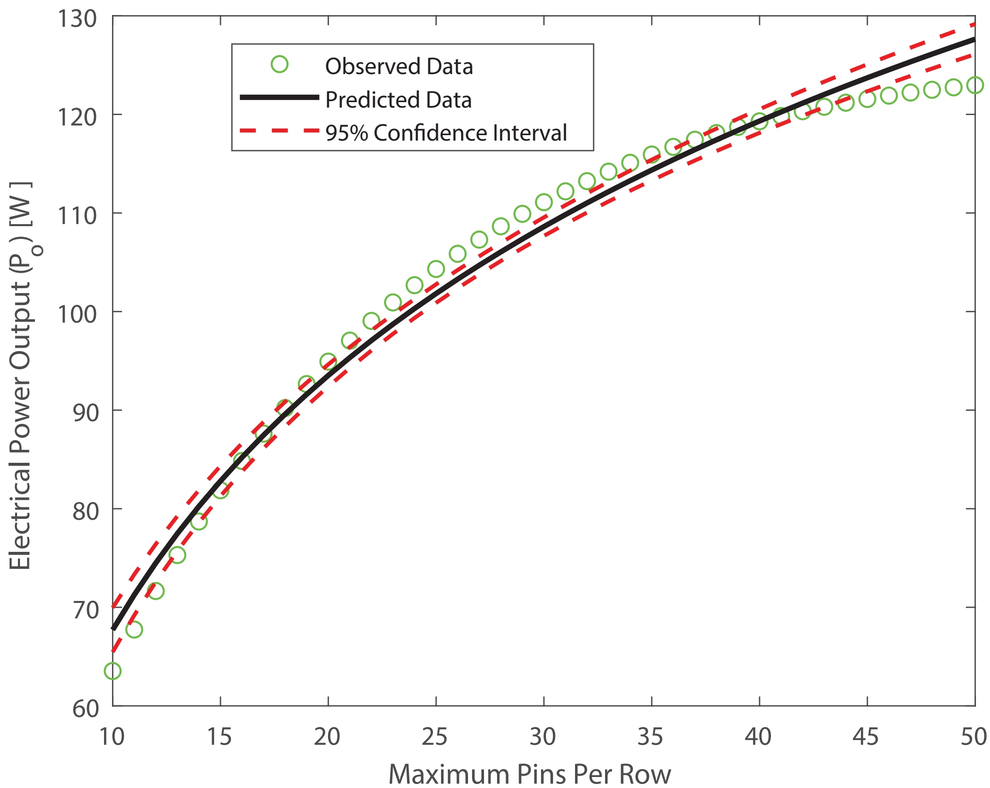

Figure 3.37: Electrical power output versus maximum pins per row

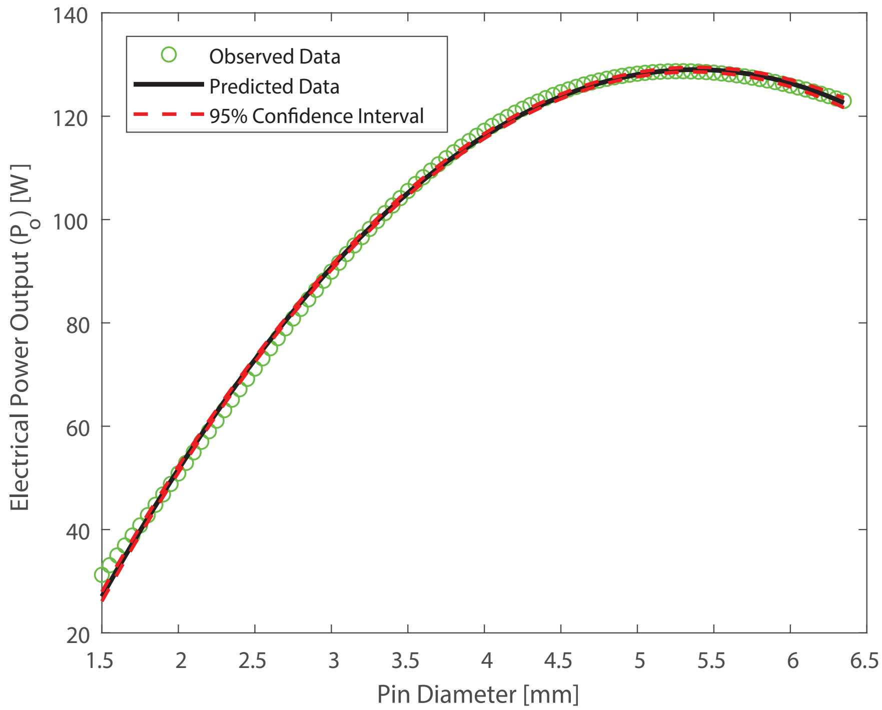

Figure 3.38: Electrical power output versus pin diameter

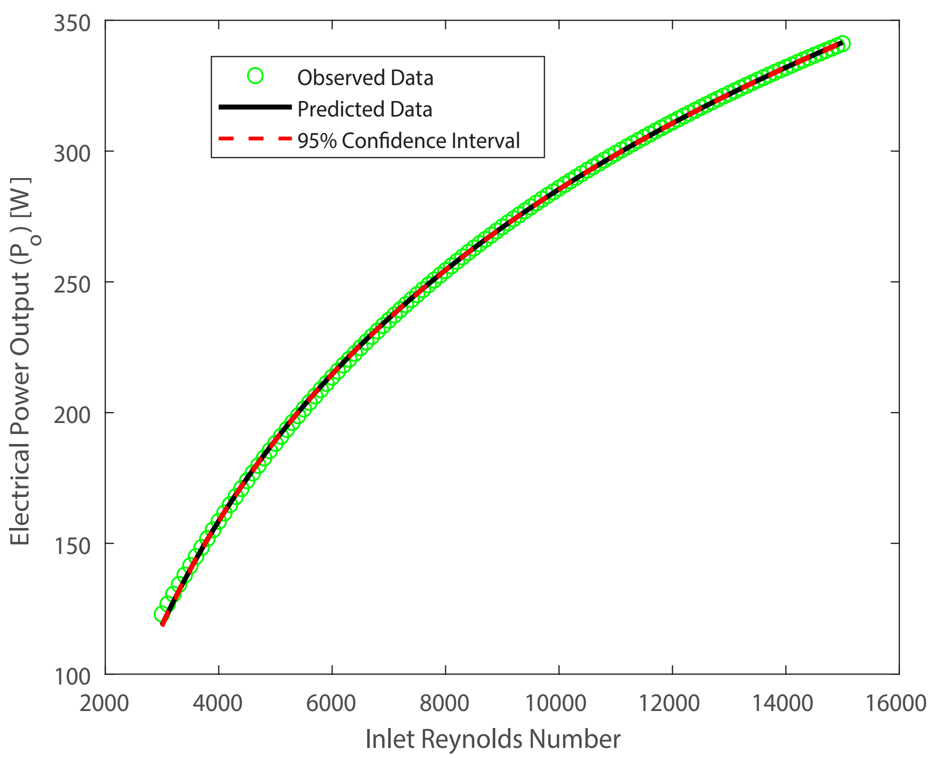

Figure 3.39: Electrical power output versus inlet Reynolds number

Table 3.30: Uni-variate non-linear regression results for electrical power output versus independent variables in domain $\mathbb{A}_3$

Electrical Power Output Model Fits				
Independent variable	Model Fits	R^2	RMSE	Observations
M_{max}	$K_1 + K_2\mathrm{X}^{K_3}$	0.979	2.570	41
	$K_1 + K_2\sqrt{\mathrm{X}}$	0.944	4.09	41
	$K_1 + K_2\mathrm{X} + K_3\mathrm{X}^2$	0.995	1.21	41
	$K_1 + K_2\dfrac{\log(\mathrm{X})}{\log(K_3)}$	0.982	2.31	41
	$K_1 + K_2^{\mathrm{X}K_3}$	0.591	11.2	41
D_{pin}	$K_1 + K_2\mathrm{X}^{K_3}$	NaN	∞	-
	$K_1 + K_2\sqrt{\mathrm{X}}$	0.897	9.87	98
	$K_1 + K_2\mathrm{X} + K_3\mathrm{X}^2$	0.999	1.09	98
	$K_1 + K_2\dfrac{\log(\mathrm{X})}{\log(K_3)}$	NaN	∞	-
	$K_1 + K_2^{\mathrm{X}K_3}$	0.484	22.1	98
Re	$K_1 + K_2\mathrm{X}^{K_3}$	1	1.26	121
	$K_1 + K_2\sqrt{\mathrm{X}}$	0.991	5.97	121
	$K_1 + K_2\mathrm{X} + K_3\mathrm{X}^2$	0.998	2.40	121
	$K_1 + K_2\dfrac{\log(\mathrm{X})}{\log(K_3)}$	1	0.897	121
	$K_1 + K_2^{\mathrm{X}K_3}$	0.634	37.4	121

Table 3.31: Best non-linear fits summarized for electrical power output in domain $\mathbb{A}_3$

Summary of Results			
Independent Variable	Model Fit	R^2	RMSE
M_{max}	$-18.026 + 74.854\dfrac{\log(\mathrm{X})}{\log(7.466)}$	0.982	2.310
D_{pin}	$-67.155 + 72.981\mathrm{X} - 6.7875\mathrm{X}^2$	0.999	1.090
Re	$-989.640 + 139.940\dfrac{\log(\mathrm{X})}{\log(2.7479)}$	1	0.897

3.4.3.2 Thermal Conversion Efficiency Based on R^2 values, the best fit for the thermal conversion efficiency as a function of maximum pins per row is the root function. The model was chosen due to its R^2 value being one of the highest and its RMSE being one of the lowest among other models. While the second order polynomial has a higher R^2 value and a lower RMSE, it is predicted its inflection point will deviate the model from the thermal conversion efficiency at a larger maximum pin per row count compared to the root function. Figure 3.40 shows the thermal conversion efficiency plotted over a finer interval of maximum pins per row. Included are the predicted values of the model fit and the 95% confidence intervals, of which has an average half-width of 0.0236 percentage points. The results of other less useful model fits are listed in table 3.32.

Based on R^2 values, the best fit for the thermal conversion efficiency as a function of pin diameter is a second order polynomial. The model was chosen due to its R^2 value being the highest and its RMSE being the lowest among other models. Figure 3.41 shows the thermal conversion efficiency plotted over a finer interval of pin diameter. Included are the predicted values of the model fit and the 95% confidence intervals, of which has an average half-width of 0.525 percentage points. The results of other less useful model fits are listed in table 3.32.

Based on R^2 values, the best fit for the thermal conversion efficiency as a function of inlet Reynolds number is a logarithmic function. The model was chosen due to its R^2 value being the highest and its RMSE being the lowest among other models. Figure 3.42 shows the thermal conversion efficiency plotted over a finer interval of inlet Reynolds number. Included are the predicted values of the model fit and the 95% confidence intervals, of which has an average half-width of 0.2770 percentage points. The results of other less useful model fits are listed in table 3.32.

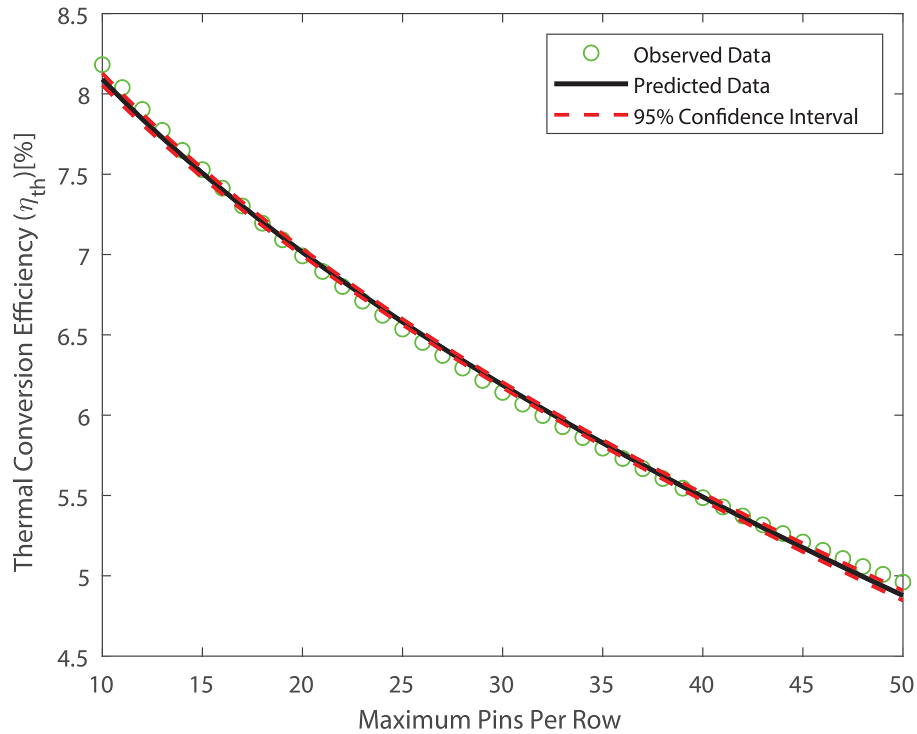

Figure 3.40: Thermal conversion efficiency versus maximum pins per row

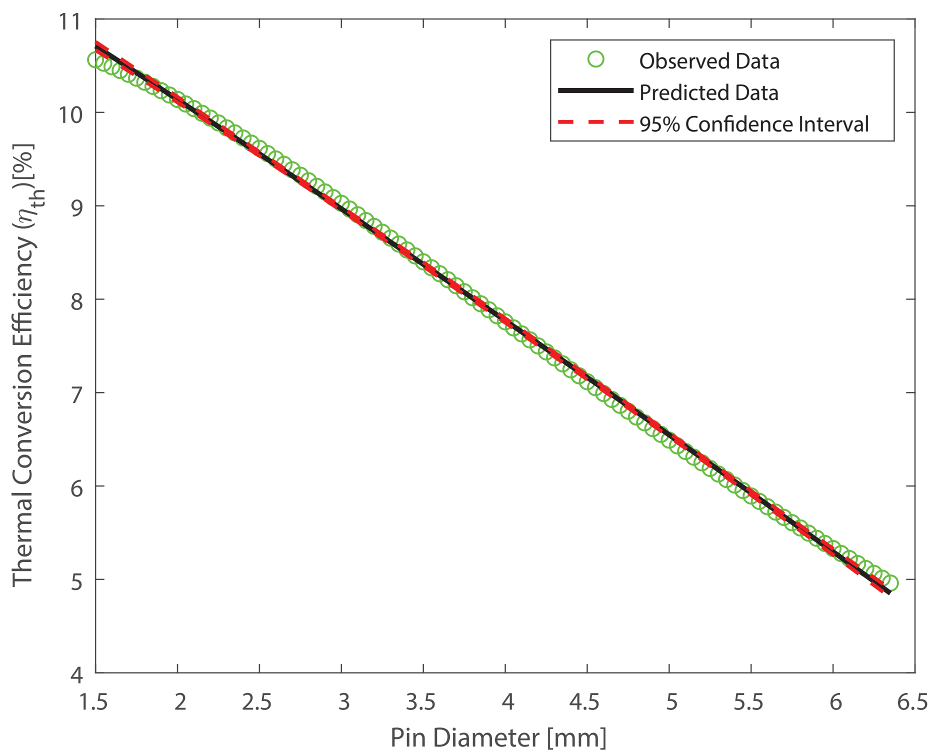

Figure 3.41: Thermal conversion efficiency versus pin diameter

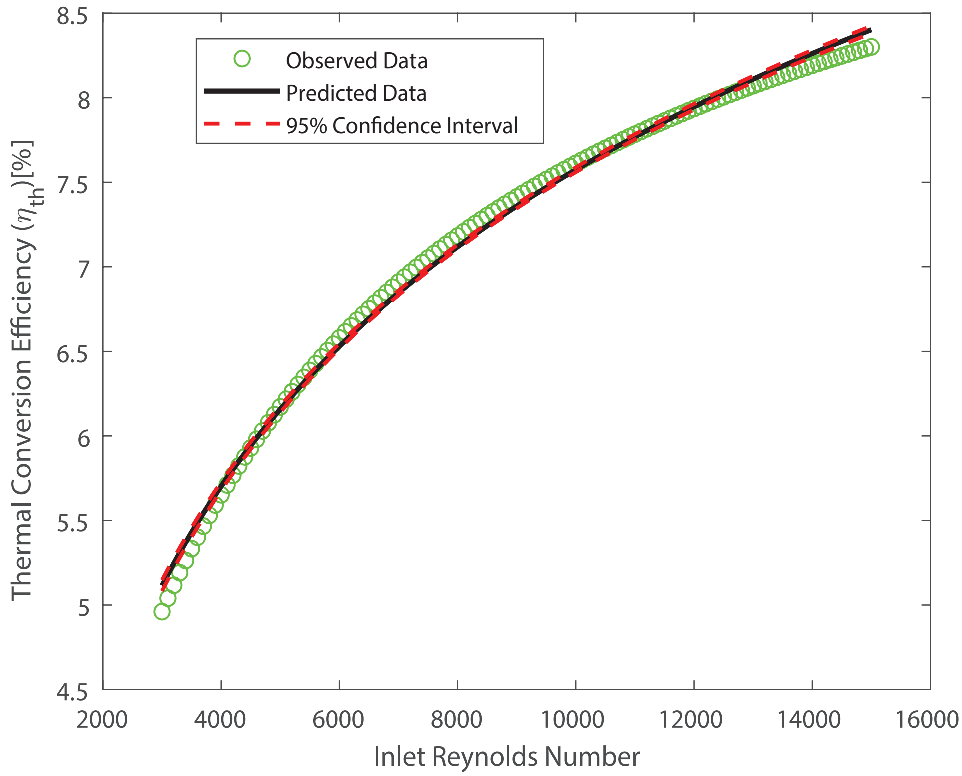

Figure 3.42: Thermal conversion efficiency versus inlet Reynolds number

Table 3.32: Uni-variate non-linear regression results for thermal conversion efficiency versus independent variables in domain $\mathbb{A}_3$

Thermal Conversion Efficiency Model Fits				
Independent variable	Model Fits	R^2	RMSE	Observations
M_{max}	$K_1 + K_2\mathrm{X}^{K_3}$	0.995	0.0682	41
	$K_1 + K_2\sqrt{\mathrm{X}}$	0.998	0.0432	41
	$K_1 + K_2\mathrm{X} + K_3\mathrm{X}^2$	0.999	0.0238	41
	$K_1 + K_2\frac{\log(\mathrm{X})}{\log(K_3)}$	NaN	∞	-
	$K_1 + K_2^{\mathrm{X}K_3}$	0.306	0.805	41
D_{pin}	$K_1 + K_2\mathrm{X}^{K_3}$	0.958	0.355	98
	$K_1 + K_2\sqrt{\mathrm{X}}$	0.988	0.193	98
	$K_1 + K_2\mathrm{X} + K_3\mathrm{X}^2$	0.999	0.0521	98
	$K_1 + K_2\frac{\log(\mathrm{X})}{\log(K_3)}$	NaN	∞	-
	$K_1 + K_2^{\mathrm{X}K_3}$	0.154	1.60	98
Re	$K_1 + K_2\mathrm{X}^{K_3}$	0.991	0.0891	121
	$K_1 + K_2\sqrt{\mathrm{X}}$	0.972	0.151	121
	$K_1 + K_2\mathrm{X} + K_3\mathrm{X}^2$	0.995	0.0653	121
	$K_1 + K_2\frac{\log(\mathrm{X})}{\log(K_3)}$	0.996	0.0574	121
	$K_1 + K_2^{\mathrm{X}K_3}$	0.845	0.36	121

Table 3.33: Best uni-variate non-linear fits summarized for thermal conversion efficiency in domain $\mathbb{A}_3$

Summary of Results			
Independent Variable	Model Fit	R^2	RMSE
M_{max}	$10.692 - 0.8223\sqrt{\mathrm{X}}$	0.998	0.0432
D_{pin}	$12.393 - 1.1004\mathrm{X} - 0.01371\mathrm{X}^2$	0.999	0.0521
Re	$-11.239 + 8.7629\frac{\log(\mathrm{X})}{\log(72.975)}$	0.996	0.0574

3.4.3.3 Performance Index Based on R^2 values, the best fit for the performance index as a function of maximum pins per row is a power function. The model was chosen due to its R^2 value being one of the highest and its RMSE being one of the lowest among other models. While the second order polynomial has an equivalent R^2 value and a lower RMSE, it is predicted its inflection point will deviate the model from the performance index at a larger maximum pins per row compared to the power function. Figure 3.43 shows the performance index plotted over a finer interval of maximum pin per row count. Included are the predicted values of the model fit and the 95% confidence intervals, of which has an average half-width of 9.427. The results of other less useful model fits are listed in table 3.34.

Based on R^2 values, the best fit for the performance index as a function of pin diameter is a second order polynomial. The model was chosen due to its R^2 value being the highest and its RMSE being the lowest among other models. Figure 3.44 shows the performance index plotted over a finer interval of pin diameter. Included are the predicted values of the model fit and the 95% confidence intervals, of which has an average half-width of 29.145. The results of other less useful model fits are listed in table 3.34.

Based on R^2 values, the best fit for the performance index as a function of inlet Reynolds number is a power function. The model was chosen due to its R^2 value being the highest and its RMSE being the lowest among other models. Figure 3.45 shows the performance index plotted over a finer interval of inlet Reynolds number. Included are the predicted values of the model fit and the 95% confidence intervals, of which has an average half-width of 20.895. The results of other less useful model fits are listed in table 3.34.

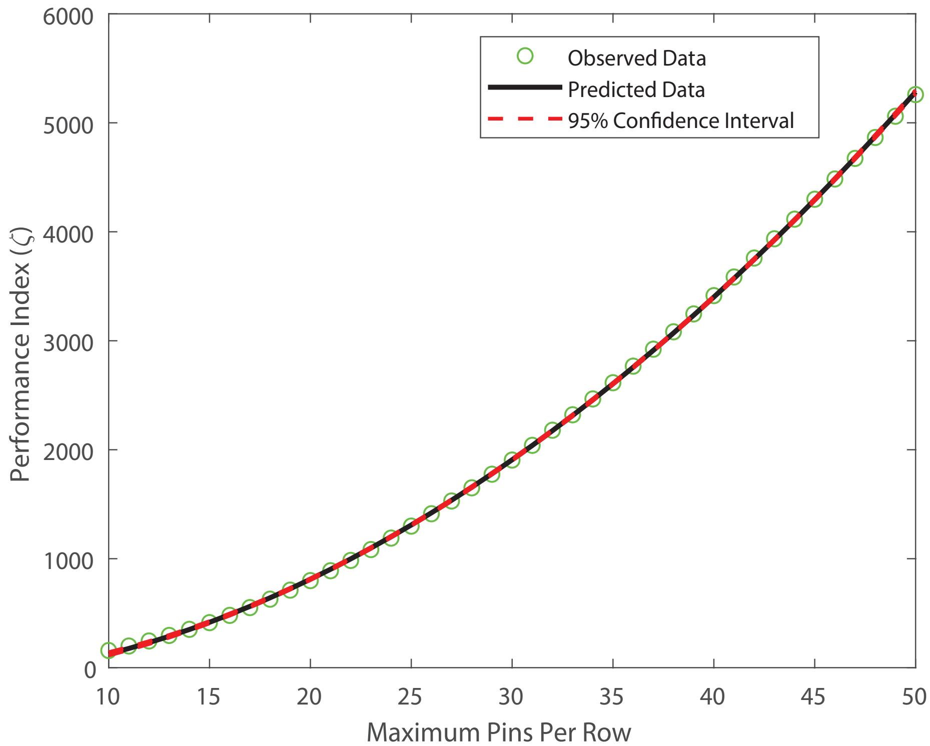

Figure 3.43: Performance index versus maximum pins per row

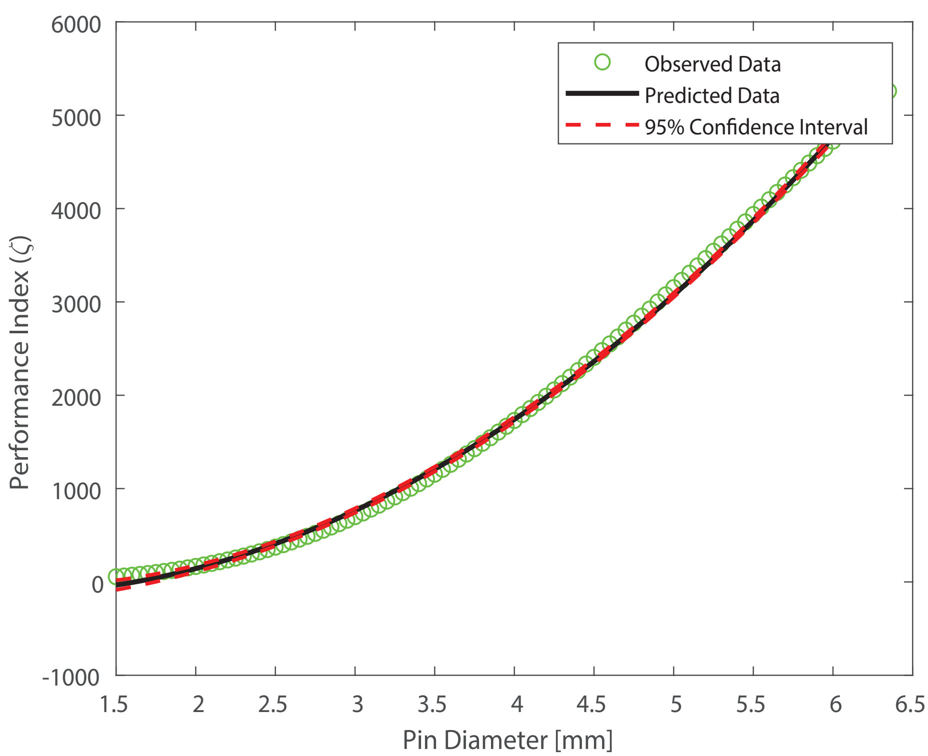

Figure 3.44: Performance index versus pin diameter

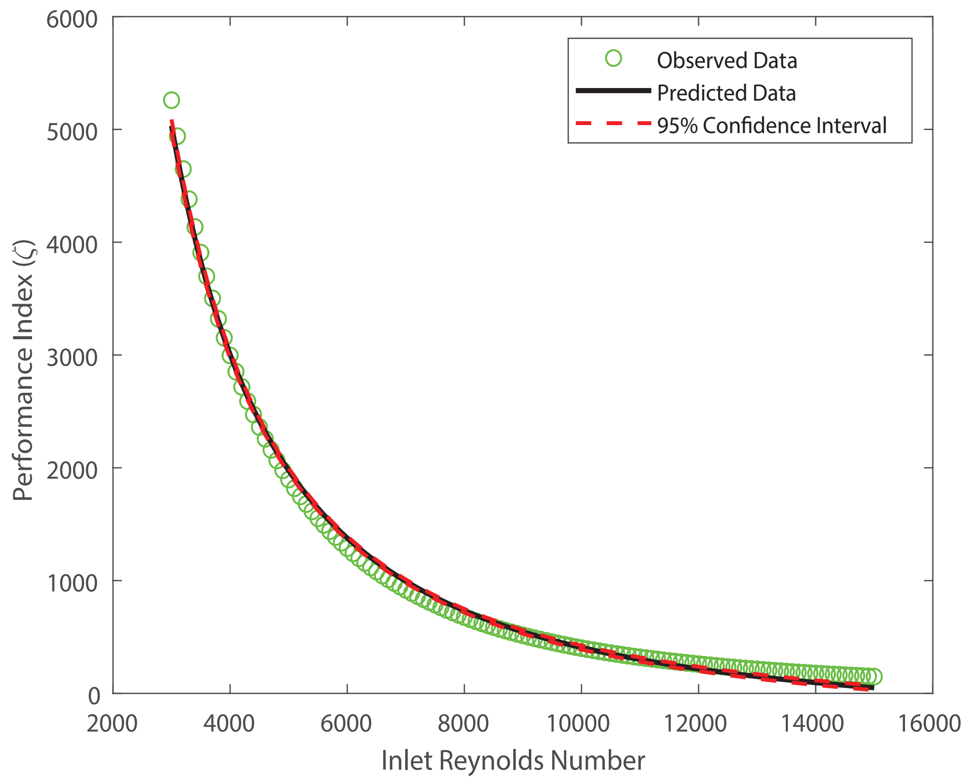

Figure 3.45: Performance index versus inlet Reynolds number

Table 3.34: Uni-variate non-linear regression results for thermal conversion efficiency versus independent variables in domain $\mathbb{A}_3$

Performance Index Model Fits				
Independent variable	Model Fits	R^2	RMSE	Observations
M_{max}	$K_1 + K_2 X^{K_3}$	1	12.3	41
	$K_1 + K_2\sqrt{X}$	0.933	411	41
	$K_1 + K_2 X + K_3 X^2$	1	0.14.8	41
	$K_1 + K_2 \frac{\log(X)}{\log(K_3)}$	0.872	568	41
	$K_1 + K_2^{X K_3}$	0.737	825	41
D_{pin}	$K_1 + K_2 X^{K_3}$	0.998	68.2	98
	$K_1 + K_2\sqrt{X}$	0.919	468	98
	$K_1 + K_2 X + K_3 X^2$	0.999	60.5	98
	$K_1 + K_2 \frac{\log(X)}{\log(K_3)}$	0.861	612	98
	$K_1 + K_2^{X K_3}$	0.762	806	98
Re	$K_1 + K_2 X^{K_3}$	0.996	69.7	121
	$K_1 + K_2\sqrt{X}$	0.765	562	121
	$K_1 + K_2 X + K_3 X^2$	0.923	321	121
	$K_1 + K_2 \frac{\log(X)}{\log(K_3)}$	NaN	∞	-
	$K_1 + K_2^{X K_3}$	NaN	∞	-

Table 3.35: Best uni-variate non-linear fits summarized for performance index in domain $\mathbb{A}_3$

Summary of Results			
Independent Variable	Model Fit	R^2	RMSE
M_{max}	$-119.420 + 2.968X^{1.919}$	1	12.3
D_{pin}	$-32.538 - 267.580X + 177.750X^2$	0.999	60.5
Re	$-323.160 + (3.0487 \cdot 10^9)X^{-1.6552}$	0.996	69.7

3.5 Multivariate Nonlinear Regression

Multivariate non-linear models are determined using the method of non-linear least squares to reduce the sum of squares of the residuals (S). It is defined as:

$$S = \sum_{i=1}^{m} (y_i - f(x_i, \boldsymbol{\beta}))^2 \tag{3.11}$$

where m is the number of observations, y is the observed value of the dependent variable, f is the regression function, x is the observed value of the independent variable and $\boldsymbol{\beta}$ is a vector of parameters for the model fit. The minimization is accomplished when the gradient of S is zero. That is:

$$\frac{\partial S}{\partial \beta_j} = 2 \sum_{i=1}^{m} (y_i - f(x_i, \boldsymbol{\beta})) \frac{\partial (y_i - f(x_i, \boldsymbol{\beta}))}{\partial \beta_j} = 0 \quad (j = 1, 2, ...n) \tag{3.12}$$

where n is the number of parameters in the vector $\boldsymbol{\beta}$. Given that the equations are non-linear, the parameters are refined iteratively until a specified convergence criterion is satisfied. The method by which these parameters are determined is dependent on the algorithm chosen. In this work, the Levenberg–Marquardt algorithm (LMA) will be used to determine the parameters.

The LMA algorithm was chosen because it interpolates between two minimization methods: the gradient descent method and the Gauss-Newton method [59, 60]. In the gradient descent method, the sum of the squared errors is reduced by updating the parameters in the steepest-descent direction [61]. In the Gauss-Newton method, the sum of the squared errors is reduced by assuming the least squares function is locally quadratic, and finding the minimum of the quadratic [62]. The advantages of the LMA is that it behaves more like the gradient descent method when parameters are far from their optimal value and acts more like the Gauss-Newton method when parameters are close to their optimal value; thus, one of two scenarios can occur. First, if initial estimates are far from their optimal values, the LMA behaves in a more robust fashion compared to the Gauss-Newton method and can potentially converge towards a local minimum. Second, if the initial estimates are close to their optimal values, the LMA is more restraint than the gradient descent method.

The LMA is housed in the MATLAB command function 'lsqcurvefit' [63]. A convergence criterion of 10^{-6} is used for the function value and the step tolerance. The gradients are determined using a forward finite difference scheme and the maximum function iteration count is set to 2,000. The remaining settings are set to default values. Initial estimates for the coefficients and the model fits will be the models fits determined in 3.5. In the case where the aforementioned criteria are not satisfied, model fit estimates will change from the values obtained in the aforementioned section to a summation of power functions and an intercept term. The validity of the models will be based on their adjusted R^2 values as well as their RMSE.

The results of the regression analysis are presented in Sections 3.5.1 - 3.5.3. The results include a series of equations to define 3.5a - 3.7c. Additionally, heat-map scatter plots of the observed data versus the aforementioned influential variables as well as function plots will be presented. The function plots will be in the form of three-dimensional heat maps. To not complicate the plots, only three values of the least influential variable of the selected independent variables chosen in 3.2.5 will be plotted.

3.5.1 Equation Set $\mathbb{Z}_1$

The equations of set $\mathbb{Z}_1$ are defined in domain $\mathbb{A}_1$, a domain defining seven independent variables that allow for the electrical power output to achieve its maximum value based on the data from the parametric study. The independent variables for the equations of set $\mathbb{Z}_1$ are inlet fluid temperature, inlet Reynolds number and maximum pins per row count. The inlet fluid temperature is measured in [K] while the remaining aforementioned variables are unit-less.

3.5.1.1 Electrical Power Output

The initial estimates for the electrical power output uses a model form given as follows:

$$f(T_{\infty,h}, \mathrm{Re}, M_{max}) = K_1 + K_2(T_{\infty,h}) + K_3(T_{\infty,h})^2 + K_4\sqrt{\mathrm{Re}} + K_5(M_{max})^{K_6} \tag{3.13}$$

Initial estimates are given by the vector $\boldsymbol{K}$ defined as:

$$\boldsymbol{K} = [-5666.1, -7.56, 0.0105, 19.054, 5531.6, 0.05973]$$

Convergence of a solution using this model fit was obtained with the function being given as:

$$P_o = -31608.166 - 3.489(T_{\infty,h}) + (5.022 \cdot 10^{-3})(T_{\infty,h})^2 + 4.108\sqrt{\mathrm{Re}} + 31,609.012(M_{max})^{0.002} \in \mathbb{A}_1 \begin{bmatrix} 3,000 \leq \mathrm{Re} \leq 15,000 \\ 350 \leq T_\infty\,[\mathrm{K}] \leq 700 \\ 4 \leq M_{max} \leq 100 \end{bmatrix} \tag{3.14}$$

The model's adjusted R^2, RMSE, maximum value and minimum value are tabulated in table 3.36.

Figure 3.46 shows three view points of a heat-map scatter plot of the raw data for power output versus inlet fluid temperature, inlet Reynolds number and maximum pin per row count. From the figure it is evident the power output converges towards its maximum at the corner where the three independent variables continue to increase. Some data points are missing in the back corner where inlet fluid temperature and Reynolds number are low and maximum pin per row count is above 40. This most likely is due to the lack of empirical data needed to define fluid Reynolds number given the influence increased pin count has on it. This data is necessary to continue solving the solution algorithm defined in Section 2.2. As a result, data for conversion efficiency and performance index in Section 3.5.1.2 - 3.5.1.3 will not exist at the same points.

Figure 3.47 is a heat-map plot representing the function given by Eq. 3.14. The trends of the model fit appear to be reflective of the raw data with some exceptions. Higher electrical power output occurs at the upper extremes of all three independent variables and a minimum occurs at the lower extremes of all three independent variable. A region of relative maximum values also appears to be concentrated in the sector where inlet fluid temperature is at the maximum value of 700 [K], inlet Reynolds number is at the maximum value of 15000 and maximum pin per row count varies above 40; thus, reinforcing the assertion that inlet fluid temperature has the most significant influence on power output. There is, however, a substantial deviation between the respective maximum and minimum values of the raw data and the model fit. It is evident the scale of the power output from the raw data has a maximum and minimum value of approximately 1200 [W] and 0 [W] respectively while the model fit has a maximum and minimum value of 700 [W] and -300 [W] respectively. This yields a 41.666 % relative difference between maximum values and a 300 [W] absolute difference between the minimum values on a scale ranging from -300 [W] to 1200 [W].

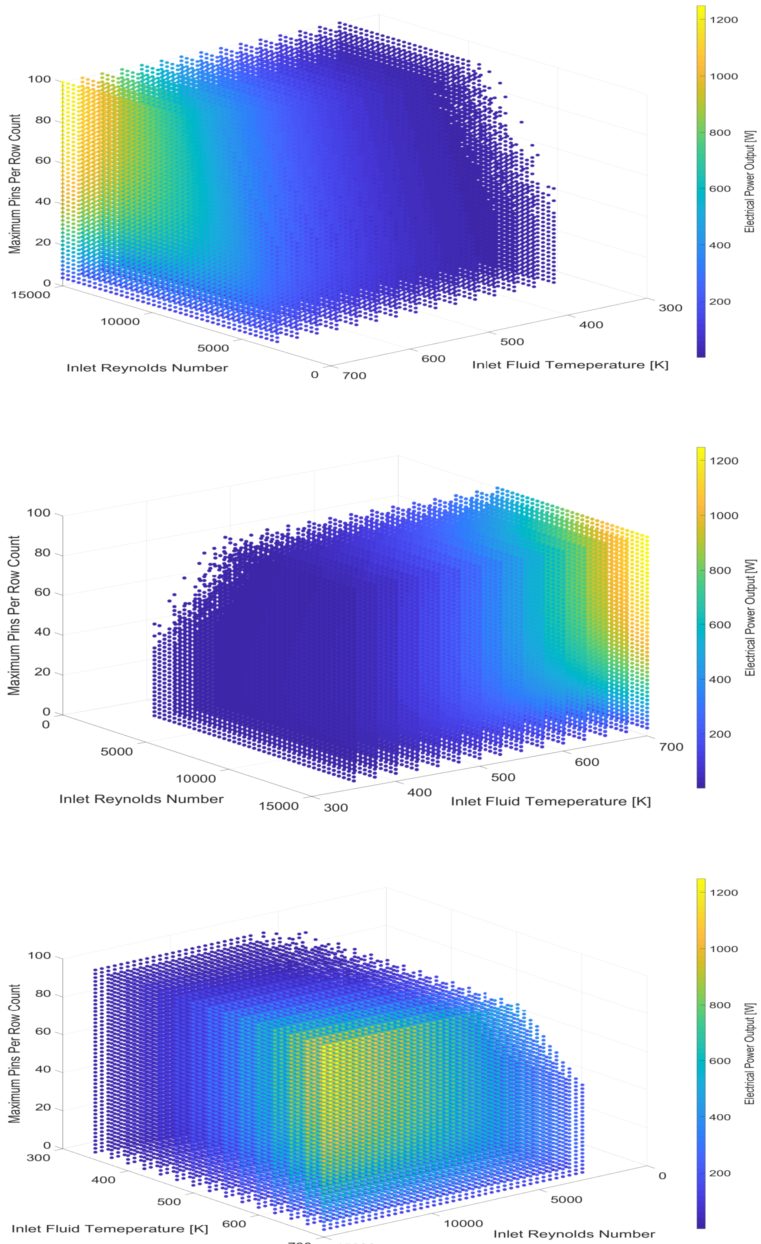

Figure 3.46: Scatter plots of electrical power output in domain $\mathbb{A}_1$

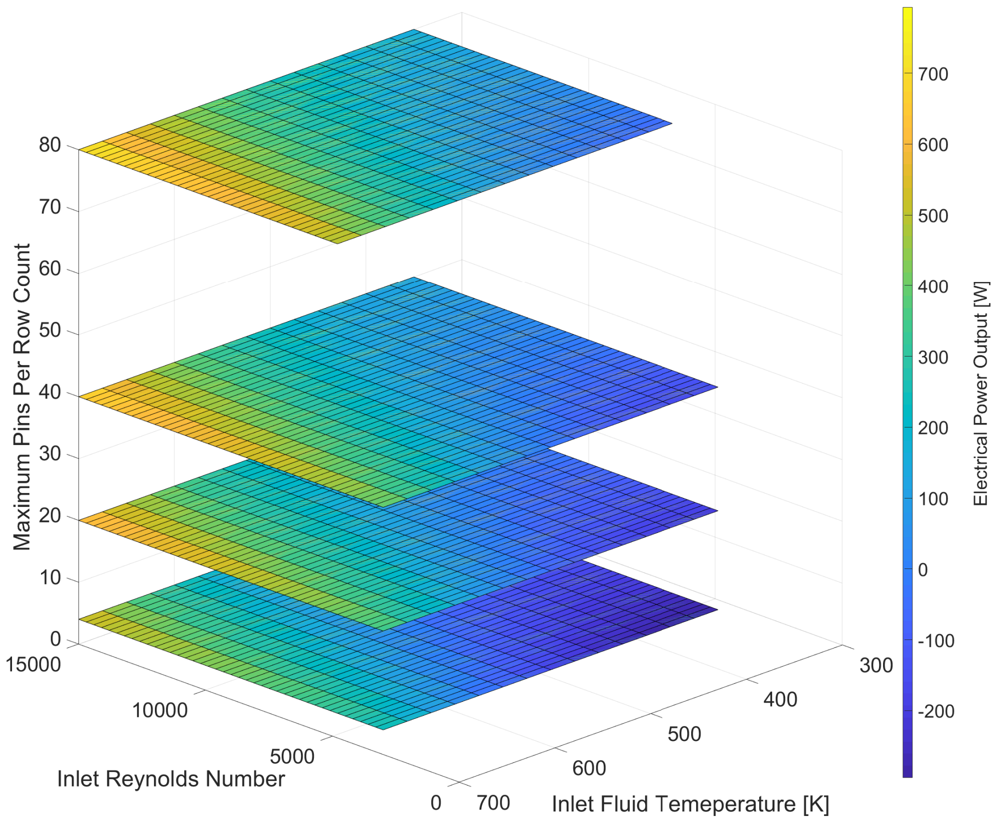

Figure 3.47: Electrical power output vs inlet fluid temperature and Reynolds number

3.5.1.2 Thermal Conversion Efficiency The model estimates for the thermal conversion efficiency in Section 3.4.1.2 were not sufficient to determine an acceptable model fit. As a result, the model form used for the thermal conversion efficiency as a function of inlet fluid temperature and Reynolds number is in the form of a summation of power functions and an intercept term. The conversion efficiency as a function of maximum pin per row count remains a second order polynomial fit. The model is given as follows:

$$f(T_{\infty,h}, \mathrm{Re}, M_{max}) = K_1 + K_2(T_{\infty,h})^{K_3} + K_4(\mathrm{Re})^{K_5} + K_6(M_{max}) + K_7(M_{max})^2 \qquad (3.15)$$

Initial coefficient estimates were taken to be unity and are defined by the vector $\boldsymbol{K}$ given as:

$$\boldsymbol{K} = [1, 1, 1, 1, 1, 1, 1]$$

Convergence of a solution using this model fit was obtained with the function being given as:

$$\eta_{th} = -1.881 + (2.064 \cdot 10^{-3})(T_{\infty,h})^{0.737} + (6.316 \cdot 10^{-5})(\mathrm{Re})^{1.799} - 0.035(M_{max}) + (7.480 \cdot 10^{-5}(M_{max})^2 \in \mathbb{A}_1 \tag{3.16}$$

$$\begin{bmatrix} 3,000 \leq \mathrm{Re} \leq 15,000 \\ 350 \leq T_\infty\,[\mathrm{K}] \leq 700 \\ 4 \leq M_{max} \leq 100 \end{bmatrix}$$

The model's adjusted R^2, RMSE, maximum value and minimum value are tabulated in table 3.36.

Figure 3.48 shows three view points of a heat-map scatter plot of the raw data for conversion efficiency versus inlet fluid temperature, inlet Reynolds number and maximum pin per row count. It is evident the conversion efficiency converges to a maximum at the corner where the inlet fluid temperature and Reynolds number continue to increase towards their respective maximum and the maximum pin per row count is approximately between 10 and 70.

Figure 3.49 is a heat-map plot representing the function given by Eq. 3.16. The trends of the model fit appear to be reflective of the raw data with some exceptions. Higher conversion efficiency occurs at the upper extremes of inlet fluid temperature and Reynolds number and the lower extremes of maximum pin per row count. A region of relative maximum values also appears to be concentrated in the sector where inlet fluid temperature is at the maximum value of 700 [K] while inlet Reynolds number varies and maximum pin per row count is between 10 and 30; thus, reinforcing the assertion that inlet fluid temperature has the most significant influence on power output. Deviation between the numeric values of the maximum and minimum conversion efficiency is relatively minimal compared to the electrical power output discussed in Section 3.5.1.1. The conversion efficiency from the raw data has a maximum and minimum value of approximately 9 % and 0 % respectively while the model fit has a maximum and minimum value of approximately 8.5 % and -0.5 % respectively. This yields a 5.5 % relative difference between maximum values and 0.5 % absolute difference between the minimum values on a scale ranging from -0.5 % to 9 %.

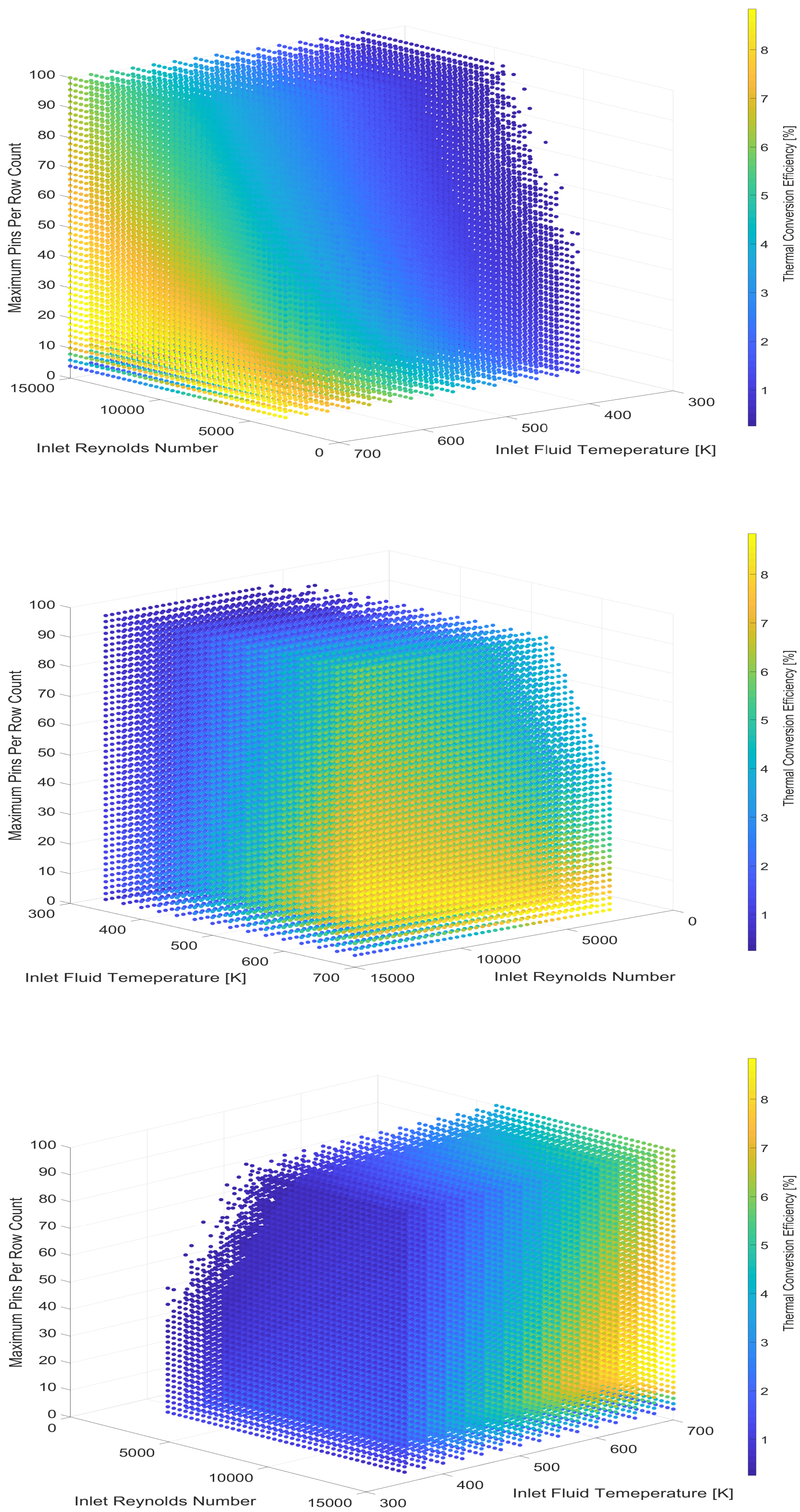

Figure 3.48: Scatter plots of thermal conversion efficiency in domain $\mathbb{A}_1$

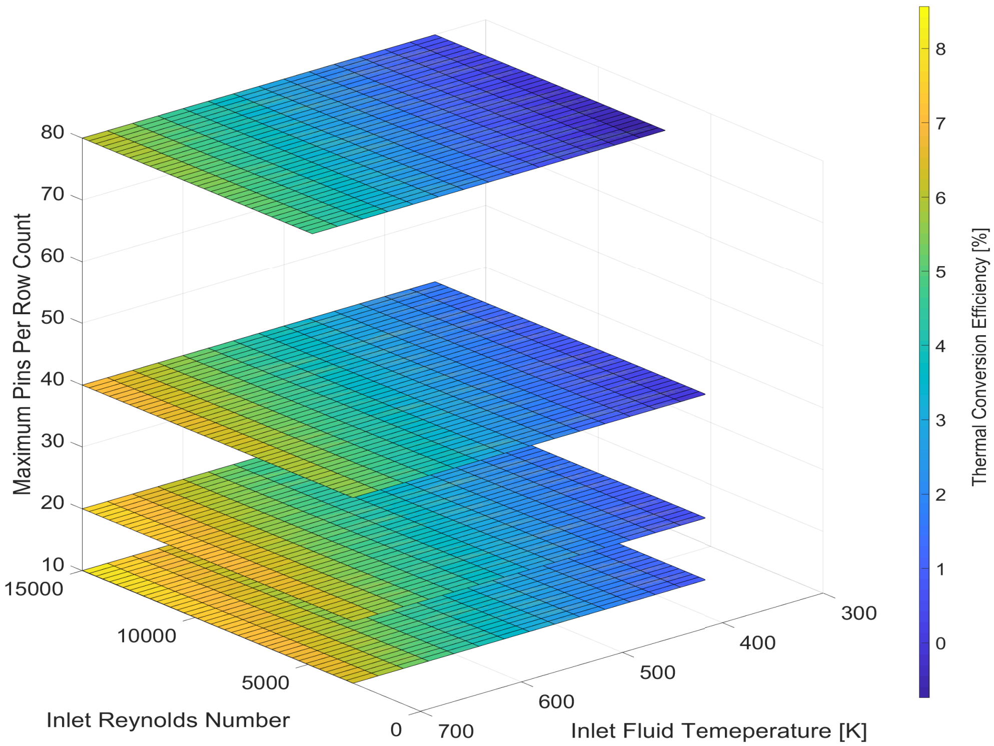

Figure 3.49: Thermal conversion efficiency vs inlet fluid temperature and Reynolds number

3.5.1.3 Performance Index The initial estimates for the performance index uses a model form given as follows:

$$f(T_{\infty,h}, \mathrm{Re}, M_{max}) = K_1 + K_2(T_{\infty,h}) + K_3(T_{\infty,h})^2 + K_4(\mathrm{Re}) + K_5(\mathrm{Re})^2 + K_6(M_{max})^{K_7} \quad (3.17)$$

Initial estimates are given by the vector $\boldsymbol{K}$ defined as:

$$\boldsymbol{K} = [1060.938, 0.727, -4.764 \cdot 10^{-4}, -0.159, 5.549 \cdot 10^{-6}, 1.777 \cdot 10^{-3}]$$

Convergence of a solution using this model fit was obtained with the function being given as:

$$\zeta = -23.934 + (16.959 \cdot 10^{-3})(T_{\infty,h}) + (4.058 \cdot 10^{-7})(T_{\infty,h})^2 +$$
$$(0.511)(\mathrm{Re}) - (2.334 \cdot 10^{-4})(\mathrm{Re})^2 - (313.885)(M_{max})^{-5{,}683.822} \in \mathbb{A}_1 \quad (3.18)$$
$$\begin{bmatrix} 3{,}000 \leq \mathrm{Re} \leq 15{,}000 \\ 350 \leq T_{\infty}\,[\mathrm{K}] \leq 700 \\ 4 \leq M_{max} \leq 100 \end{bmatrix}$$

The model's adjusted R^2, RMSE, maximum value and minimum value are tabulated in table 3.36.

Figure 3.50 shows three view points of a heat-map scatter plot of the performance index versus inlet fluid temperature, inlet Reynolds number and maximum pin per row count. It is evident the performance index converges to a maximum at the corner where the inlet fluid temperature and maximum pin per row count continue to increase towards their maximum respective values and inlet fluid Reynolds number decreases towards it minimum value. Every other section of the plot shows the performance index occurring at low values.

Figure 3.51 is a heat-map plot representing the function given by Eq. 3.18. The trends of the model fit appear to be reflective of the raw data with some exceptions. A higher performance index occurs at the upper extremes of inlet fluid temperature and maximum pin per row count and the lower extremes of the fluid Reynolds number. Deviation between the numeric values of the maximum and minimum performance index is substantial between the model fit and raw data. The performance index from the raw data has a maximum and minimum value of approximately 550 and 0 respectively while the model fit has a maximum and minimum value of approximately 170 and -25 respectively. This yields a 70.91 % relative difference between maximum values and an absolute difference of 25 between the minimum values on a scale ranging from -25 to 550.

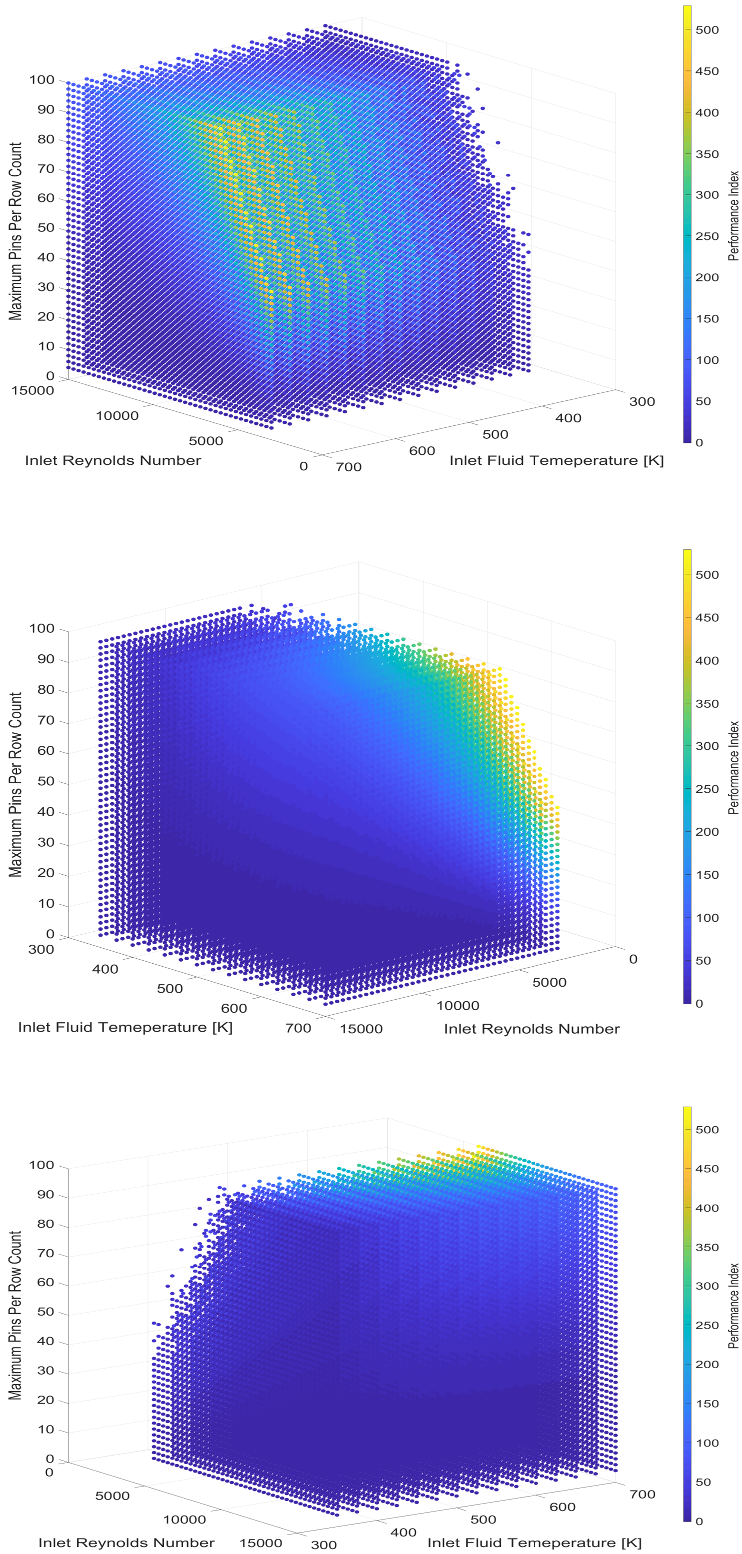

Figure 3.50: Scatter plots of performance index in domain $\mathbb{A}_1$

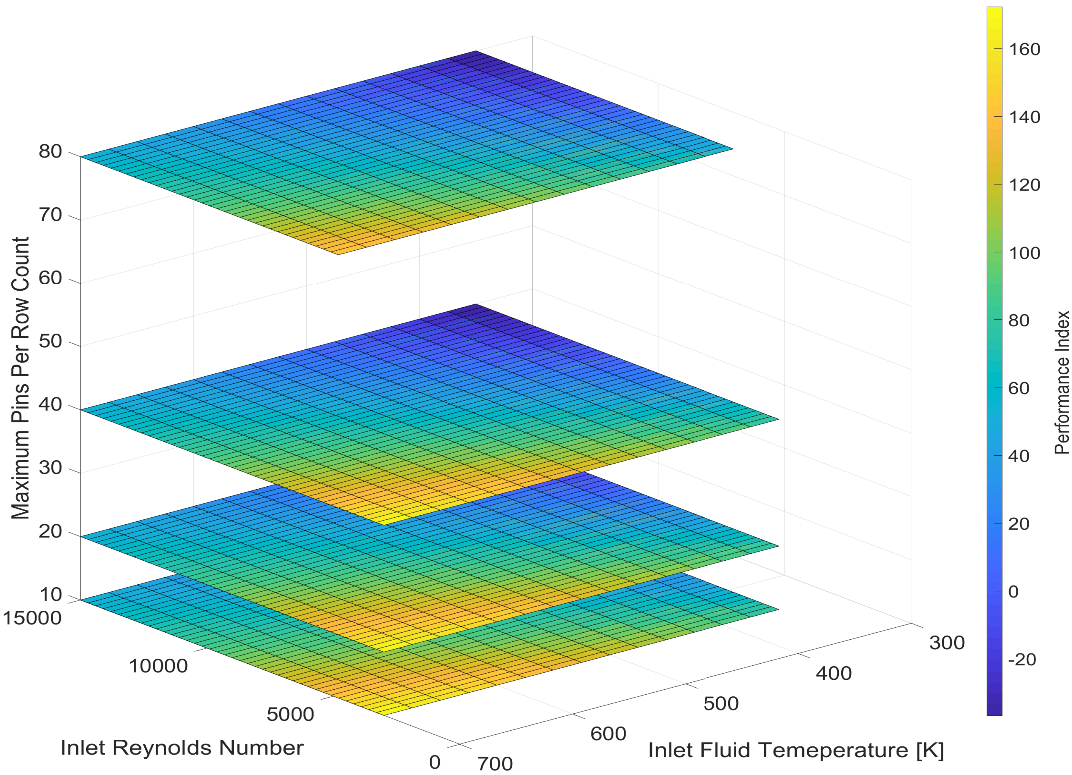

Figure 3.51: Performance index vs inlet fluid temperature and Reynolds number

Table 3.36: Regression analysis results for model fits of equations in set $\mathbb{Z}_1$

Set $\mathbb{Z}_1$ Statistical Values				
Function	R^2_{adj}	RMSE	Max Value	Min Value
P_o	0.838	96.912 [W]	1,248.338 [W]	1.527 [W]
η_{th}	0.913	0.619 [%]	8.841 [%]	0.259 [%]
ζ	0.303	65.832	528.913	-0.991

3.5.2 Equation Set $\mathbb{Z}_2$

The equations of set $\mathbb{Z}_2$ are defined in domain $\mathbb{A}_2$, a domain defining seven independent variables that allow for the thermal conversion efficiency to achieve its maximum value based on the data from the parametric study. The independent variables for the equations of set $\mathbb{Z}_2$ are inlet fluid temperature, thermoelectric material length and pin diameter. The inlet fluid temperature is measured in [K] while the remaining aforementioned variables are measured in [mm].

3.5.2.1 Electrical Power Output The models determined in Section 3.4.2.1 were not sufficient to determine an acceptable model fit. As a result, the model form used for the thermal conversion efficiency is in the form of a summation of power functions and an intercept term. The model is given as follows:

$$f(T_{\infty,h}, t_{N,P}, D_{pin}) = K_1 + K_2(T_{\infty,h})^{K_3} + K_4(t_{N,P})^{K_5} + K_6(D_{pin})^{K_7} \tag{3.19}$$

Initial coefficient estimates were taken to be unity and are defined by the vector $\boldsymbol{K}$ given as:

$$\boldsymbol{K} = [1, 1, 1, 1, 1, 1, 1]$$

Convergence of a solution using this model fit was obtained with the function being given as:

$$P_o = 0.911 + (2.938 \cdot 10^{-10})(T_{\infty,h})^{4.225} + 0.803(t_{N,P})^{0.801} + 0.811(D_{pin})^{0.844} \in \mathbb{A}_2 \tag{3.20}$$

$$\begin{bmatrix} 350 \leq T_\infty \,[\text{K}] \leq 700 \\ 0.5 \leq t_{N,P} \,[\text{mm}] \leq 5 \\ 1.5875 \leq D_{pin} \,[\text{mm}] \leq 6.350 \end{bmatrix}$$

The model's adjusted R^2, RMSE, maximum value and minimum value are tabulated in table 3.37.

Figure 3.52 shows three view points of a heat-map scatter plot of the raw data for power output versus inlet fluid temperature, thermoelectric material length and pin diameter. It is evident the power output has a relative maximum region defined where inlet fluid temperature is at 700 [K] and pin diameter as well as thermoelectric material length varies. It has been observed that relative minimum values occur when the inlet fluid temperature approaches its lower values and the numeric values of the pin diameter as well as thermoelectric material length varies.

Figure 3.53 is a heat-map plot representing the function given by Eq. 3.20. The trends of the model fit appear to be reflective of the raw data with some exceptions. A region of relative maximum values appears to be concentrated in the sector where inlet fluid temperature is at the maximum value of 700 [K], and thermoelectric material length as well as pin diameter varies; thus, reinforcing the assertion that inlet fluid temperature has the most significant influence on power output. A moderate deviation between the respective maximum and minimum values of the raw data and the model fit exists. It is evident the scale of the power output from the raw data has a maximum and minimum value of approximately 450 [W] and 0 [W] respectively while the model fit has a maximum and minimum value of 320 [W] and 10 [W] respectively. This yields a 28.889 % relative difference between maximum values and a 10 [W] absolute difference between the minimum values on a scale ranging from 0 [W] to 450 [W].

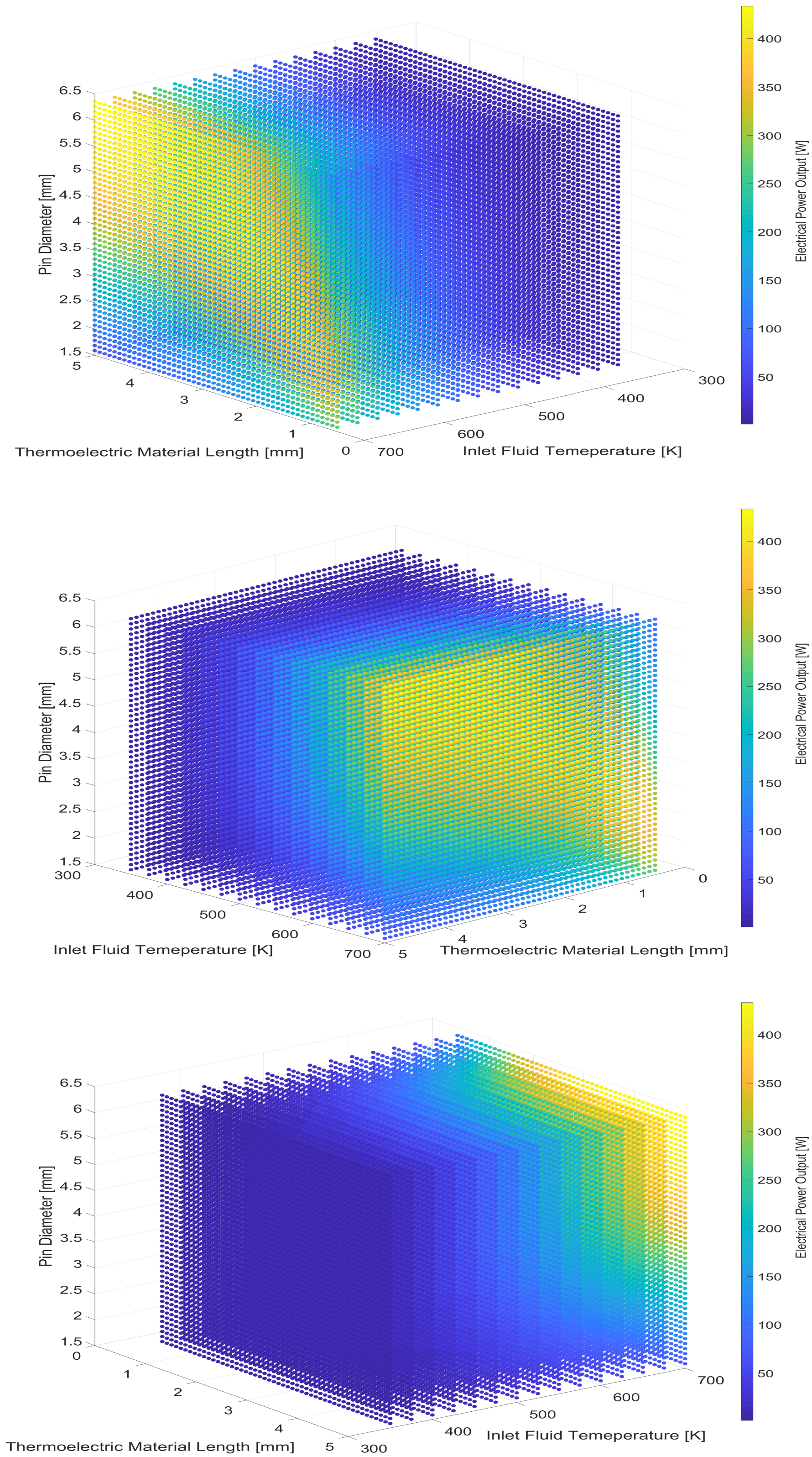

Figure 3.52: Scatter plots of electrical power output in domain $\mathbb{A}_2$

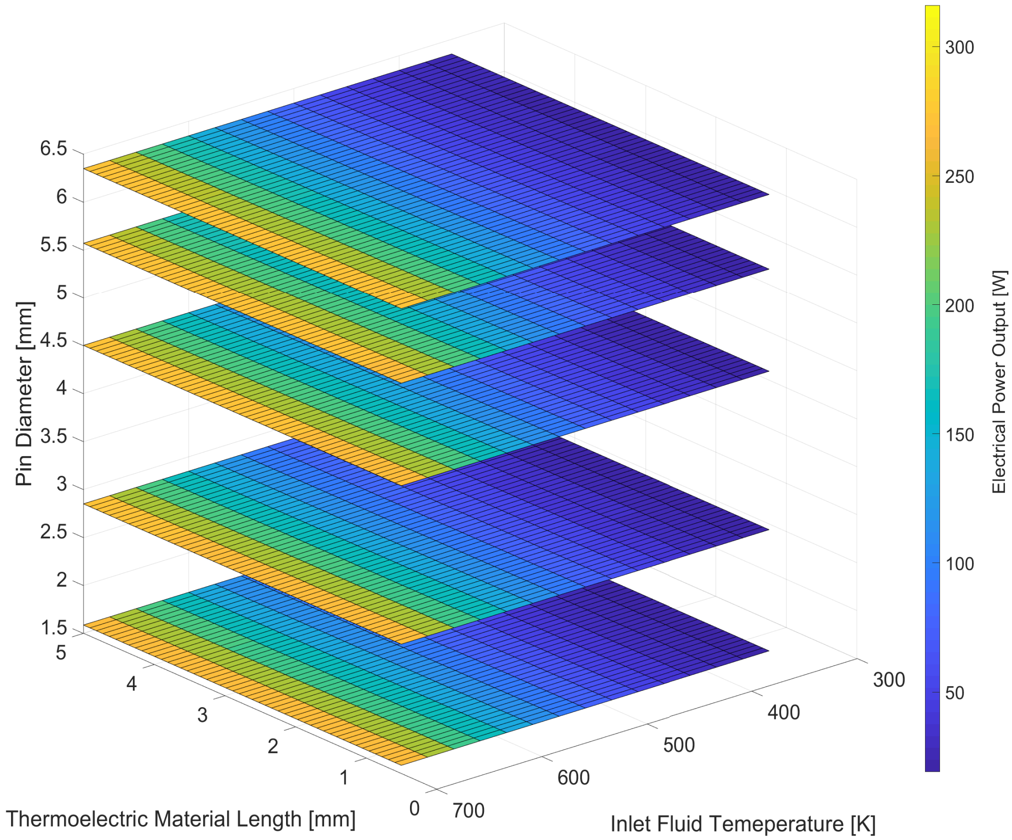

Figure 3.53: Electrical power output vs inlet fluid temperature and thermoelectric material length

3.5.2.2 Thermal Conversion Efficiency The initial estimates for the performance index uses a model form given as follows:

$$f(T_{\infty,h}, t_{N,P}, D_{pin}) = K_1 + K_2\sqrt{T_{\infty,h}} + K_3\frac{\log_{10}(t_{N,P})}{\log_{10}(K_4)} + K_5(D_{pin}) + K_6(D_{pin})^2 \tag{3.21}$$

Initial estimates are given by the vector $\boldsymbol{K}$ defined as:

$$\boldsymbol{K} = [-0.415, 1.184, -0.166, 0.892, -0.465, -0.054]$$

Convergence of a solution using this model fit was obtained with the function being given as:

$$\eta_{th} = -13.972 + 0.809\sqrt{T_{\infty,h}} + 0.646\frac{\log_{10}(t_{N,P})}{\log_{10}(0.793)} + 1.626(D_{pin}) - 0.166(D_{pin})^2 \in \mathbb{A}_2 \tag{3.22}$$

$$\begin{bmatrix} 350 \leq T_\infty \ \text{[K]} \leq 700 \\ 0.5 \leq t_{N,P} \ \text{[mm]} \leq 5 \\ 1.5875 \leq D_{pin} \ \text{[mm]} \leq 6.350 \end{bmatrix}$$

The model's adjusted R^2, RMSE, maximum value and minimum value are tabulated in table 3.37.

Figure 3.54 shows three view points of a heat-map scatter plot of the raw data for conversion efficiency versus inlet fluid temperature, thermoelectric material length and pin diameter. It is evident the conversion efficiency converges to a maximum at the corner where the inlet fluid temperature and thermoelectric material length continue to increase towards their respective maximum values and the pin diameter is approximately between 1.5 [mm] and 4 [mm].

Figure 3.55 is a heat-map plot representing the function given by Eq. 3.22. The trends of the model fit appear to be reflective of the raw data with some exceptions. A region of relative maximum conversion efficiency occurs when the thermoelectric material length exists at its lower numeric values while the inlet fluid temperature can vary between 500 [K] and 700 [K] and the pin diameter varies at any value. A moderate deviation between the respective maximum and minimum values of the raw data and the model fit exists. It is evident the scale of the conversion efficiency from the raw data has a maximum and minimum value of approximately 10.5 % and 0 % respectively while the model fit has a maximum and minimum value of 13.5 % and -0.5 % respectively. This yields a 28.571 % relative difference between maximum values and 0.5 % absolute difference between the minimum values on a scale ranging from -0.5 % to 13.5 %.

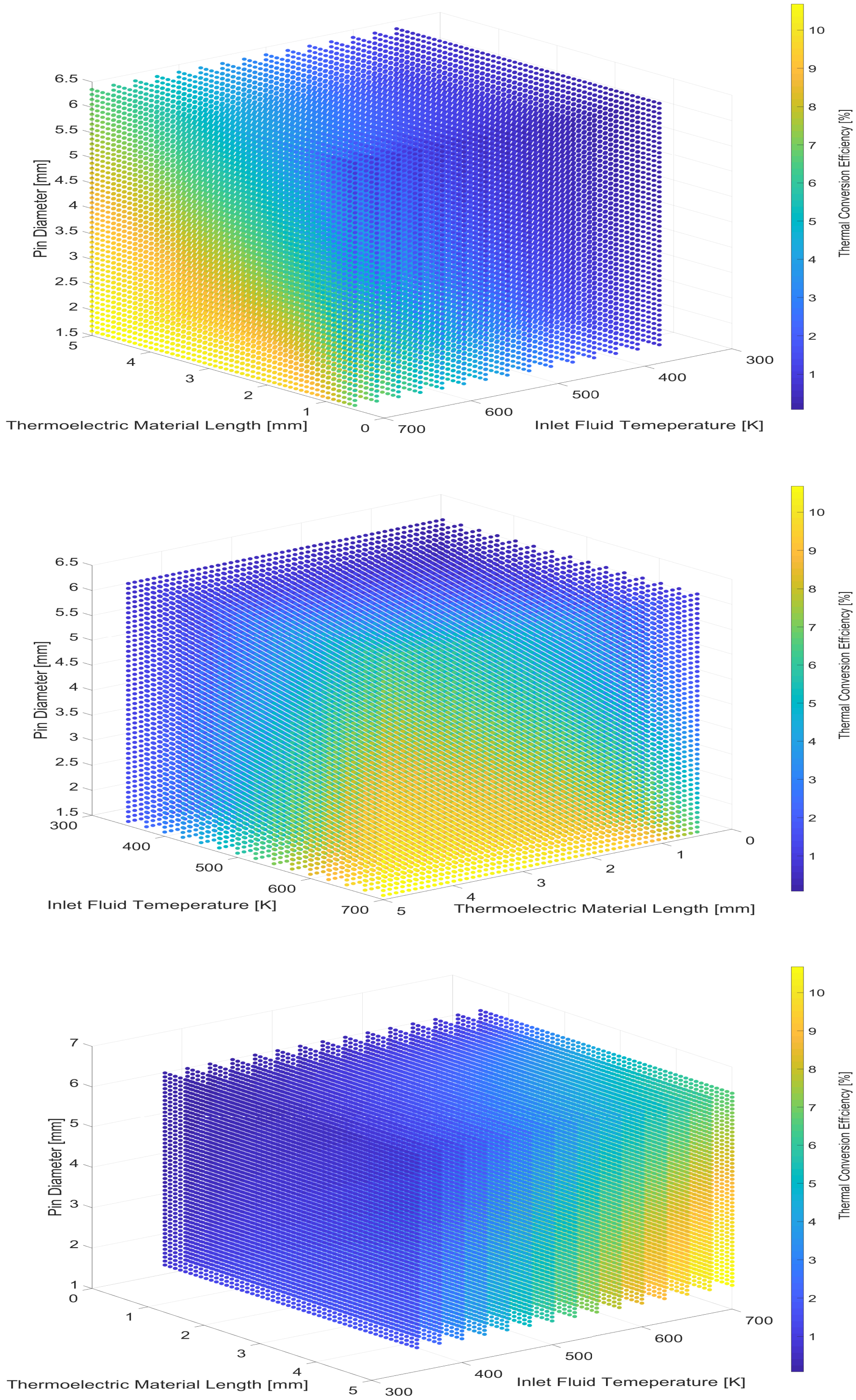

Figure 3.54: Scatter plots of thermal conversion efficiency in domain $\mathbb{A}_2$

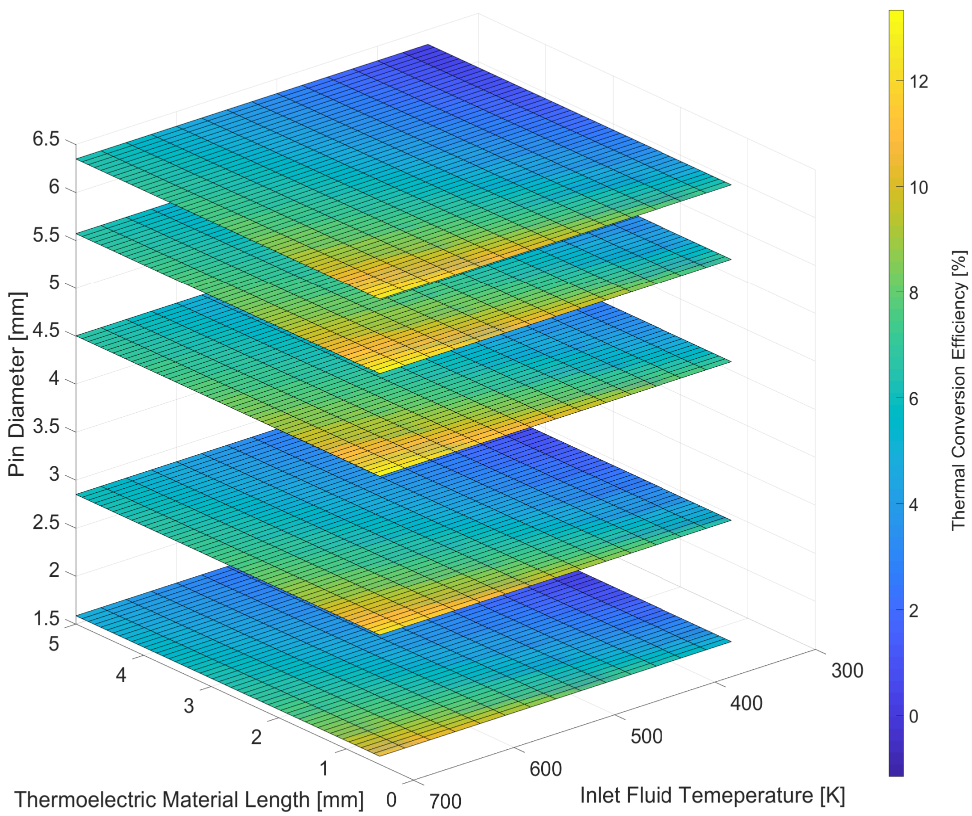

Figure 3.55: Thermal conversion efficiency vs inlet fluid temperature and thermoelectric material length

3.5.2.3 Performance Index The initial estimates for the performance index uses a model form given as follows:

$$f(T_{\infty,h}, t_{N,P}, D_{pin}) = K_1 + K_2(T_{\infty,h}) + K_3(T_{\infty,h})^2 + K_4(t_{N,P})^{K_5} + K_6(D_{pin})^{K_7} \tag{3.23}$$

Initial estimates are given by the vector $\boldsymbol{K}$ defined as:

$$\boldsymbol{K} = [-142.369, 0.181, -1.617 \cdot 10^{-4}, 10.330, -0.184, 8.694, 2.728]$$

Convergence of a solution using this model fit was obtained with the function being given as:

$$\begin{aligned} \zeta = -18,598.384 + 4.329(T_{\infty,h}) + (3.113 \cdot 10^{-3})(T_{\infty,h})^2 + \\ 49.018(t_{N,P})^{1.569} + 17,053.212(D_{pin})^{0.004} \in \mathbb{A}_2 \end{aligned} \tag{3.24}$$

$$\begin{bmatrix} 350 \leq T_{\infty}\,[\mathrm{K}] \leq 700 \\ 0.5 \leq t_{N,P}\,[\mathrm{mm}] \leq 5 \\ 1.5875 \leq D_{pin}\,[\mathrm{mm}] \leq 6.350 \end{bmatrix}$$

The model's adjusted R^2, RMSE, maximum value and minimum value are tabulated in table 3.37.

Figure 3.56 shows three view points of a heat-map scatter plot of the performance index versus inlet fluid temperature, thermoelectric length and pin diameter. It is evident the performance index converges to a maximum at the corner where the inlet fluid temperature and thermoelectric material length continue to increase towards their respective maximum values and pin diameter exists between approximately 5.5 [mm] and 6.5 [mm]. Every other section of the plot shows the performance index occurring at relative minimum values.

Figure 3.57 is a heat-map plot representing the function given by Eq. 3.24. The trends of the model fit appear to be reflective of the raw data with some exceptions. A region of relative maximum performance index occurs when the thermoelectric material length exists at its upper numeric values while the inlet fluid temperature can vary between 400 [K] and 700 [K] and the pin diameter varies at any value. A substantial deviation between the respective maximum and minimum values of the raw data and the model fit exists. The performance index from the raw data has a maximum and minimum value of approximately 1,300 and 0 respectively while the model fit has a maximum and minimum value of approximately 700 and -350 respectively. This yields a 46.2% relative difference between maximum values and -350 absolute difference between the minimum values on a scale ranging from -350 to 1,300.

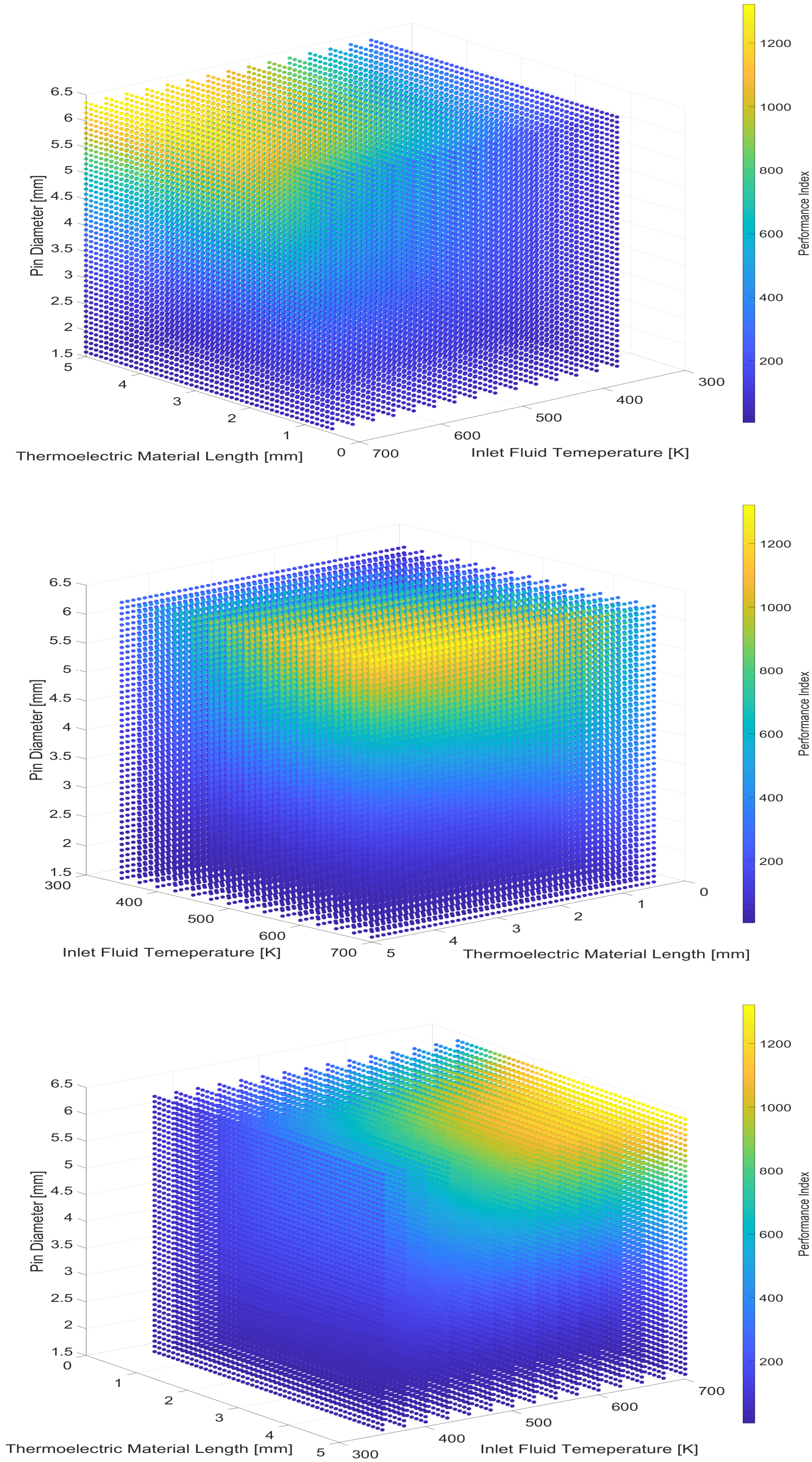

Figure 3.56: Scatter plots of performance index in domain $\mathbb{A}_2$

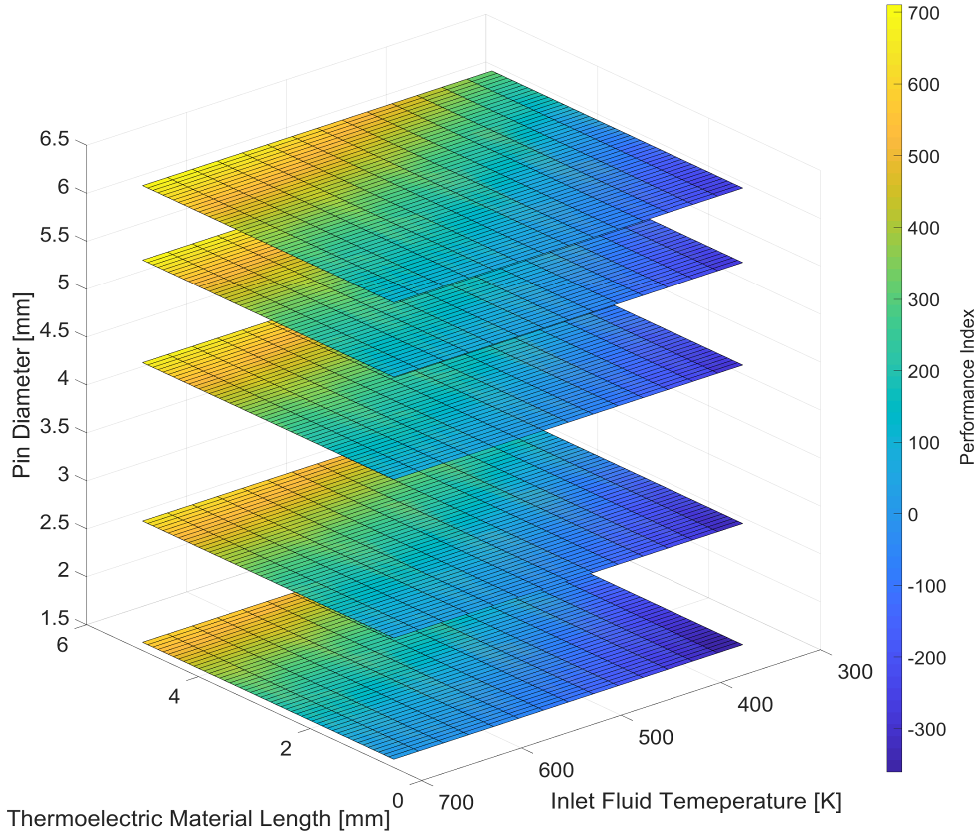

Figure 3.57: Performance index vs inlet fluid temperature and thermoelectric material length

Table 3.37: Regression analysis results for model fits of equations in set $\mathbb{Z}_2$

Set $\mathbb{Z}_2$ Statistical Values				
Function	R^2_{adj}	RMSE	Max Value	Min Value
P_o [W]	0.825	45.397	433.445	0.996
η_{th} [%]	0.926	0.687	10.677	0.072
ζ [-]	0.821	124.908	1,322.157	5.054

3.5.3 Equation Set $\mathbb{Z}_3$

The equations of set $\mathbb{Z}_3$ are defined in domain $\mathbb{A}_3$, a domain defining seven independent variables that allow for the performance index to achieve its maximum value based on the data from the parametric study. The independent variables for the equations of set $\mathbb{Z}_3$ are maximum pin per row count, pin diameter and inlet Reynolds number. The pin diameter is measured in [mm] while the remaining aforementioned variables are unit-less.

3.5.3.1 Electrical Power Output The models determined in Section 3.4.3.1 were not sufficient to determine an acceptable model fit. As a result, the model form used for the thermal conversion efficiency is in the form of a summation of power functions and an intercept term. The model is given as follows:

$$f(M_{max}, D_{pin}, \mathrm{Re}) = K_1 + K_2(M_{max})^{K_3} + K_4(D_{pin})^{K_5} + K_6(\mathrm{Re})^{K_7} \tag{3.25}$$

Initial coefficient estimates were taken to be unity and are defined by the vector $\boldsymbol{K}$ given as:

$$\boldsymbol{K} = [1, 1, 1, 1, 1, 1, 1]$$

Convergence of a solution using this model fit was obtained with the function being given as:

$$P_o = -134.013 + 11.526(T_{\infty,h})^{0.694} + 108.534(t_{N,P})^{-371.718} - 1.362(D_{pin})^{-0.149} \in \mathbb{A}_3 \tag{3.26}$$

$$\begin{bmatrix} 4 \leq M_{max} \leq 100 \\ 1.5875 \leq D_{pin}\,[\mathrm{mm}] \leq 6.350 \\ 3,000 \leq \mathrm{Re} \leq 15,000 \end{bmatrix}$$

The model's adjusted R^2, RMSE, maximum value and minimum value are tabulated in table 3.38.

Figure 3.58 shows three view points of a heat-map scatter plot of the raw data for power output versus maximum pin per row count, pin diameter and inlet Reynolds number. It is evident the power output converges to a maximum at the corner where the maximum pin per row count, pin diameter and inlet fluid Reynolds number increase towards their maximum respective values. The remaining volume of the plots represents a region of relative minimum values. Some data points are missing in the bottom triangular region of the cube where inlet Reynolds number is closer to is lower values, maximum pin per row count does not exceed approximately 60 and pin diameter varies. This most likely is due to the lack of empirical data needed to define fluid Reynolds number given the influence increased pin count has on it. This data is necessary to continue solving the solution algorithm defined in Section 2.2. As a result, data for conversion efficiency and performance index in Section 3.5.3.2 - 3.5.3.3 will not exist at the same points.

Figure 3.59 is a heat-map plot representing the function given by Eq. 3.26. The trends of the model fit appear to be reflective of the raw data with some exceptions. A region of relative maximum values appears to be concentrated in the sector where inlet fluid temperature is at the maximum value of 700 [K], and thermoelectric material length as well as pin diameter varies; thus, reinforcing the assertion that inlet fluid temperature has the most significant influence on power output. A moderate deviation between the respective maximum and minimum values of the raw data and the model fit exists. It is evident the scale of the power output from the raw data has a maximum and minimum value of approximately 450 [W] and 0 [W] respectively while the model fit has a maximum and minimum value of 320 [W] and 10 [W] respectively. This yields a 28.9% relative difference between maximum values and a 10 [W] absolute difference between the minimum values on a scale ranging from 0 [W] to 450 [W].

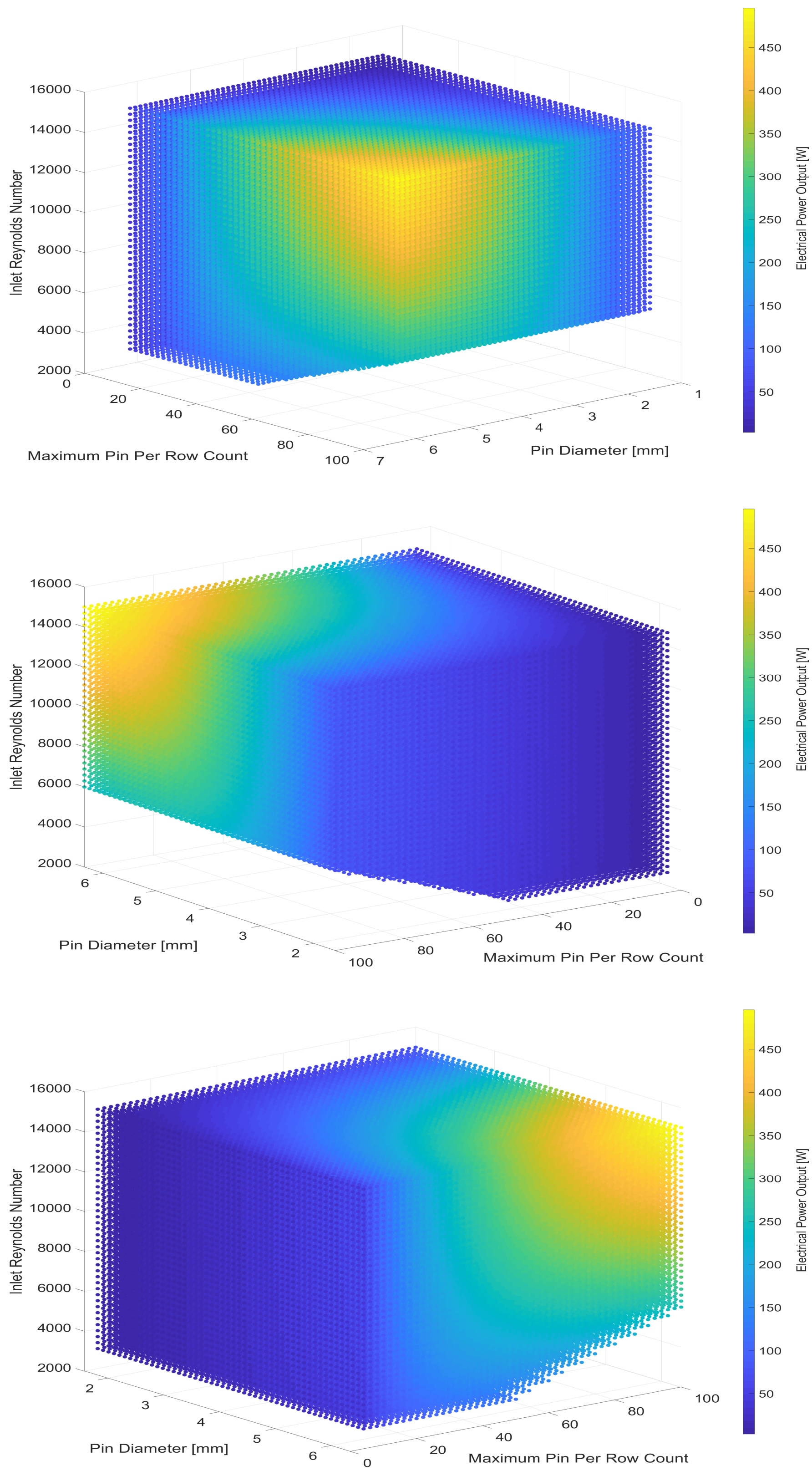

Figure 3.58: Scatter plots of electrical power output in domain $\mathbb{A}_3$

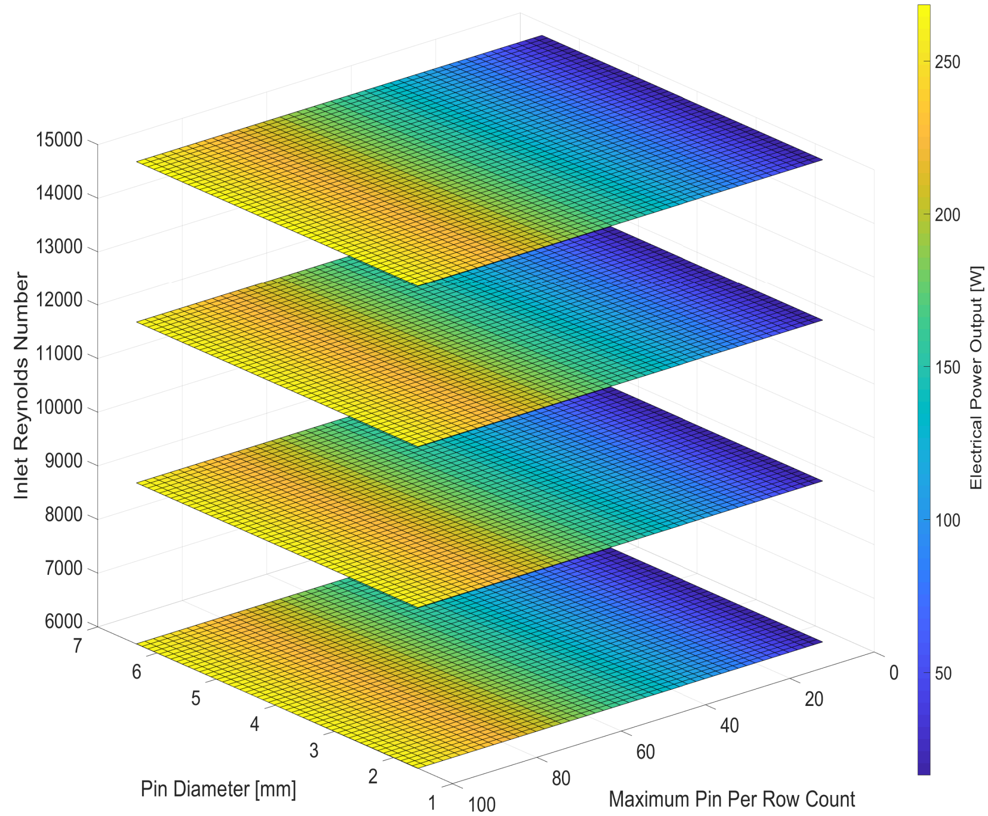

Figure 3.59: Electrical power output vs maximum pin per row count and pin diameter

3.5.3.2 Thermal Conversion Efficiency The initial estimates for the thermal conversion efficiency uses a model form given as follows:

$$f(M_{max}, D_{pin}, \mathrm{Re}) = K_1 + K_2\sqrt{M_{max}} + K_3(D_{pin}) + K_4(D_{pin})^2 + K_5\frac{\log_{10}(\mathrm{Re})}{\log_{10}(K_6)} \tag{3.27}$$

Initial estimates are given by the vector $\boldsymbol{K}$ defined as:

$$\boldsymbol{K} = [-0.415, 1.184, -0.166, 0.892, -0.465, -0.054]$$

Convergence of a solution using this model fit was obtained with the function being given as:

$$\eta_{th} = 6.133 + 0.040\sqrt{M_{max}} + 0.674(D_{pin}) + -0.142(D_{pin})^2 + 1.134\frac{\log_{10}(\mathrm{Re})}{\log_{10}(73.205)} \in \mathbb{A}_3 \tag{3.28}$$

$$\begin{bmatrix} 4 \leq M_{max} \leq 100 \\ 1.5875 \leq D_{pin}\,[\text{mm}] \leq 6.350 \\ 3,000 \leq \text{Re} \leq 15,000 \end{bmatrix}$$

The model's adjusted R^2, RMSE, maximum value and minimum value are tabulated in table 3.38.

Figure 3.60 shows three view points of a heat-map scatter plot of the raw data for conversion efficiency versus maximum pin per row count, pin diameter and inlet Reynolds number. It is evident the conversion efficiency exists at its maximum at a substantially large region of space defined in the scatter plot of raw data. This region appears to be defined by an increasing maximum pin per row count, pin diameter and inlet fluid Reynolds number by a linear rate. It appears relative minimum values exist when one independent value increases at a faster rate than the other two. This is evident when conversion efficiency decreases drastically when inlet Reynolds number increases and maximum pin per row count as well as pin diameter do not. This region of relative minimum also exists when maximum pin per row count increases and inlet Reynolds number as well as pin diameter do not.

Figure 3.61 is a heat-map plot representing the function given by Eq. 3.28. The trends of the model fit appear to be reflective of the raw data with some exceptions. A region of relative maximum conversion efficiency is defined when pin diameter is approximately lower than 4 [mm] and inlet Reynolds number as well as maximum pin per row count varies. A substantial deviation between the respective maximum and minimum values of the raw data and the model fit exists. It is evident the scale of the conversion efficiency from the raw data has a maximum and minimum value of approximately 10.5% and 0% respectively while the model fit has a maximum and minimum value of 10% and 7% respectively. This yields a 4.761% relative difference between maximum values and 7% absolute difference between the minimum values on a scale ranging from 0 % to 10.5%.

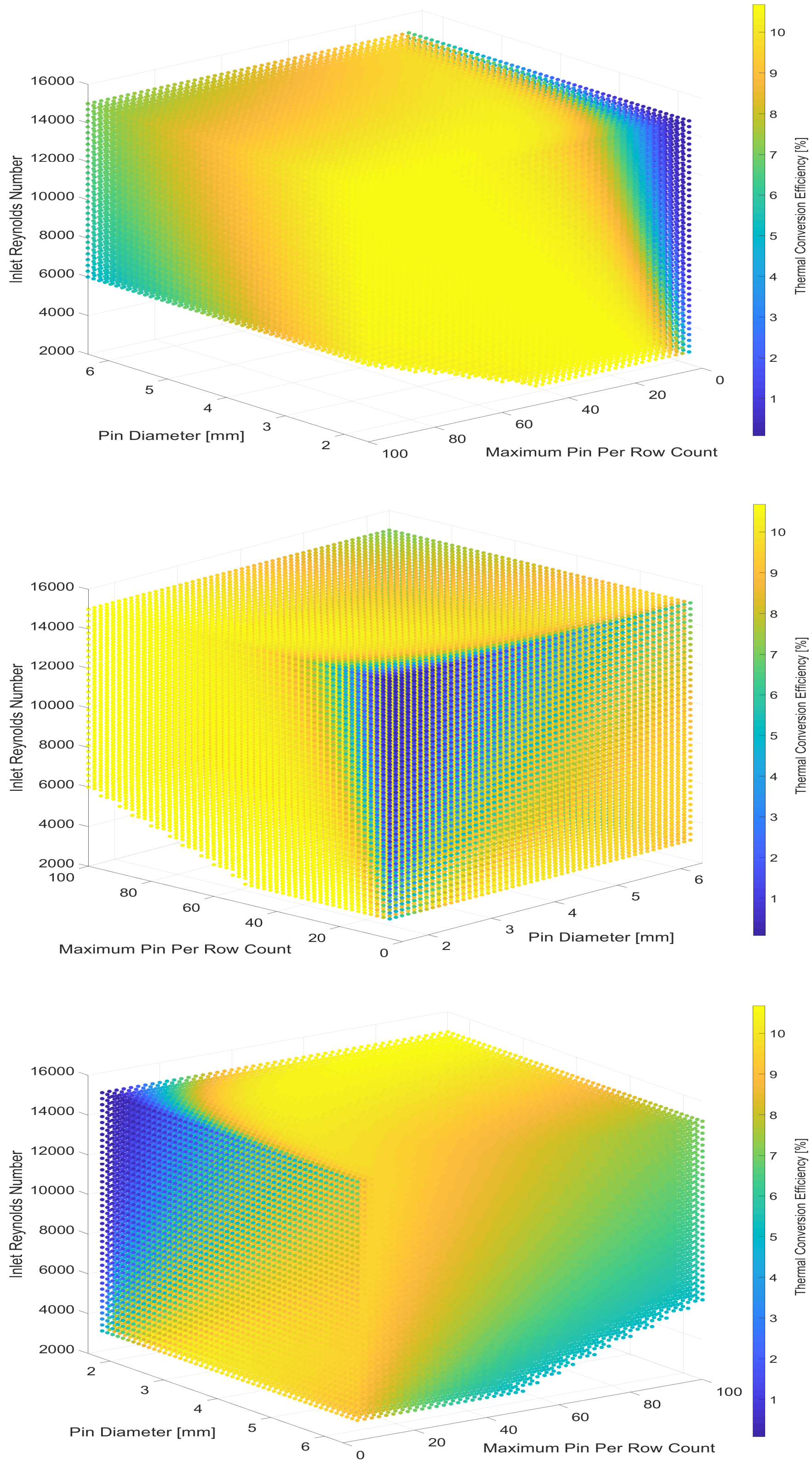

Figure 3.60: Scatter plots of thermal conversion efficiency in domain $\mathbb{A}_3$

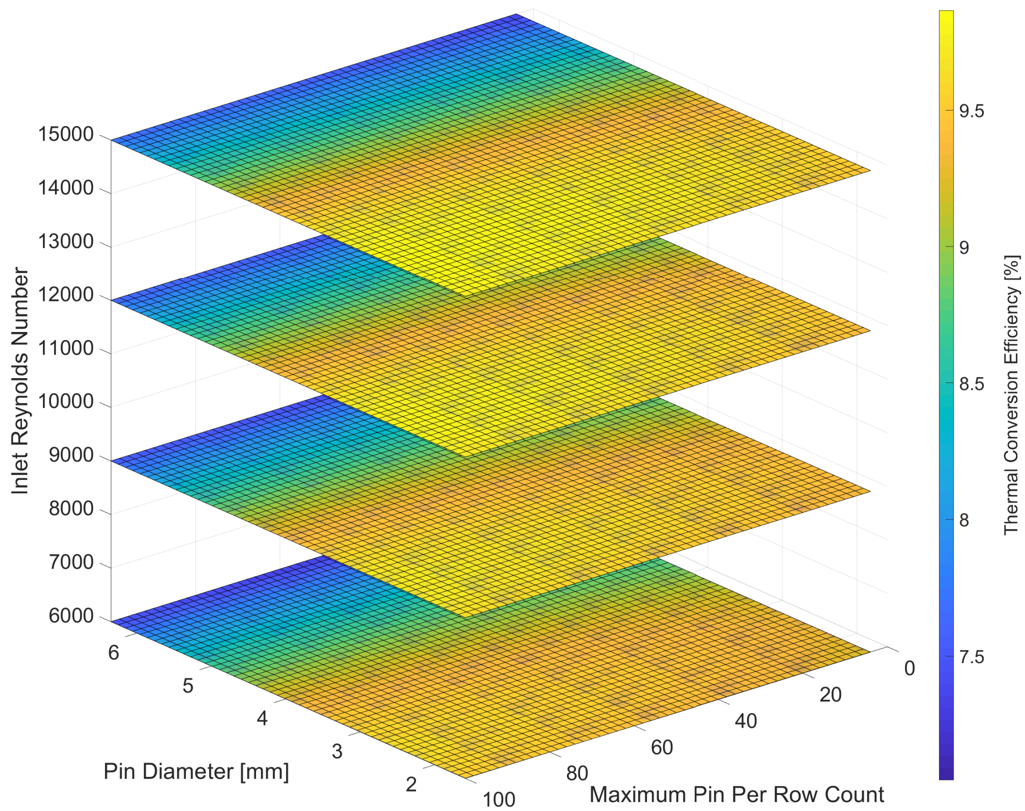

Figure 3.61: Thermal conversion efficiency vs maximum pin per row count and pin diameter

3.5.3.3 Performance Index The initial estimates for the performance index uses a model form given as follows:

$$f(M_{max}, D_{pin}, \mathrm{Re}) = K_1 + K_2(M_{max})^{K_3} + K_4(D_{pin}) + K_5(D_{pin})^2 + K_6(\mathrm{Re})^{K_7} \tag{3.29}$$

Initial estimates are given by the vector $\boldsymbol{K}$ defined as:

$$\boldsymbol{K} = [-142.369, 0.181, -1.617 \cdot 10^{-4}, 10.330, -0.184, 8.694, 2.728]$$

Convergence of a solution using this model fit was obtained with the function being given as:

$$\begin{aligned} \zeta = 1,653.634 + 2.674(M_{max})^{1.285} + 22.273(D_{pin}) + \\ 1.000(D_{pin})^2 - 150.539(\mathrm{Re})^{0.297} \in \mathbb{A}_3 \end{aligned} \tag{3.30}$$

$$\begin{bmatrix} 4 \leq M_{max} \leq 100 \\ 1.5875 \leq D_{pin}, [\mathrm{mm}] \leq 6.350 \\ 3,000 \leq \mathrm{Re} \leq 15,000 \end{bmatrix}$$

The model's adjusted R^2, RMSE, maximum value and minimum value are tabulated in table 3.38.

Figure 3.62 shows three view points of a heat-map scatter plot of the performance index versus maximum pin per row count, pin diameter and inlet fluid Reynolds number. It is evident the performance index converges to a maximum at the corner where the pin diameter and maximum pin per row count continue to increase towards their maximum respective values and the inlet fluid Reynolds number exists between approximately 3000 and 6000. Every other section of the plot shows the performance index occurring at low values.

Figure 3.63 is a heat-map plot representing the function given by Eq. 3.30. The trends of the model fit appear to be reflective of the raw data with some exceptions. A region of relative maximum performance index occurs when the pin diameter and maximum pin per count increase towards their respective maximum values and inlet Reynolds number decreases towards its lower numeric values. A substantial deviation between the respective maximum and minimum values of the raw data and the model fit exists. The performance index from the raw data has a maximum and minimum value of approximately 5500 and 0 respectively while the model fit has a maximum and minimum value of approximately 1600 and -700 respectively. This yields a 70.909 % relative difference between maximum values and 700 absolute difference between the minimum values on a scale ranging from -700 to 5500.

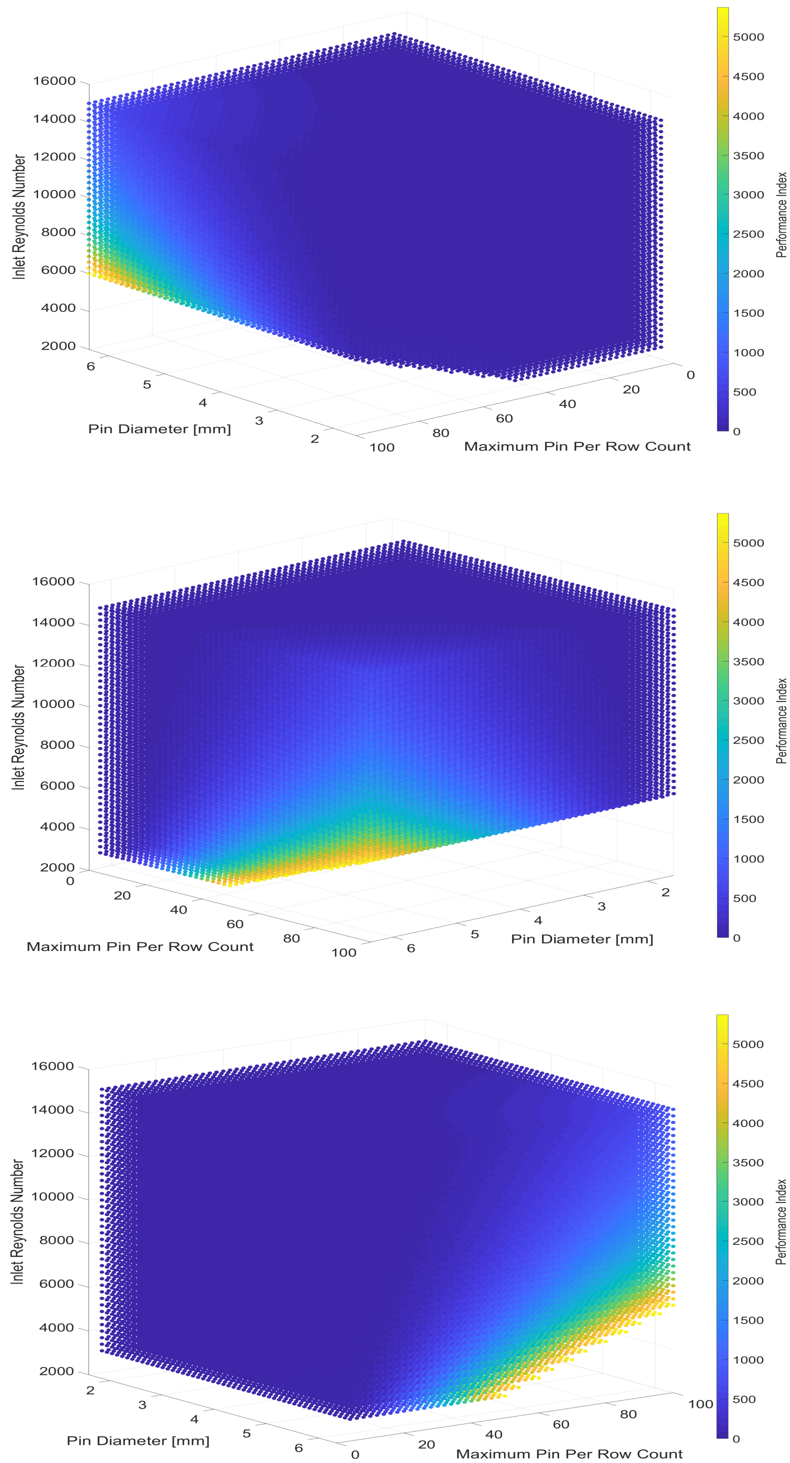

Figure 3.62: Scatter plots of performance index in domain $\mathbb{A}_3$

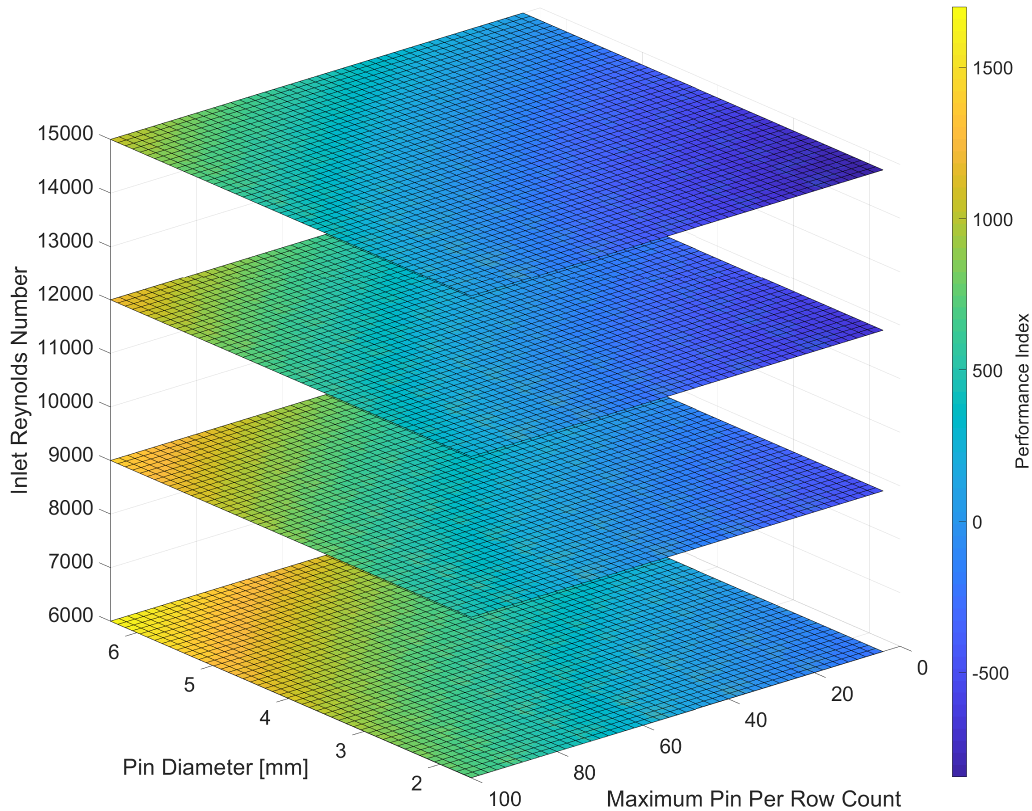

Figure 3.63: Performance index vs maximum pin per row count and pin diameter

Table 3.38: Regression analysis results for model fits of equations in set $\mathbb{Z}_3$

Set $\mathbb{Z}_3$ Statistical Values				
Function	R^2_{adj}	RMSE	Max Value	Min Value
P_o	0.468	75.256 [W]	495.590 [W]	2.705 [W]
η_{th}	0.205	1.385 [%]	10.667 [%]	0.084 [%]
ζ	0.524	434.726 [-]	5,369.988 [-]	-0.999 [-]

3.6 Conclusions

A comprehensive approach composed of a parametric study and non-linear regression was conducted. The parametric study was used to determine the maximum values of performance solutions in a 42,000,000 configuration design space while the non-linear regression analysis was used to determine the linear and non-linear relationship between a set of independent variables and performance solutions based on configurations of the maximum values thereof. The key findings from the parametric study and linear regression analysis include the following:

1. The electrical power output has a maximum value of 1248.338 [W] and is most effectively influenced by inlet fluid temperature, inlet fluid Reynolds number and maximum pin per row count respectively.
2. The thermal conversion efficiency has a maximum value of 10.677 % and is most effectively influenced by inlet fluid temperature, thermoelectric material length and pin diameter respectively.
3. The performance index has a maximum value of 5259.130 and is most effectively influenced by maximum pin per row count, pin diameter and inlet fluid Reynolds number.

The key findings of the non-linear regression analysis are the non-linear relationships given by equations 3.31a - 3.33c.

$$\mathbb{Z}_1 = \begin{cases} \boldsymbol{P_o} = -31608.166 - 3.489(T_{\infty,h}) + (5.022 \cdot 10^{-3})(T_{\infty,h})^2 + \\ 4.108\sqrt{\mathrm{Re}} + 31609.012(M_{max})^{0.002} \in \mathbb{A}_1 & (3.31\text{a}) \\ \boldsymbol{\eta_{th}} = -1.881 + (2.064 \cdot 10^{-3})(T_{\infty,h})^{0.737} + (6.316 \cdot 10^{-5})(\mathrm{Re})^{1.799} - \\ M_{max}) + (7.480 \cdot 10^{-5}(M_{max})^2 \in \mathbb{A}_1 & (3.31\text{b}) \\ \boldsymbol{\zeta} = -23.934 + (16.959 \cdot 10^{-3})(T_{\infty,h}) + (4.058 \cdot 10^{-7})(T_{\infty,h})^2 + \\ (0.511)(\mathrm{Re}) - (2.334 \cdot 10^{-4})(\mathrm{Re})^2 - (313.885)(M_{max})^{-5683.822} \in \mathbb{A}_1 & (3.31\text{c}) \end{cases}$$

$$\begin{bmatrix} 3,000 \leq \mathrm{Re} \leq 15,000 \\ 350 \leq T_\infty\,[\mathrm{K}] \leq 700 \\ 4 \leq M_{max} \leq 100 \end{bmatrix}$$

$$\mathbb{Z}_2 = \begin{cases} \boldsymbol{P_o} = 0.911 + (2.938 \cdot 10^{-10})(T_{\infty,h})^{4.225} + 0.803(t_{N,P})^{0.801} + 0.811(D_{pin})^{0.844} \in \mathbb{A}_2 & (3.32a) \\ \boldsymbol{\eta_{th}} = -13.972 + 0.809\sqrt{T_{\infty,h}} + 0.646\dfrac{\log_{10}(t_{N,P})}{\log_{10}(0.793)} + 1.626(D_{pin}) - 0.166(D_{pin})^2 \in \mathbb{A}_2 & (3.32b) \\ \boldsymbol{\zeta} = -18598.384 + 4.329(T_{\infty,h}) + (3.113 \cdot 10^{-3})(T_{\infty,h})^2 + 49.018(t_{N,P})^{1.569} + 17053.212(D_{pin})^{0.004} \in \mathbb{A}_2 & (3.32c) \end{cases}$$

$$\begin{bmatrix} 350 \leq T_\infty \,[\mathrm{K}] \leq 700 \\ 0.5 \leq t_{N,P} \,[\mathrm{mm}] \leq 5 \\ 1.5875 \leq D_{pin} \,[\mathrm{mm}] \leq 6.350 \end{bmatrix}$$

$$\mathbb{Z}_3 = \begin{cases} \boldsymbol{P_o} = -134.013 + 11.526(T_{\infty,h})^{0.694} + 108.534(t_{N,P})^{-371.718} - 1.362(D_{pin})^{-0.149} \in \mathbb{A}_3 & (3.33a) \\ \boldsymbol{\eta_{th}} = 6.133 + 0.040\sqrt{M_{max}} + 0.674(D_{pin}) + -0.142(D_{pin})^2 + 1.134\dfrac{\log_{10}(\mathrm{Re})}{\log_{10}(73.205)} \in \mathbb{A}_3 & (3.33b) \\ \boldsymbol{\zeta} = 1653.634 + 2.674(M_{max})^{1.285} + 22.273(D_{pin}) + 1.000(D_{pin})^2 - 150.539(\mathrm{Re})^{0.297} \in \mathbb{A}_3 & (3.33c) \end{cases}$$

$$\begin{bmatrix} 4 \leq M_{max} \leq 100 \\ 1.5875 \leq D_{pin}, [\mathrm{mm}] \leq 6.350 \\ 3,000 \leq \mathrm{Re} \leq 15,000 \end{bmatrix}$$

4.0 Conclusion And Future Work

4.1 Conclusions

This thesis took a robust approach in investigating the performance of integrated thermoelectric devices. This was done through the implementation of several sub-routines in a solution algorithm and running the algorithm over a large multivariable design space. The resultant data was then used for a rigorous mathematical study which composed of a parametric study, the determination of linear correlations between independent and dependent variables, the determination of design configurations that yield maximum numeric values for variables of interest, and lastly, a non-linear regression analysis to determine relationships between independent variables and dependent variable of interest in a restricted domain. In Chap. 2, the governing equations used to represent the physical phenomena as well as how they are solved were discussed. In Chap. 3, the results of data validation, a parametric study, linear regression analysis and non-linear regression analysis were presented and discussed. As a result, several contributions have been made.

The first contribution is the development and implementation of a solution algorithm to determine the performance of the integrated thermoelectric devices. The solution algorithm is based on conservation of energy principles and incorporates temperature dependency of material properties to more accurately reflect steady-state solutions. The results were validated with published data from another numerical model.

The second contribution is the determination of the most influential independent variables on the performance solutions of the integrated thermoelectric device. Proposed non-linear relationship between a set of independent variables and the performance solutions were also presented. The relationships are based on the configurations of the maximum numeric values of each performance solutions. Given there were three performance solutions, a total of nine non-linear equations were developed via non-linear regression.

4.2 Future Work

This work exists as a portion of a larger body of work. The impetus of this work is to provide a large set of performance predictions of the iTED operating under all possible thermal-fluid conditions when applied to a Cummins ISL diesel-powered transit bus. The results of this model will then be correlated to high-fidelity fully-coupled numeric results through the use of multi-fidelity modeling methods. Then, the non-linear multivariate regressions would be re-run to provide a functional description of the iTED based upon the most relevant and impactful independent variables. These functions will then be incorporated into a drive-cycle model of a Cummins ISL diesel-powered transit bus.

The drive cycle model will be based upon experimentally collected operational data of transit buses operated by the Port Authority of Allegheny County. The model will relate driving conditions, exhaust characteristics including temperature, flow rate and back-pressure, electrical demands and production via the alternator to fuel consumption. By incorporating the iTED into the exhaust system, predictions of reducing fuel consumption can be made; the production of electrical power from the exhaust gases can offset parasitic engine losses due to alternator loading, and the potential for this will be quantified. Via the coupling of the aforementioned mathematical model of the iTED to the drive-cycle model of a transit bus, every permissible iTED configuration can be analyzed under every possible driving condition. The configuration that maximizes the desired output (i.e. fuel savings) can be selected using time-averaged data from multiple buses operating along different routes throughout different times of the year as the model input.

Consideration for the effects of empirical correlations is another avenue to study. The Nusselt number has several empirical correlations such as those developed by Colburn and Žukauskas. Figures 4.1 - 4.3 show the device electrical resistance as a function of Reynolds number using the configuration used for maximum power, thermal conversion efficiency and performance index respectively. Each plot compares the Nusselt number correlation developed by Colburn and Žukauskas.

Deviation appears to be most evident in the maximum performance index configuration, less evident in the maximum efficiency configuration and somewhere in the middle in the maximum power output configuration. Depending on the solution(s) of interest, further investigation of device performance as a function of independent variables and Nusselt number correlations can be explored.

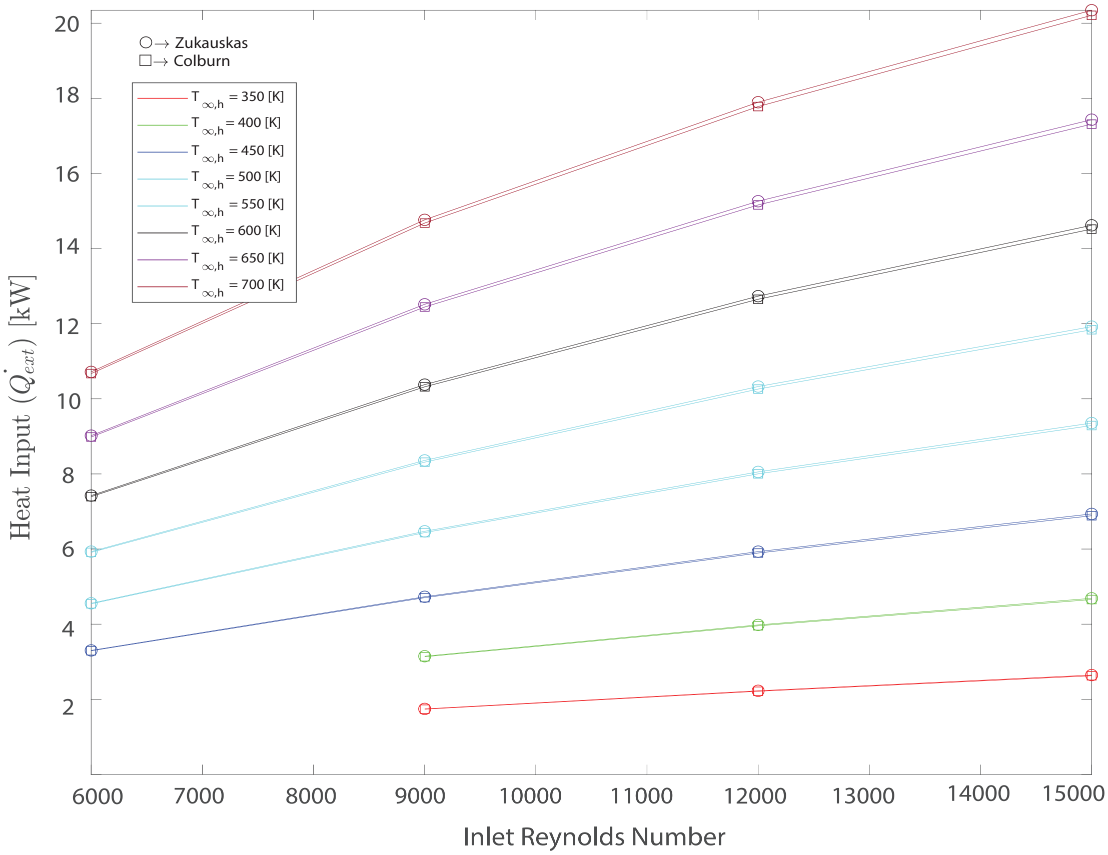

Figure 4.1: Heat extraction versus inlet Reynolds number for set $\mathbb{A}_1$

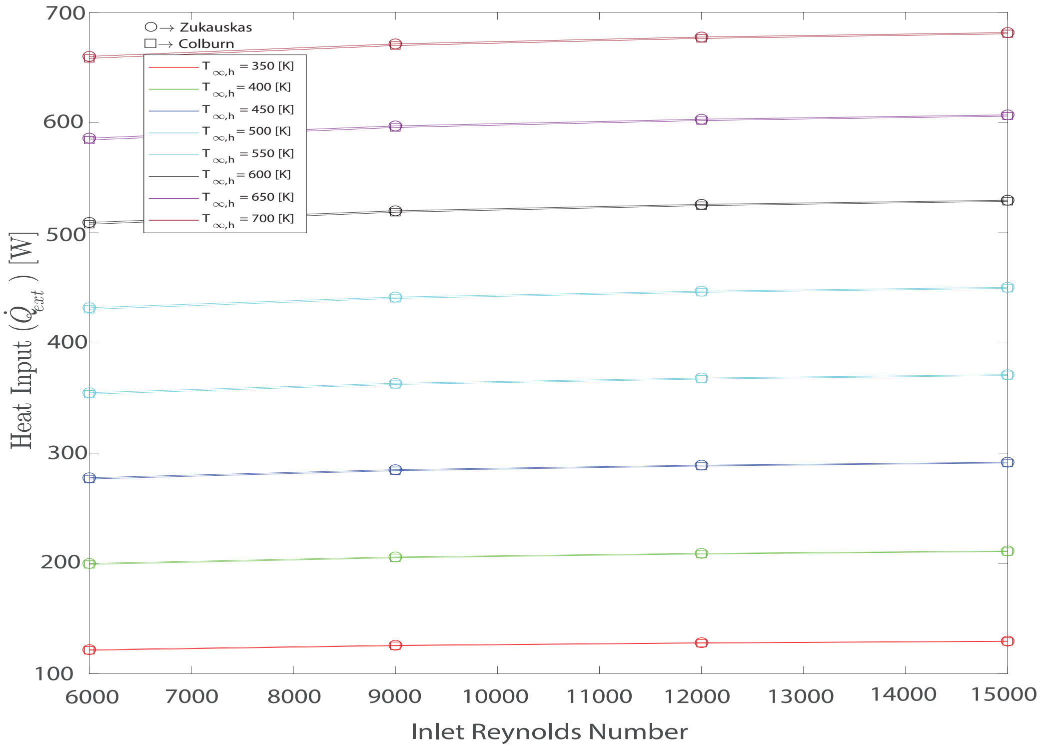

Figure 4.2: Heat extraction versus inlet Reynolds number for set $\mathbb{A}_2$

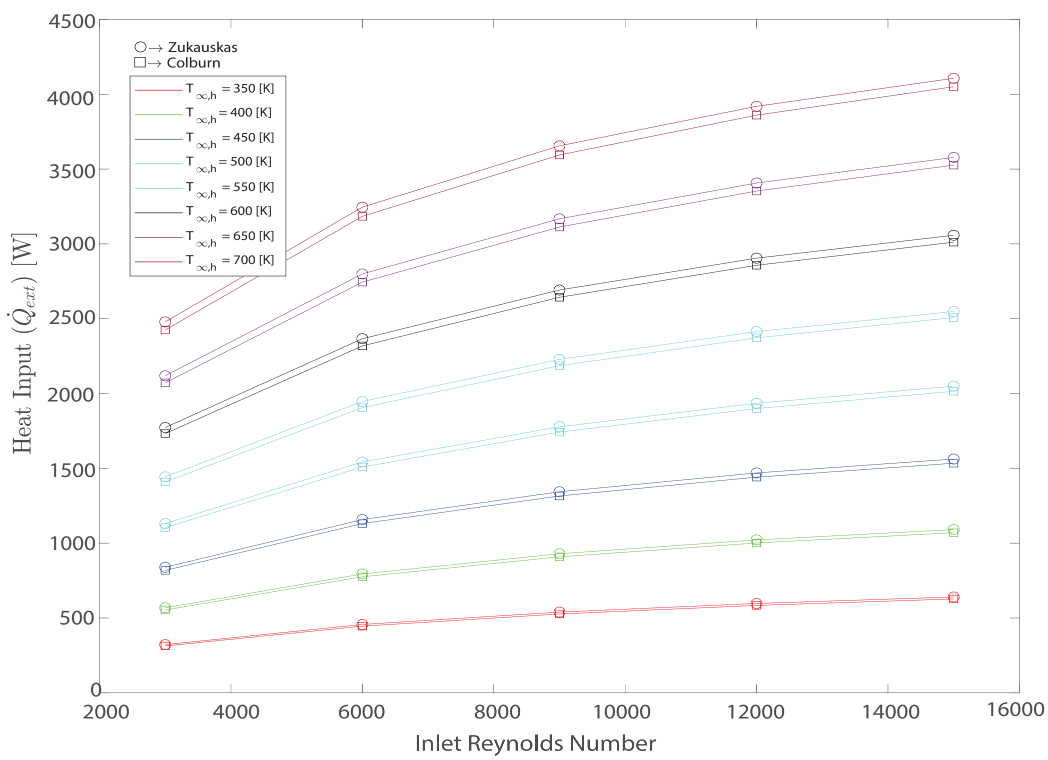

Figure 4.3: Heat extraction versus inlet Reynolds number for set $\mathbb{A}_3$

Appendix

Nomenclature

(This page is intentionally left blank.)

Variables

A	area, m^2
A_c	cross-sectional area, m^2
C_p	specific heat of fluid, $kJkg^{-1}$-K^{-1}
D	diameter, m
D_h	hydraulic diameter, m
H	height, m
I	electric current, A
K	thermal conductance, WK^{-1}
L	leg length, m
M	pins per row
$\dot{m}$	mass flow rate, kg-s^{-1}
N	number of rows
Nu	Nusselt number
P	pressure, Pa
P_o	power output, W
Pr	Prandtl number
Q	heat, W
R	electrical or thermal resistance, Ω or KW^{-1}
Re	Reynolds number
S_L	longitudinal pitch, m
S_T	transverse pitch, m
T	temperature, K
ΔV	electric Potential, V
$\dot{\forall}$	volumetric flow rate, kg-m^{-3}
W	width, m

Greek symbols

α	Seebeck coefficient, VK^{-1}
β	generic property
γ	generic solution
ϵ	surface roughness or relative estimated error, m or dimensionless
ζ	performance index, dimensionless
η_{th}	thermoelectric conversion efficiency, dimensionless
λ	thermal conductivity, $Wm^{-1}K^{-1}$
μ	dynamic viscosity, Pa-s
ν	kinematic viscosity, m^2-s^{-1}
ρ_{el}	electrical resistivity, Ωm
ρ	density, kg-m^{-3}
τ	Thomson coefficient , VK^{-1}

Subscripts

air	Air	∞	source or sink
adj	adjusted	int	interconnector
c	cold or cross-sectional	l	local or loss
cer	ceramic	max	maximum
cond	conduction	N,n	n-type semiconductor
conv	convection	oc	Seebeck potential, open circuit
el	electrical	P,p	p-type semiconductor
exit	exit	pin	Pin
g	grease	s	surface
h	hot or hydraulic	th	thermal
hex	heat exchanger	tot	total
in	inlet/internal		

Bibliography

[1] U.S EPA, Inventory of U.S Greenhouse Gas Emissions and Sinks: 1990–2017, Tech. rep., United States EPA Washington D.C (2019).

[2] B. Nordell, Thermal pollution causes global warming, Global and Planetary Change 38 (3-4) (2003) 305–312.

[3] LLNL, Estimated u.s. energy consumption in 2017.
URL https://flowcharts.llnl.gov/

[4] S. Carnot, Réflexions sur la puissance motrice du feu et sur les machines propres à développer cette puissance, in: Annales scientifiques de l'École Normale Supérieure, Vol. 1, 1872, pp. 393–457.

[5] S. Eggleston, L. Buendia, K. Miwa, T. Ngara, K. Tanabe, Intergovernmental panel on climate change guidelines for national greenhouse gas inventories, intergovernmental panel on climate change, Paris: IPCC Secretariat.

[6] S. Kirschke, P. Bousquet, P. Ciais, M. Saunois, J. G. Canadell, E. J. Dlugokencky, P. Bergamaschi, D. Bergmann, D. R. Blake, L. Bruhwiler, et al., Three decades of global methane sources and sinks, Nature geoscience 6 (10) (2013) 813–823.

[7] D. Singh, E. Croiset, P. L. Douglas, M. A. Douglas, Techno-economic study of CO_2 capture from an existing coal-fired power plant: Mea scrubbing vs. O_2/CO_2 recycle combustion, Energy conversion and Management 44 (19) (2003) 3073–3091.

[8] Y. Ding, E. Alpay, High temperature recovery of CO_2 from flue gases using hydrotalcite adsorbent, Process Safety and Environmental Protection 79 (1) (2001) 45–51.

[9] S. Brückner, S. Liu, L. Miró, M. Radspieler, L. F. Cabeza, E. Lävemann, Industrial waste heat recovery technologies: An economic analysis of heat transformation technologies, Applied Energy 151 (2015) 157–167.

[10] H. Jouhara, N. Khordehgah, S. Almahmoud, B. Delpech, A. Chauhan, S. A. Tassou, Waste heat recovery technologies and applications, Thermal Science and Engineering Progress 6 (2018) 268–289.

[11] E. Worrell, C. Galitsky, E. Masanet, W. Graus, Energy efficiency improvement and cost saving opportunities for the glass industry, Berkeley National Laboratory (2008) 60.

[12] W. C. Turner, S. Doty, Energy management handbook, 2009.

[13] R. K. Shah, D. P. Sekulic, Fundamentals of heat exchanger design, John Wiley & Sons, 2003.

[14] J. Wallin, H. Madani, J. Claesson, Run-around coil ventilation heat recovery system: A comparative study between different system configurations, Applied Energy 90 (1) (2012) 258–265.

[15] A. Faghri, Heat Pipes: Review, Opportunities and Challenges, Frontiers in Heat Pipes 5 (1) (2014) 2–15.

[16] T. J. Seebeck, Ueber die magnetische polarisation der metalle und erze durch temperaturdifferenz, Annalen der Physik 82 (3) (1826) 253–286.

[17] J.-C. Peltier, Nouvelles expériences sur la caloricité des courants électrique, Ann. Chim. Phys 56 (371) (1834) 371–386.

[18] W. Thomson, On a mechanical theory of thermo-electric currents, Proceedings of the Royal society of Edinburgh 3 (1857) 91–98.

[19] C. A. Domenicali, Irreversible thermodynamics of thermoelectricity, Reviews of Modern Physics 26 (2) (1954) 237.

[20] D. M. Rowe, Thermoelectrics, an environmentally-friendly source of electrical power, Renewable Energy 16 (1-4) (1999) 1251–1256.

[21] X. Tang, Q. Zhang, L. Chen, T. Goto, T. Hirai, Synthesis and thermoelectric properties of p-type-and n-type-filled skutterudite $R_yM_xCo_{4-x}Sb_{12}$ (R: Ce, Ba, Y; M: Fe, Ni), Journal of Applied Physics 97 (9) (2005) 093712.

[22] X. Zhao, X. Ji, Y. Zhang, T. Zhu, J. Tu, X. Zhang, Bismuth telluride nanotubes and the effects on the thermoelectric properties of nanotube-containing nanocomposites, Applied Physics Letters 86 (6) (2005) 062111.

[23] G. Rogl, A. Grytsiv, E. Bauer, P. Rogl, M. Zehetbauer, Thermoelectric properties of novel skutterudites with didymium: DD_y $(Fe_{1-x}$ $Co_x)_4$ Sb_{12} and DD_y $(Fe_{1-x}$ $Ni_x)_4$ Sb_{12}, Intermetallics 18 (1) (2010) 57–64.

[24] E. Thacher, B. Helenbrook, M. Karri, C. J. Richter, Testing of an automobile exhaust thermoelectric generator in a light truck, Proceedings of the Institution of Mechanical Engineers, Part D: Journal of Automobile Engineering 221 (1) (2007) 95–107.

[25] M. Stordeur, I. Stark, Low power thermoelectric generator-self-sufficient energy supply for micro systems, in: XVI ICT'97. Proceedings ICT'97. 16th International Conference on Thermoelectrics (Cat. No. 97TH8291), IEEE, 1997, pp. 575–577.

[26] C. Suter, P. Tomeš, A. Weidenkaff, A. Steinfeld, Heat transfer and geometrical analysis of thermoelectric converters driven by concentrated solar radiation, Materials 3 (4) (2010) 2735–2752.

[27] D. T. Crane, An introduction to system-level, steady-state and transient modeling and optimization of high-power-density thermoelectric generator devices made of segmented thermoelectric elements, Journal of Electronic Materials 40 (5) (2011) 561–569.

[28] D. Crane, C. Koripella, V. Jovovic, Validating steady-state and transient modeling tools for high-power-density thermoelectric generators, Journal of Electronic Materials 41 (6) (2012) 1524–1534.

[29] K. Qiu, A. Hayden, Integrated thermoelectric generator and application to self-powered heating systems, in: 2006 25th International Conference on Thermoelectrics, IEEE, 2006, pp. 198–203.

[30] B. Reddy, M. Barry, J. Li, M. K. Chyu, Thermoelectric performance of novel composite and integrated devices applied to waste heat recovery, Journal of heat transfer 135 (3).

[31] B. Reddy, M. Barry, J. Li, M. K. Chyu, A fluid-thermo-electric coupled field analysis of a novel integrated thermoelectric device, Energy Procedia 14 (2012) 2088–2095.

[32] B. Reddy, M. Barry, J. Li, M. K. Chyu, Three-dimensional multiphysics coupled field analysis of an integrated thermoelectric device, Numerical Heat Transfer, Part A: Applications 62 (12) (2012) 933–947.

[33] B. Reddy, M. Barry, J. Li, M. Chyu, Enhancement of thermoelectric device performance through integrated flow channels, Frontiers in Heat and Mass Transfer (FHMT) 4 (2).

[34] B. Reddy, M. Barry, J. Li, M. K. Chyu, Thermoelectric-hydraulic performance of a multistage integrated thermoelectric power generator, Energy conversion and management 77 (2014) 458–468.

[35] M. Barry, K. Agbim, B. Reddy, M. K. Chyu, Experimental investigations on the performance of a thermoelectric device with an integrated heat exchanger and flow channels, in: International Heat Transfer Conference Digital Library, Begel House Inc., 2014.

[36] M. M. Barry, K. A. Agbim, M. K. Chyu, Performance of a thermoelectric device with integrated heat exchangers, Journal of Electronic Materials 44 (6) (2015) 1394–1401.

[37] F. Meng, L. Chen, F. Sun, A numerical model and comparative investigation of a thermoelectric generator with multi-irreversibilities, Energy 36 (5) (2011) 3513–3522.

[38] M. E. Demir, I. Dincer, Development and heat transfer analysis of a new heat recovery system with thermoelectric generator, International Journal of Heat and Mass Transfer 108 (2017) 2002–2010.

[39] J. Yu, H. Zhao, A numerical model for thermoelectric generator with the parallel-plate heat exchanger, Journal of Power Sources 172 (1) (2007) 428–434.

[40] W. He, S. Wang, X. Zhang, Y. Li, C. Lu, Optimization design method of thermoelectric generator based on exhaust gas parameters for recovery of engine waste heat, Energy 91 (2015) 1–9.

[41] S. Kumar, S. D. Heister, X. Xu, J. R. Salvador, G. P. Meisner, Thermoelectric generators for automotive waste heat recovery systems part i: numerical modeling and baseline model analysis, Journal of electronic materials 42 (4) (2013) 665–674.

[42] S. Kumar, S. D. Heister, X. Xu, J. R. Salvador, G. P. Meisner, Thermoelectric generators for automotive waste heat recovery systems part ii: parametric evaluation and topological studies, Journal of electronic materials 42 (6) (2013) 944–955.

[43] M. Zhang, Y. Tian, H. Xie, Z. Wu, Y. Wang, Influence of thomson effect on the thermoelectric generator, International Journal of Heat and Mass Transfer 137 (2019) 1183–1190.

[44] A. Žukauskas, Heat transfer from tubes in crossflow, in: Advances in heat transfer, Vol. 8, Elsevier, 1972, pp. 93–160.

[45] P. R. Chandra, M. L. Fontenot, J.-C. Han, Effect of rib profiles on turbulent channel flow heat transfer, Journal of thermophysics and heat transfer 12 (1) (1998) 116–118.

[46] S. E. Haaland, Simple and explicit formulas for the friction factor in turbulent pipe flow, Journal of Fluids Engineering 105 (1) (1983) 89–90.

[47] C. F. Colebrook, T. Blench, H. Chatley, E. Essex, J. Finniecome, G. Lacey, J. Williamson, G. Macdonald, Correspondence. turbulent flow in pipes, with particular reference to the transition region between the smooth and rough pipe laws.(includes plates)., Journal of the Institution of Civil engineers 12 (8) (1939) 393–422.

[48] G. S. Ohm, Die galvanische Kette, mathematisch bearbeitet, TH Riemann, 1827.

[49] M. H. von Jacobi, Die Galvanoplastik, oder, Das Verfahren cohärentes Kupfer in Platten: oder nach sonst gegebenen Formen, unmittel-bar aus Kupferauflösungen, auf galvanischem Wege zu produciren: nach dem auf Befehl des Gouvernements in russischer Sprache bekannt gemachten Originale, Eggers, 1840.

[50] L. F. Moody, Friction factors for pipe flow, Trans. Asme 66 (1944) 671–684.

[51] D. F. Young, B. R. Munson, T. H. Okiishi, W. W. Huebsch, A brief introduction to fluid mechanics, John Wiley & Sons, 2010.

[52] M. M. Barry, K. A. Agbim, P. Rao, C. E. Clifford, B. Reddy, M. K. Chyu, Geometric optimization of thermoelectric elements for maximum efficiency and power output, Energy 112 (2016) 388–407.

[53] C. E. Clifford, M. M. Barry, S. Sammak, Multiphysics fluid-thermal-electric-coupled modeling of a novel pin-fin integrated thermoelectric device applied to heavy-duty diesel engine waste heat recovery, Applied Energy. Manuscript submitted for publication.

[54] J. M. Said, J. R. Rivero, C. E. Clifford, M. J. Durka, A. D. Fradeneck, M. L. Kimber, M. M. Barry, Thermal-Fluid-Electric Coupled Modeling of a Novel Pin-Fin Integrated Thermoelectric Device, in: International Conference on Thermoelectrics, Pasadena, CA, 2017.

[55] C. E. Clifford, S. Sammak, A. D. Fradeneck, J. R. Rivero, M. L. Kimber, M. M. Barry, Thermal-Fluid-Electric Coupled Modeling of Novel Pin-Fin Integrated Thermoelectric Devices - The effect of Packing Density on Performance, in: 3rd Thermal and Fluids Engineering Conference (TFEC), American Society of Thermal and Fluids Engineers (ASTFE), Fort Lauderdale, FL, 2018.

[56] I. G. Lantgios, E. M. Ledesma, J. A. Cameron, J. R. Rivero, C. E. Clifford, A. D. Fradeneck, S. Sammak, M. M. Barry, Waste Heat Recovery of Cummins ISL Diesel Engines using Integrated Thermoelectric Devices - Thermal-Fluid-Electric Coupled Numerical Modeling, in: 4th Thermal and Fluids Engineering Conference (TFEC), American Society of Thermal and Fluids Engineers (ASTFE), Las Vegas, NV, 2019.

[57] G. W. Sutton, Direct energy conversion, New York, McGraw-Hill Book Company, 1966.

[58] S. W. Angrist, Direct energy conversion, Allyn and Bacon, Inc., Boston, 1976.

[59] K. Levenberg, A method for the solution of certain nonlinear problems, Quart. Appl. Math. 2 (1944) 164–168.

[60] D. W. Marquardt, An algorithm for least-squares estimation of nonlinear parameters, Journal of the society for Industrial and Applied Mathematics 11 (2) (1963) 431–441.

[61] A. Cauchy, Méthode générale pour la résolution des systemes d'équations simultanées, Comp. Rend. Sci. Paris 25 (1847) (1847) 536–538.

[62] R. W. Wedderburn, Quasi-likelihood functions, generalized linear models, and the gauss—newton method, Biometrika 61 (3) (1974) 439–447.

[63] MathWorks, lsqcurvefit.
URL https://www.mathworks.com/help/optim/ug/lsqcurvefit.html